

University of Groningen

Domain walls and their conduction properties in ferroelectric BiFeO₃ thin films

Farokhipoor, Saeedeh

IMPORTANT NOTE: You are advised to consult the publisher's version (publisher's PDF) if you wish to cite from it. Please check the document version below.

Document Version

Publisher's PDF, also known as Version of record

Publication date:

2013

[Link to publication in University of Groningen/UMCG research database](#)

Citation for published version (APA):

Farokhipoor, S. (2013). Domain walls and their conduction properties in ferroelectric BiFeO₃ thin films
Groningen: s.n.

Copyright

Other than for strictly personal use, it is not permitted to download or to forward/distribute the text or part of it without the consent of the author(s) and/or copyright holder(s), unless the work is under an open content license (like Creative Commons).

Take-down policy

If you believe that this document breaches copyright please contact us providing details, and we will remove access to the work immediately and investigate your claim.

Downloaded from the University of Groningen/UMCG research database (Pure): <http://www.rug.nl/research/portal>. For technical reasons the number of authors shown on this cover page is limited to 10 maximum.

RIJKSUNIVERSITEIT GRONINGEN

Domain walls and their conduction properties in ferroelectric BiFeO_3 thin films

Proefschrift

ter verkrijging van het doctoraat in de
Wiskunde en Natuurwetenschappen
aan de Rijksuniversiteit Groningen
op gezag van de
Rector Magnificus, dr. E. Sterken,
in het openbaar te verdedigen op
vrijdag 26 april 2013
om 11.00 uur

door

Saeedeh Farokhipoor

geboren op 22 mei 1981
te Tehran, Iran

Promotores: Prof. dr. B. Noheda
Prof. dr. T.T.M. Palstra

Beoordelingscommissie: Prof. dr. H.M. Christen
Prof. dr. G. Catalan
Prof. dr. A.J.H.M. Rijnders

ISBN(BOOK): 978-90-367-6137-6

ISBN(DIGITAL): 978-90-367-6136-9

To my family

Contents

1	Introduction	1
1.1	General introduction to multiferroic materials	1
1.2	Perovskites	2
1.3	Thin films	3
1.4	Ferroics	5
1.4.1	Ferroelectricity	6
1.4.2	Ferroelasticity	8
1.5	BiFeO ₃	8
1.5.1	Characterization	8
1.5.2	Thin films of BiFeO ₃	10
1.6	Domains	10
1.7	Domain walls	11
1.7.1	Domain wall transport	14
1.7.2	Origin of domain wall conductivity	15
1.8	Conduction mechanisms	15
1.8.1	Thermionic emission at interfaces and Poole-Frenkel emission in bulk	16
1.8.2	Fowler Nordheim tunneling	18
1.8.3	Space charge limited conduction current	18
	Bibliography	19
2	Experimental techniques	23
2.1	Abstract	23
2.2	Substrate treatment	24
2.2.1	Pulsed Laser Deposition	24
2.3	Reflection High Energy Electron Diffraction (RHEED)	28

2.4	X-ray Diffraction (XRD)	31
2.4.1	Grazing incidence	32
2.4.2	Reciprocal space maps	33
2.4.3	X-ray reflectivity	34
2.5	Atomic Force Microscopy (AFM)	35
2.5.1	Experimental set up	36
2.5.2	Operating principle	38
2.5.3	AFM modes	38
2.5.4	Piezo Force Microscopy (PFM)	40
2.5.5	Domain imaging process by PFM	41
2.5.6	Conductive-AFM	42
	Bibliography	45
3	Tuning atomic and domain structure of epitaxial multiferroic BiFeO₃	47
3.1	Abstract	47
3.2	Introduction	48
3.3	Methodology	49
3.4	Results and discussion	50
3.5	Conclusion	58
3.6	Experimental	58
	Bibliography	61
4	Conduction through domain walls in BiFeO₃ thin films	63
4.1	Abstract	63
4.2	Introduction	64
4.3	Results and discussions	65
4.4	Conclusion	71
4.5	Experimental	71
	Bibliography	75
5	Conduction mechanisms around twin walls of (001)-BiFeO₃ films	77
5.1	Abstract	77
5.2	Introduction	78
5.3	Results and discussion	79

5.4	Conclusion	90
5.5	Experimental	91
	Bibliography	93
6	Ferroelectric resistive switching in BiFeO₃ thin films	95
6.1	Abstract	95
6.2	Introduction	96
6.3	Results	98
6.4	Discussion	104
6.5	Conclusion	105
6.6	Experimental	105
	Bibliography	107
	Summary	111
	Samenvatting	115
	Acknowledgements	119

Chapter 1

Introduction

1.1 General introduction to multiferroic materials

The current general interest in multiferroics was triggered by a paper published in 2000 by Hill, who pointed out that only a few materials exist that unite both ferromagnetic and ferroelectric properties in a single phase[1].

In this review, mainly multiferroic oxides were discussed. Their scarcity was ascribed to contradicting requirements for ferromagnetism and ferroelectricity: ferroelectrics typically require empty d-shells, whereas magnetism requires partially filled d (or f) shells. One way to circumvent these conflicting requirements would be a perovskite structure providing ferroelectricity from the A-site cation and magnetism from the B-site cation. There are compounds containing lone-pair Bi in the A-site, such as $\text{Bi}(\text{Cr},\text{Fe})\text{O}_3$. In other multiferroics ferroelectricity appears because the magnetic structure breaks inversion symmetry. These materials display larger magnetoelectric couplings but they typically show multiferroicity only at low temperatures (see e.g. TbMnO_3 , TbMn_2O_5 ,...).

There has been a tendency to focus on multiferroic oxides, particularly perovskites. This is probably motivated by the large piezoelectric and dielectric responses in some very popular perovskites, like PbTiO_3 , BaTiO_3 ; the interesting magnetic properties of some other provskites like $(\text{LaSr})\text{MnO}_3$ or LaCaMnO_3 , and by the fact that first-principle calculation are developed to the extend that they provide mechanistic insight on these structurally simple materials[2].

Despite these advantages, Catalan and Scott pointed out that *a-priori* there is no reason to expect that oxides will have the most exciting physics

with respect to device applications[3]. In 1995, J.F. Scott *et al.*, have reminded people in the field that there are hundreds of interesting non-oxide ferroelectrics with a transition temperature higher than room temperature[4]. During the same decade, Abrahams and Ravez started introducing a list of magnetic materials that have the possibility to be ferroelectric, including both oxides and fluorides families[5; 6]. More recently, more studies on fluorides and oxyfluorides families have been reviewed by Palstra *et al.*,[7].

However, the field has remained mainly focused on oxides due to convenience of oxide growth, in particular, due to the possibility to produce high quality specimens in thin film form and the possibility of strain engineering. This has much to do with the fact that theoretical calculations, which play a crucial role in designing new materials and predicting and understanding their behavior, are considerably easier and more developed in oxides with simple unit cells, such as perovskites. The scope of this thesis will be on one the most famous and the only room-temperature multiferroic: the perovskite BiFeO_3 (BFO).

1.2 Perovskites

In this Thesis, I will refer to the perovskite structure with the ABO_3 formula, where both "A" and "B" are in a trivalent state. Oxygen anions coordinate in corner-shared, octahedral, face-centered fashion, forming a chain of octahedral cages throughout the crystal structure in three dimensions; while the smaller size cation (B) can be found inside the octahedral cage. The "A" position is occupied by a 12-fold coordinated cation located in the voids between the octahedra.

The parent structure has cubic symmetry with space group $\text{Pm}\bar{3}\text{m}$. However, most of the interesting perovskite-like materials are in fact distorted perovskites in which one or both cations and/or the oxygens shift along particular directions, lowering the symmetry. In our model system (bulk BFO at room temperature) the crystal symmetry is rhombohedral with space group; $\text{R}\bar{3}\text{c}$ as shown in figure 1.1.

The stability of ABO_3 type structure is determined by the tolerance factor, which is 1 for an ideal cubic perovskite. This factor was for the first time introduced by Goldschmidt[8] and it is as follows:

$$t = \frac{r_A + r_O}{\sqrt{2}(r_B + r_O)} \quad (1.1)$$

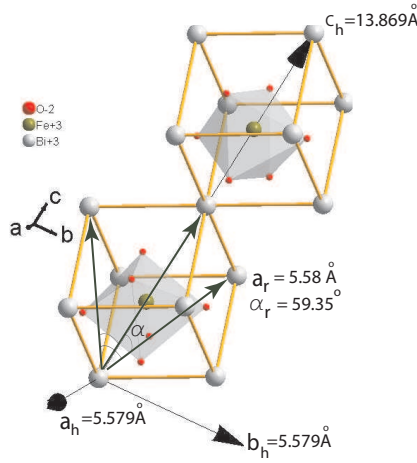


Figure 1.1: Unit cell of the rhombohedral crystal structure of BFO_3 , showing the hexagonal and rhombohedral lattice parameters.

Where r_A , r_B and r_O are the ionic radius of A, B and oxygen ions, respectively.

In general, there are 3 different distortion mechanisms giving rise to different tolerance factors: octahedral distortion, cation displacement and octahedral tilting. The tolerance factor values for most of the perovskites ranges from 0.7 to 1.06. For tetragonal symmetry it is larger 1. For $0.9 \leq t \leq 1$ perovskites acquire the rhombohedral structure, and for $0.75 \leq t \leq 0.9$, that is for smallest A cation, perovskite tend to be orthorhombic. By considering the Shannon radii[9], with Bi^{+3} in twelffold coordination and Fe^{3+} in sixfold coordination, the tolerance factor of BFO is 0.88. In BFO both cation shifts and octahedra tilts are present.

1.3 Thin films

In modern technology, such as in solar cells, LCD displays, memory devices and other applications that require integration (assembly into integrated circuits), most of the devices are preferred in thin film form. In many of these applications, the thickness of the thin layer is in the micrometer range. A subgroup within the big family of thin films is the one formed by epitaxial thin films, which are under strain (deformed with respect to

their ground state structure) on a crystal structure. The stress that causes this lattice deformation originates from the mismatch between the lattice parameters of the film and the substrate. Therefore, growing epitaxial thin films enables us to impose structural changes in a material and, thus, to modify its properties. A relatively large mismatch between the lattice parameters and/or the structure of the thin film and the substrate can give rise to a film with a crystal structure different than that of the substrate; nonetheless, the film can still be epitaxially grown if there is a clear crystallographic relationship between the substrate and the capping thin layer. On the other hand, a so-called coherent film is obtained when the lattice mismatch between the thin layer and the substrate is very small and the structure very similar. Such that, the atoms of the film can grow exactly on top of the atoms of the substrate[10].

Depending on the magnitude of the mismatch, a thin film can be fully strained, partially strained (or partially relaxed) and completely relaxed. The mathematical definition of misfit strain is $u_m = (a_{film}/a_{substrate}) - 1$, where a_{film} refers to in-plane lattice parameters of the film and $a_{substrate}$ corresponds to the in-plane lattice parameters of the substrate. Tensile and compressive strain give negative and positive misfit strain, respectively. Applied stress and the resulting induced strain in the material cost energy, which is proportional to the film thickness. As the film thickness grows, the strain energy competes with the energy needed to relax the lattice by means of dislocations, disclinations, atomic vacancies or crystallographic domains (domain boundaries)[11; 12]. Which mechanism will take place depends very much on the type of materials used and the kinetics of the growth. While for Si or Ge-based semiconductors dislocations are most common, in transition metal oxides, oxygen vacancies are often formed to relax the lattice. Moreover, in ferroelastic perovskites, twin formation is energetically less costly than the formation of dislocations. The density of defects present during relaxation depends thus on the lattice mismatch and thickness and it is important to mention that the temperature dependence of the lattice mismatch plays an important role. This evidences the complex relation between misfit strain and critical thickness for strain relaxation[13].

In the present thesis we will discuss thin films of BFO on cubic SrTiO₃ substrates, which we have shown to behave differently than usually expected. Normally, strain develops in these films when the unit cell matches the substrate lattice. In the case of BFO however, the combination of dif-

ferent domain variants or twins (instead of a single unit cell) match the substrate lattice, providing a singular evolution of the lattice parameters. This is extensively discussed in chapter 3.

1.4 Ferroics

We have already introduced that BFO, the material investigated is multiferroic. Here we describe in more detail what are ferroics and multiferroics. Ferroics are materials that display spontaneous ordering of a physical quantity below a certain temperature, the ordering temperature (T_o). Three types of ferroic materials have been known for a long time: ferroelectrics present spontaneous electrical polarization, ferromagnets show spontaneous magnetization and ferroelastics display spontaneous strain. Within the Landau approach, these physical properties are the so-called order parameter of the ferroelectric, ferromagnetic or ferroelastic phase transition, respectively. The essential and distinct characteristic of a ferroic material is the formation of domains, or energetically equivalent regions with different orientations of the order parameter. In 2007, Fiebig *et al.*, observed for the first time another type of ordering which has been named ferrotoroidicity[14]. A vortex of magnetic moments can generate a toroidal moment[15]. This thesis focusses on the material BFO, which does not display ferrotoroidicity so we will not discuss this property further. Ferroics can be also characterized by their response under time and space reversal, as presented in figure 1.2.

The so-called multiferroic materials display two or more ferroic orderings within the same phase, breaking time and space reversal symmetry, simultaneously. In recent years, multiferroics have obtained a lot of attention because of their potential to present large magnetoelectric effect. This is of fundamental interest but also of technological importance because it would allow the control of magnetization (polarization) in devices using an electric (magnetic) field. BFO is a ferroelectric, ferroelastic and antiferromagnetic material. The Fe^{3+} spins order in spiral fashion with a very long period of 62-64nm[16]. The spins are canted but they cancel each other giving an average zero magnetic moment. However, epitaxial strain can in principle modify this and give rise to net magnetic moment in the films[17]. This thesis is not dealing with the magnetic properties of BiFeO_3 and thus we will now discuss ferroelectricity and ferroelasticity in more detail.

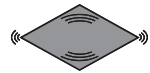
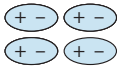
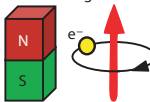
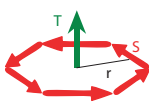
		Space	
		Invariant	Change
Time	Invariant	Ferroelastic 	Ferroelectric 
	Change	Ferromagnetic 	Ferrotoroidic 

Figure 1.2: All forms of ferroic materials under time and spatial reversal, adapted from[14].

1.4.1 Ferroelectricity

All dielectrics can be electrically polarized, that is, they show a dipole moment per unit cell in the presence of an external electric field. Ferroelectrics are a particular type of dielectrics in which the polarization can be switched by an external electric field. In addition, they show polarization even without applying field. That is called remanent polarization. The polarization remains up to the ferroelectric Curie temperature, above which the material is depolarized and becomes paraelectric. That temperature-dependent behaviour makes a dielectric material pyroelectric. Pyroelectric materials are ferroelectric only if the polarization can be switched by an electric field. This is allowed due to symmetry breaking and it is present in certain crystals that lack inversion symmetry and that allow a dipole moment in the unit cell. In ferroelectrics, the polarization as a function of the applied field is highly non-linear and shows hysteretic behavior, very much like in ferromagnets, as shown in figure 1.3. Thus a binary state or double potential well exists at zero field. Besides the presence of the remanent polarization, they can easily be polarized and thus they display the largest dielectric susceptibilities in nature.

Ferroelectrics are of interest for many different applications, from statics dynamics. Because of the non-zero and switchable remanent polarization, they are used as non-volatile RAM memories in low memory applications like ID cards (in the Japanese railway system or the Play Station). Due to their pyroelectric behaviour, they are used as infrared detectors. Moreover, all ferroelectrics are piezoelectrics, which means that they can

transform mechanical energy into electrical energy and vice versa. This makes them useful in many applications, such as accelerometers, ultrasound generators (in sonars or medical apparatuses), gyroscopes, thermistors, actuators, fuel injection nozzles on diesel engines, vibration dampers (in helicopter blades or cars), micropositioners (in microscopes), voltage generators (in gas lighters), shock detectors (in airbags) and many others.

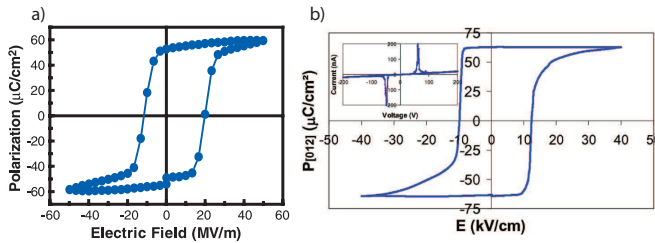


Figure 1.3: Hysteresis loops of a) epitaxial thin film of BFO, adapted from[18] and b) bulk single crystal of BFO, adapted from[19]. Unlike many other compounds, they show the same quality and similar polarization values.

In general, ferroelectricity can appear as a primary effect (polarization being the main order parameter in the material) in the so-called *proper ferroelectrics*, or as a result of a primary symmetry breaking of a different character that in turn produces an electrical dipole (polarization being a secondary order parameter), as in *improper ferroelectrics*. In multiferroics with large magnetoelectric coupling, the observed ferroelectricity is often improper and induced by the magnetic order, which is the primary order parameter. Proper ferroelectrics can also be generally categorized according to several mechanisms. Here, we treat the specific category of oxides with a perovskite structure which typically show so-called *displacive ferroelectricity*: shift of ions below the ordering temperature while the ions remain in the high symmetry position above the ordering temperature. This happens due to their covalent bonding interactions. In BaTiO_3 , for example, the electron density of the filled oxygen $2p$ orbitals partially transfers to an empty $\text{Ti}^{4+} 3d^0$ orbital on the octahedral B-site, which gives rise to a polar lattice distortion. In other displacive ferroelectrics such as PbTiO_3 or BiFeO_3 the Pb/Bi lone pair introduces another type of distortion[2; 20–22]. In this case, the stereochemical activity of the ns^2 lone pair in A-site plays a dominant role resulting in off-centered distortion that give rise to a permanent polarization density. In reality, there seems to be

always an order-disorder components even in these mainly displacive ferroelectrics. In the case of BFO, the ferroelectric ordering temperature occurs at 825°C and it is a first-order (discontinuous, involving latent heat and thermal hysteresis) paraelectric-ferroelectric phase transition, accompanied by a cubic-orthorhombic structural phase transition. Moreover, BFO is a proper ferroelectric with the largest existing electrical polarization.

1.4.2 Ferroelasticity

Spontaneous strain is the driving order parameter in ferroelastic materials. Unlike ferroelectrics or ferromagnets, the order parameter in a ferroelastic material is not a vector, but a second rank tensor. This brings about various interesting consequences, such as the absence of 180° domain walls (DWs) in a purely ferroelastic material, because inversion symmetry cannot be broken in the strain tensor[23]. Nevertheless, 90° domains (or twins) can form in pure ferroelastic domains[24]. Moreover, tetragonal $\text{PbZr}_{1-x}\text{Ti}_x\text{O}_3$ or PbTiO_3 with two perpendicular strain components are an example of ferroelastic-ferroelectric materials [25]. In the case of rhombohedral BFO, all the non- 180° DWs (109° and 71° DWs) are both ferroelectric as well as ferroelastic. That is, they separate domains that are both ferroelectric and ferroelastic due to the coupling between polarization and strain.

Since DWs are regions of symmetry breaking, they offer additional possibilities for multiferroic behaviour. A complete study on possible ferroelectric and ferroelastic coupling (those that satisfy the rules of mechanical and electrical compatibility among adjacent domains) has been provided by Fousek and Janovec[26; 27].

1.5 BiFeO₃

1.5.1 Characterization

The crystal structure of BFO at room temperature is rhombohedral with $R3c$ as the space group. The lattice parameters are $a_{rh} = b_{rh} = c_{rh} = 3.965 \text{ \AA}$ and the rhombohedral angle is 89.4° , as plotted in figure 1.1, the often used hexagonal axes are also drawn in figure 1.1. The symmetry defines the direction of ferroelectric polarization to lie along the body diagonal of the unit cell, along $[111]$ direction. The first experimental value for the *remanent*

polarization, P_r was reported by Teague *et al.*, as $0.6\mu\text{C}/\text{cm}^{-2}$ [28]. As discussed in the previous section, the Goldschmid tolerance factor measures the distortion of the perovskite from cubic symmetry. When this factor is smaller than 1, the oxygen octahedra buckle. The octahedral rotation around the polar [111] axis alters the Fe-O-Fe angle, affects the magnetic ordering temperature and the conductivity. In bulk, there is volume contraction, at the onset of the orthorhombic phase[29] above the first order ferroelectric transition temperature (around 825°C). In addition, different structural phase transitions can be obtained by tuning the pressure[30], temperature[31] and chemical doping[32; 33]. A tentative phase diagram versus temperature and pressure has been proposed by Catalan *et al.*, which is shown in figure 1.4.

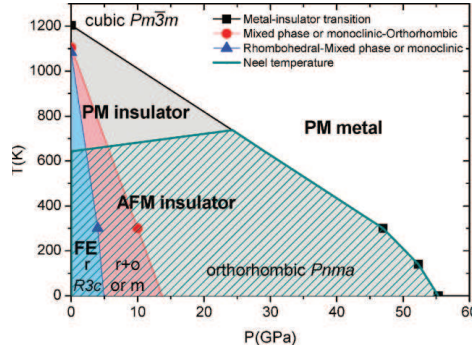


Figure 1.4: Sketch of possible phase diagram as a function of pressure and temperature. Adapted from[3].

BFO in bulk is highly resistive $\rho=10^{10}$ Ohm.cm[31; 34]. Temperature dependent resistivity reveals a semiconductor like activated behaviour. Moreover, there is a change in activation energy above 370°C (magnetic ordering temperature) which shows a correlation between the bandgap and the magnetic ordering, suggesting the possibility of magnetoresistivity in BFO. At higher temperatures, resistivity anomalies coincide with structural changes[31; 35; 36]. BFO is theoretically predicted to be a semiconductor with a band gap of 2.8eV at room temperature[31; 37]. The band gap is controlled by the orbital overlap between the O 2p and the Fe 3d levels. However, experimentally, there are several reports on the existence of both direct and indirect band gaps in BFO. The former is 2.3-2.8eV[31; 34; 38] and the latter is 0.4-1eV[34; 38]. A smaller band gap

can be attributed to enhanced orbital overlap, typical for a straightened Fe-O-Fe angle. This angle can be controlled by a ferroelectric distortion and it is straightened by temperature enhancement[31; 39].

1.5.2 Thin films of BiFeO₃

BFO is one of the few materials for which high-quality film samples existed before high-quality bulk samples were ever synthesized. It is now the case that a crystal is considered a "good crystal" if it is as good as a film. This is a big break-through for the thin film community. However, the crystal structure of epitaxial films is different from that of the bulk. When BFO is under slight compressive strain, it becomes monoclinic, reported by several groups[40–43]. This symmetry arises by elongating one of the axes of the rhombohedral unit cell, in this case by strain due to lattice mismatch between substrate and film. Since this monoclinic distortion is rather small, we often call this distortion "pseudo-rhombohedral". Nevertheless, BFO has a more complex dependence with strain[44] and thickness[45]. It has been shown that BFO under strain has a very rich phase diagram with many different, previously unknown phases[46].

Despite the many recent reports on BFO, there are still many unknowns and some controversial issues: depending on the report, the obtained critical thickness for the tetragonal phase varies from 10 to 100nm in different reports; Piezo Force Microscopy analysis does not seem compatible with the structural analysis. This incompatibility could be explained by the decoupling between crystal class and internal symmetry, as has been observed for other perovskite system under strain[47; 48]. It is worth to mention that BFO has a relatively small piezoelectric constant[19]. This means that the magnitude of the polarization does not depend strongly on strain. Nonetheless, polarization can be rotated within the (110)_{pc} plane thanks to the monoclinic symmetry induced by strain effect[49].

1.6 Domains

The presence of polarization in ferroelectrics induces surface charges that if they were unscreened, they would result in a depolarization field. The depolarization field increases with decreasing thickness (as 1/d) and thus its effect is mainly relevant in thin films[50]. The surface charges can be screened by external or internal charges, to prevent depolarization and the

cancellation of ferroelectricity in the film. Adsorbates from the atmosphere on the surface of the sample, good electrodes, or charged defects in the material can supply the compensation of the polar charges, therefore allowing ferroelectricity in very thin films.

Additionally, another way to cancel out the surface charges is dividing the ferroelectric state into regions with opposite polar orientations. In this way the average polarization is zero but the material remains locally polar and can be ferroelectric (if switching can be achieved)[23]. We call these regions with different polar orientations, all having the same energy "domains". In the case of BFO with its rhombohedral symmetry at room temperature, there are 8 energetically equivalent domains, shown in figure 1.5 a). In bulk, the domains appear randomly and it is difficult to control them, but in thin film form, both electrical and mechanical boundary conditions, such as the atomic termination of the substrate, its electrical properties and the lattice mismatch between film and substrate or the thickness, can be tuned to control the number of domains as well as the preferred polarization direction inside the domains. The energy penalty incurred by the lattice deformation (strain) scales linearly with the film thickness. If the elastic energy becomes too large for large enough thicknesses, the film can relax, forming domains. However, creating domains and domain walls also cost energy. Therefore, the system has to balance the cost of creating a domain wall versus the energy cost of increasing the thickness of a strained layer. That balance determines the domain wall density or, in other words the domain size (w) as a function of thickness(d). Roytburd found out that for relatively large thicknesses (with some approximations), the ferroelastic domain width was proportional to the square root of the thickness ($w \propto \sqrt{d}$)[51], the same dependence that Kittel found for ferromagnetic domains[52]. This allows great tunability of domain formation in thin film form. After defining the concept of domains, we can move on to the domain wall section.

1.7 Domain walls

Two domains are separated by a DW. The width of the walls is inversely proportional to the anisotropy of the order parameters since typically ferroelastics are highly anisotropic, their DWs are atomically thin, which is very different from most ferromagnets having DWs of tens or hundred nanometers in width. The DWs between ferroelastic domains are very in-

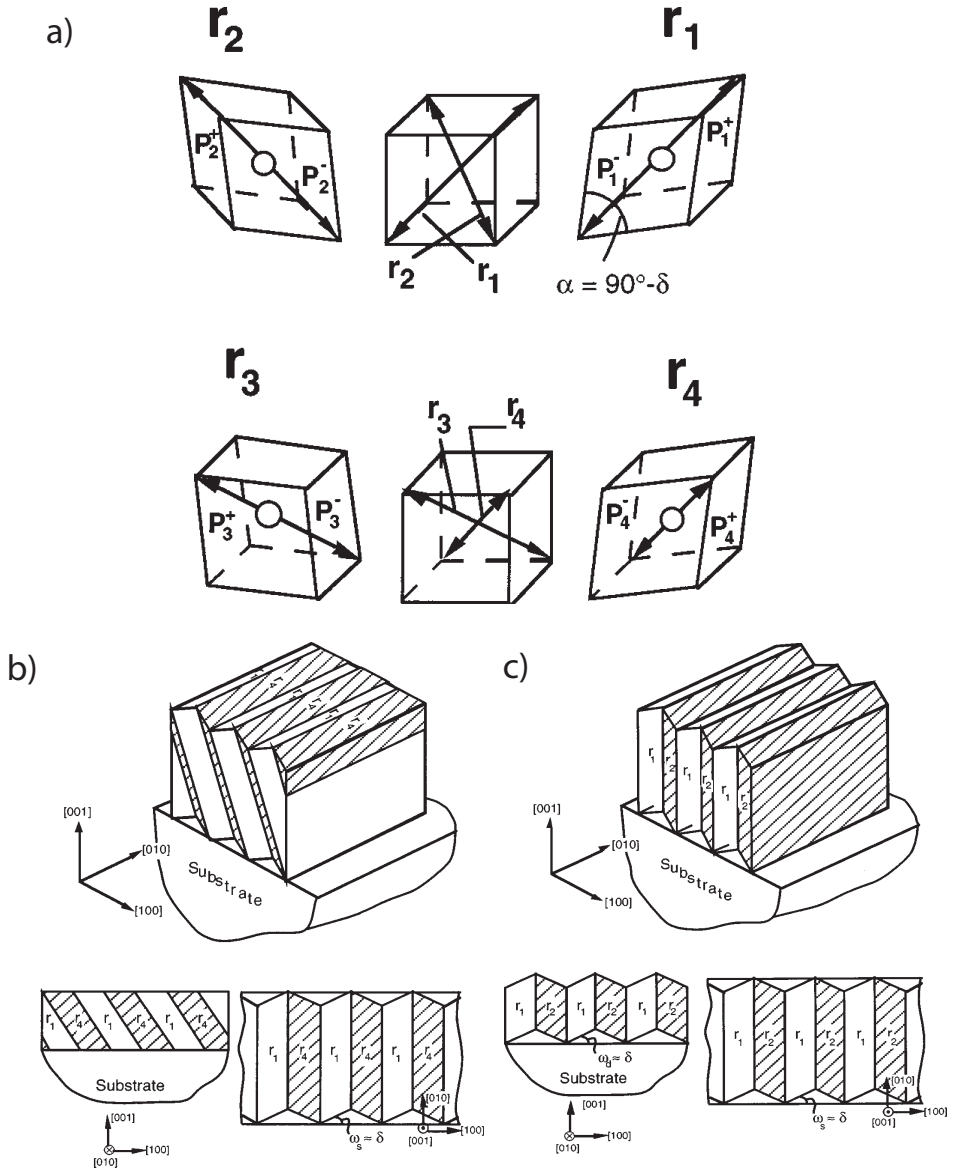


Figure 1.5: a) 4 structural (r_1, r_2, r_3, r_4) and 8 polarization variants in a prototypical rhombohedral perovskite phase, b) perspective, side and plan view of 71° and c) 109° DWs, taken from [53].

interesting because they display large strain values concentrated in a nano-scale region, that is, they display very large strain gradients, and they break the crystal symmetry, which can give rise to different properties compared to those present in the domains. In the case of BFO, the rhombohedral distortion and the 8 possible polar directions (body diagonals of the perovskite unit cell), allows three types of DWs. The analysis of possible domain walls in rhombohedral perovskites was reported by Streiffer *et al.*,[53; 54]. The walls are named after the angle formed by the polar vectors in the two adjacent domains: 71° DW, 109° DW and 180° DW. In figure 1.5 the first two walls (most relevant for the present thesis) are described in detail[53; 54]. These are ferroelectric, as well as ferroelastic DWs.

Depending on the orientation of the existing polar vectors inside the domains, a DW can be neutral or charged[55]. The charged walls can be either head-head or tail-tail, which influence the size of the DWs. In 2008 Jia *et al.*, could evidence the existence of charged DWs by means of High-resolution transmission electron microscopy[56]. It has been postulated that in order to screen the depolarization field produced by neighboring polar domains, a reasonable amount of carriers has to be present in the walls. Because of that different DWs would have different width, being the neutral, head-head and tail-tail DWs (for n-type BFO) in order of narrowest to broadest, respectively[57]. There are more parameters, such as susceptibility and/or anisotropy as discussed earlier, that have influence on the width of a DW.

However, in multiferroic materials, the thickness of a DW depends on the strength of the coupling between the order parameters. For instance, if the coupling is weak, like in ferroelectric and antiferromagnetic YMnO_3 [58].

In BFO, there are two order parameters with two different correlation lengths with a moderate coupling between the order parameters, which results in broader ferroelectric DWs compared to normal ferroelectrics[59]. As discussed in the first part of this section, this narrowest known feature in ferroic materials -the DW- has its own phase transitions, as realized for the first time by Lajzerowicz and co-workers[60]. Indeed, since the free energy in the DW is different compared to those in the domains, one could expect that the thermodynamical properties and phase transitions should be different[23]. In addition, space group symmetry arguments in "a-priori non-ferroelectric materials" can be used to predict that 128

classes of materials can exhibit spontaneously non - zero net magnetization and/or polarization at the DWs[26]. One of the studied space groups was R3c (the space group of BFO) which allows magnetization at the walls[26]. Symmetry analysis is a necessary but not sufficient criterion; the next step is the investigation of the magnitude of the studied property which is allowed by symmetry. The underlying symmetry change in a DW causes changes in the electronic structure and hence, changes in transport properties which will be discussed further in the next section.

1.7.1 Domain wall transport

Significantly different conduction properties at domains and walls were first discovered by Salje and coworkers who evidenced superconductivity in twin walls in WO_3 . Salje *et al.*, explained their observation by the ability of twin walls to attract defects. This gives rise to preferential doping along the walls and causes the appearance of selective conduction paths along the twin walls[61]. Recently, local transport properties were investigated in non-doped multiferroics. The first observation was on thin films of BFO[62] and showed that artificially written DWs show a higher conduction level compared to that of the domains and that the conduction level is tunable by changing the chemistry state at the walls in La-doped thin films of BFO[63]. While, one year later, Choi *et al.*, showed exactly the opposite in improper ferroelectric YMnO_3 that the DWs are less conductive than the domains[64]. Catalan *et al.*, interpreted this contrast by considering paraphaselike behavior in addition to polarization considerations[23]. These works motivated large part of this thesis. A difference in the conduction level between domains and DWs has been observed in the as-grown state of thin films of BFO[65; 66]. But conduction phenomenon is not specific for ferroelastic walls. Recently, conduction has been reported in ferroelectric (but non-ferroelastic) DWs in thin films of $\text{Pb}(\text{Zr},\text{Ti})\text{O}_3$ [67] and also in improper ferroelectric single crystals of ErMnO_3 [68] and HoMnO_3 [69].

Apart from conduction phenomena, other transport properties have also been investigated. In one of the earliest experiments (antiferromagnetic) BFO was brought in contact with a soft ferromagnetic (permalloy) layer, and exchange bias proportional to the number of 109° DWs is observed[70]. In the same type of DWs, the photovoltaic effect has been observed as well[71]. Further investigation on the same family of samples illustrated that DWs function as nanoscale generators of the photovoltaic

current[72]. Very recently, the magnetoresistance effect as large as 60% in array of 109° DWs was measured[73].

1.7.2 Origin of domain wall conductivity

The conduction behaviour of BFO domain walls has been explained in two ways: on one hand, by the reduction of the band gap at the wall. On the other hand, electrostatic potential changes caused by the structural variations is the other driving force[74]. Yet, the concept of band gap for a DW is obscured because of its finite width[75]. Nonetheless, the possibility of complete hybridization between Fe 3d and 2p can lead to straightening of Fe-O-Fe bond angle, which results in band gap decrease at the walls[23]. Lubk and coworkers have calculated the potential steps at the twin walls of BFO due to rotation of the polar vector normal to the walls[74], this potential drop creates a large electric field where electrons and oxygen vacancies concentrate in two opposite sites of the wall which clearly implies charge aggregation around the wall and hence, a higher level of conduction at the walls. Catalan *et al.*, [23] summarizes some of the possible origins of conduction at the walls in thin films of BFO and other oxides as follows: octahedral rotations, electrostatic steps because of rigid rotation of the polar vector, and increased carrier density at the wall. One more consideration which has to be taken into account is the mutual interplay between vacancy content (oxygen anions and/or cations) and conductivity at the walls[63; 76]. The role of oxygen vacancies has been put forward using electron-energy-loss spectroscopy (EELS) and TEM analysis by Jia *et al.*, in the case of BaTiO₃ twin boundaries[77]. This has been emphasized by Salje *et al.*, as well[78].

1.8 Conduction mechanisms

In order to design new devices and devise novel approaches to the application and engineering at nanoscale, one needs to understand the underlying mechanisms in the transport properties. Transport properties in semiconducting BFO are extensively studied in this thesis. Here, we introduce different types of conduction mechanisms in semiconductors.

1.8.1 Thermionic emission at interfaces and Poole-Frenkel emission in bulk

Conduction through interfaces has been studied for a long time. Common examples of interfaces are the ones between a metal and a vacuum, a metal and an insulator or a DW with a top or bottom electrode. Typically, a Schottky barrier develops at an interface between the electrode and semiconductor due to the difference in the work function of the metal and electron affinity of the semiconductor. Applying different metals as the electrode results in a different height of the Schottky barrier. Assuming a larger work function for the electrode than the electron affinity of the semiconductor, electrons inject from the top electrode to the semiconductor.

Already in 1942, Bethe[79] formulated the thermionic-emission theory for rectifying metal-semiconductor contacts. In the model it was assumed that the potential barrier height was larger than the thermal energy $k_B T$ of charge carriers that surmount a barrier with height $q\phi_B$. In addition, it is assumed that the interface through which charge carriers are emitted, is in thermal equilibrium. The magnitude of the thermionic emission current depends entirely on the barrier height. Charge carriers obey Fermi-Dirac statistics. A fraction of the charge carriers will attain energy levels that are high enough to traverse the potential barrier. The thermionic current density is proportional to:

$$J = AT^2 \exp\left(\frac{-q\phi_B}{k_B T}\right) \exp\left(\frac{qV}{k_B T}\right) \quad (1.2)$$

Here A is the Richardson constant $\frac{4\pi q m k^2}{h^3}$, $q\phi_B$ is the barrier height. Several adaptations to this general form have been developed that are valid in special limiting cases. As mentioned earlier, here, we discuss several conduction mechanisms with a particular focus on conduction through semiconducting/insulating solids. The exact conduction mechanism depends on whether the conduction is bulk or interface limited. We distinguish Nordheim tunneling, Poole-Frenkel emission, Simmons-Richardson-Schottky emission behavior and discuss how to recognize the relevant conduction mechanism. In addition, conduction can be limited by space charge.

When the mobility is high and the recombination velocity at the potential barrier maximum is dominant, the Bethe equation reduces to the "standard Schottky" equation, which describes an interface limited conduction mechanism.

$$J = AT^2 \exp\left(\frac{-\phi}{kT}\right) \exp(\beta_0 E^{1/2}) \quad (1.3)$$

Where $\beta_0 = \frac{q}{kT} \left(\frac{q}{\pi\epsilon_0 K}\right)^{0.5}$, ϵ_0 is the permittivity of free space, K is the dielectric constant and E is the field at the interface.

In contrast, a low carrier number reduces the Bethe equation to the Simmons equation. Simmons *et al.*, [80] noted that the standard Richardson-Schottky equation is less suitable for solids in which the electronic mean free path is very small, which is typical for insulating solids. He therefore suggested a modified "Richardson-Schottky-Simmons" version with an additional pre-exponential factor to take into account the small electronic mean free path. The devised "Richardson-Schottky-Simmons" equation has been formulated as follows:

$$J = A \left(\frac{2\pi m}{k}\right)^{1/2} (T)^{3/2} E \exp\left(\frac{-\phi}{kT}\right) \exp(\beta_0 E^{1/2}) \quad (1.4)$$

The Poole-Frenkel conduction mechanism is a bulk limited conduction mechanism mediated by charge carrier hopping between defect sites (localized states) assisted by an electric field. The electric field assists the trapped charge carriers in a thermal ionization process. The Coulomb potential barrier is effectively lowered in the presence of an electric field. In this conduction mechanism, trapped charge carriers are released by thermal emission, assisted by an electric field E that effectively lowers the potential barrier of the trap. The Poole-Frenkel conduction mechanism shows a similar behaviour as the Schottky mechanism (field dependence).

$$J = \sigma_o \exp\left(\frac{-E_t}{kT}\right) \left(\sqrt{\frac{e^3}{\pi\epsilon\epsilon_\infty}}\right) \sqrt{E} \quad (1.5)$$

where E_t is the trap energy.

This makes it more complicated to distinguish between these two types of mechanisms. The main difference is that a Poole-Frenkel conduction mechanism is bulk limited, whereas Schottky is an interface limited conduction mechanism. This means Schottky mechanism should not depend on thickness and therefore, a thickness dependence would help distinguishing between the two. Another way to recognize which of the two of the mechanisms is present is to extract the high frequency dielectric constant should be extracted, which should be in agreement with expectations.

1.8.2 Fowler Nordheim tunneling

Fowler Nordheim tunneling is an interface limited conduction mechanism. Tunneling is a purely quantum mechanical phenomenon, and can only be described when the wave nature of the tunneling particle is taken into account. The wavefunction of a tunneling charge carrier, protrudes into the potential barrier region. The tunneling probability is proportional to the exponentially decaying probability amplitude of the wavefunction. Provided that the potential barrier is thin enough, a carrier can traverse a potential barrier even though the particle energy is lower[81]. The height of the potential barrier can be adjusted with a locally applied remanent electric polarization. The remanent polarization could be used to adjust the potential barrier height to control the magnitude of the tunneling current. Tunneling is employed in Josephson junctions, Esaki diodes and flash memory[82]. Evidence for a Fowler Nordheim tunneling mechanism can be obtained by plotting $\ln(J/E^2)$ versus E^{-1} for different temperatures, followed by the formula below,

$$J = A_{eff} A \frac{E^2}{\varphi_B} \exp\left(\frac{-8\pi\sqrt{2m_{FE}}}{3hq} \frac{\varphi_B^{3/2}}{E}\right) \quad (1.6)$$

As can be obtained from the formula, this gives a linear dependence with a slope that should be temperature independent.

1.8.3 Space charge limited conduction current

The presence of accumulated charge carrier density in a volume causes an electric field that reduces the rate of emission and conductivity. Space charge limited conduction processes show a typical quadratic voltage dependence:

$$J = \frac{8}{9} \epsilon_0 \mu \frac{V^2}{L^3} \quad (1.7)$$

where μ is the carrier mobility and ϵ_0 is the relative dielectric constant. The quadratic voltage dependence of space charge limited conduction can be obtained from a double logarithmic plot. Slopes slightly larger than 2 can occur in the presence of traps.

Bibliography

- [1] N. A. Hill, *J. Phys. Chem. B* **104**, 6694 (2000).
- [2] R. E. Cohen, *Nat.* **358**, 136 (1992).
- [3] G. Catalan and J.F. Scott, *Adv. Mat.* **21**, 2463 (2009).
- [4] J.F.Scott, *Ferroelectrics* **95**, 166 (1995).
- [5] S.C. Abrahams and J. Ravez, *Ferroelectrics* **21**, 135 (1992).
- [6] J. Ravez, *J. Physique III* **7**,1129(1997).
- [7] G. Nenert and T. T. M. Palstra, *J. Phys.: Condens. Matter.* **19**, 406213 (2007).
- [8] V. Goldsmidt, *I. Mat.-Nat.* **K1** (1926).
- [9] R.D. Shannon and C.T. Prewitt, *Acta Crystallogr. Sec.B* **25**,925 (1969).
- [10] S.W. Bailey et al.,*Acta Cryst. A* **33**, 681 (1977).
- [11] J.W. Matthees and A.E. Blakeslee, *J. Crystal Growth.* **27**, 118 (1974).
- [12] X. Pompe et al., *J of Appl.Phys.* **74**, 6012 (1993).
- [13] J.S. Speck and W. Pompe, *J of Appl.Phys.* **76**, 446 (1994).
- [14] B.B. Van Aken et al., *Nat.* **449**, 09139 (2007).
- [15] V.L. Ginzburg et al., *Solid State Commun.* **50**, 339 (1984).
- [16] I. Sosnovska et al., *J. Phys. C.* **15**, 4835 (1982).

- [17] F. Bai et al., *Appl. Phys. Lett.* **86**, 32511 (2005).
- [18] D. Lebeugle et al., *Appl. Phys. Lett.* **91**, 022907 (2007).
- [19] J. Wang et al., *Science* **299**, 1719 (2003).
- [20] Z. Wu and R. E. Cohen, *Phys. Rev. Lett.* **95**, 903760 (2005).
- [21] N.A. Hill, *Annu. Rev. Mater.* **32**, 1 (2002).
- [22] J. Ravez, *Acad. Sci. Paris, IIc Chem.* **3**, 267 (2000).
- [23] G. Catalan et al., *Rev. Mod. Phys.* **84**, 1 (2012).
- [24] E.K.H. Salje et al., *Ferroelectrics* **223**, 1 (1999).
- [25] E.K.H. Salje, *Phase transition in ferroelastic and co-elastic crystals*, Cambridge university press (1993).
- [26] V. Janovec et al., *Ferroelectrics* **222**, 73 (1999).
- [27] J. Fousek, and V. Janovec, *J. Appl. Phys.* **40**, 135 (1969).
- [28] J.R. Teague et al., *Solid State Commun.* **8**, 1073 (1970).
- [29] J.D. Bucci et al., *J. Appl. Cryst.* **5**, 187 (1972).
- [30] R. Haumont et al., *Phys. Rev. B* **79**, 184110 (2009).
- [31] R. Palai et al., *Phys. Rev. B* **77**, 014110 (2008).
- [32] M. Polomska et al., *Phys. Stat. Sol.* **23**, 567 (1974).
- [33] M. Polomska and W. Kaczmarek, *Acta Phys. Polonica A* **45**, 199 (1974).
- [34] T.P. Gujar et al., *Mater. Chem. Phys.* **103**, 142 (2007).
- [35] M.I. Morozov et al., *Russ. J. Gen. Chem.* **73**, 1680 (2003).
- [36] S.M. Selbach et al., *Chem. Mater.* **19**, 6478 (2007).
- [37] S.J. Clark and J. Robertson, *Appl. Phys. Lett.* **90**, 132903 (2007).
- [38] V. Fruth et al., *J. Eur. Ceram. Soc.* **27**, 937 (2007).

- [39] A. Palewicz et al., *Acta Cryst. B* **63**, 537 (2007).
- [40] J. Li et al., *Appl. Phys. Lett.* **95**, 5261 (2004).
- [41] G. Xu et al., *Appl. Phys. Lett.* **86**, 182905 (2005).
- [42] S. Keisuke et al., *Jpn. J. Appl. Phys.* **45**, 7311 (2006).
- [43] G.Y. Xu et al., *Appl. Phys. Lett.* **89**, 222901 (2006).
- [44] H.M. Christen et al., *Phys. Rev. B* **83**, 144107 (2011).
- [45] C.J.M Daumont et al., *Phys. Rev. B* **81**, 144115 (2010).
- [46] O. Dieguez et al., *Phys. Rev. B* **83**, 094105 (2011).
- [47] F. He et al., *Phys. Rev. Lett.* **94**, 176101 (2005).
- [48] G. Catalan et al., *Phys. Rev. Lett.* **96**, 127602 (2006).
- [49] H.W. Jang et al., *Phys. Rev. Lett.* **101**, 107602 (2008).
- [50] J. Junquera P. Ghosez, *Nat.* **422**, 506 (2003).
- [51] A. Roytburd, *Phys. Stat. Sol. A* **37**, 329 (1976).
- [52] C. Kittel, *Phys. Rev.* **70**, 965 (1946).
- [53] S.K. Streiffer et al., *J. Appl. Phys.* **83**, 2742 (1998).
- [54] S.K. Streiffer et al., *J. Appl. Phys.* **83**, 2754 (1998).
- [55] M.Y. Gureev et al., *Phys. Rev. B* **83**, 184104 (2011).
- [56] C.-L. Jia et al., *Nat. Mater.* **7**, 57 (2008).
- [57] E. Eliseev et al., *Phys. Rev. B* **83**, 235313 (2011).
- [58] M. Fiebig et al., *J. Magn. Magn. Mater.* **353**, 272 (2004).
- [59] G. Catalan et al., *Phys. Rev. Lett.* **100**, 027602 (2008).
- [60] J. Lajzerowicz et al., *J. Phys. Lett.* **40**, 165 (1979).
- [61] E.K.H. Salje. *Chem. Phys. Chem* **11**, 940 (2010).
- [62] J. Seidel et al., *Nat. Mater.* **8**, 229 (2009).

- [63] J. Seidel et al., Phys. Rev. Lett. **105**, 197603 (2010).
- [64] T. Choi et al., Nat. Mater. **9**, 423 (2010).
- [65] Y.-P. Chiu et al., Adv. Mater. **23**, 1530 (2011).
- [66] S. Farokhipoor and B. Noheda, Phys. Rev. Lett. **107**, 127601 (2011).
- [67] J. Guyonnet et al., Adv. Mater. **23**, 5377 (2011).
- [68] D. Meier et al., Nat. Mater. **11**, 284 (2012).
- [69] W. Wu et al., Phys. Rev. Lett. **108**, 077203 (2012).
- [70] L.W. Martin et al., Nano Letters. **8**, 2050 (2008).
- [71] S.Y. Yang et al., Nat. Nanotech. **5**, 143 (2010).
- [72] J. Seidel et al., Phys. Rev. Lett. **107**, 126805 (2011).
- [73] Q. He et al., Phys. Rev. Lett. **108**, 067203 (2012).
- [74] A. Lubk et al., Phys. Rev. B **80**, 104110 (2009).
- [75] M. Alexe, Private communication.
- [76] S. Farokhipoor and B. Noheda, J of Appl. Phys. **112**, 052003 (2012).
- [77] C.L. Jia and K. Urban, Science **303**, 204 (2001).
- [78] E.K.H. Salje and H. Zhang, Science **82**, 452 (2009).
- [79] S.M. Sze, Physics of semiconductor devices, John Wiley and Sons (1981).
- [80] J.G. Simmons, Phys. Rev. Lett. **155**, 657 (1967).
- [81] G.D. Mahan et al., Condensed matter in a nutshell, Princeton university press, 355, (2011).
- [82] P. Maksymovych et al., Science 324, 1421 (2004).

Chapter 2

Experimental techniques

2.1 Abstract

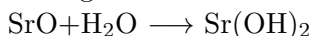
This chapter describes the thin film deposition process and characterization techniques that have been employed for the BiFeO_3 thin films on SrRuO_3 buffered SrTiO_3 substrates that are studied in this thesis. The described techniques will be routinely used in the subsequent chapters. We present a gamut of different measurement techniques that probe physical properties at different length scales to provide a complementary picture of the physics of the thin film. We discuss Pulsed Laser Deposition (PLD) technique and surface sensitive Reflection High Energy Electron Diffraction (RHEED) which is used to follow in situ the deposition and growth process, X-ray diffraction (XRD) to study the crystalline film over extended length scales. More local probes such as Atomic Force Microscopy (AFM) provide detailed information about the surface topography of the thin film. In this thesis, we focus on the interrelationship between microstructure and local physical properties. We provide an overview of less common techniques based on AFM that have been developed to allow local physical properties to be mapped out: Piezo Force Microscopy (PFM) and Conductive Force Microscopy (CFM) are employed to study local ferroelectric and transport properties in the vicinity of microstructural phenomena such as domain walls. With these techniques, we elucidate the relationship between microstructure and local physical properties.

2.2 Substrate treatment

The single crystal substrate onto which the films are grown should have suitable structured lattice parameters similar to those of the crystalline film that will be grown. The lattice mismatch between the two determines the strain and the defect or domain wall density. All samples have been grown on the (001) surfaces of the perovskite SrTiO₃ (STO) with a lattice parameter of $a=3.905\text{\AA}$. All the substrates had a miscut angle of less than 0.1 degree. The preparation of surfaces and the stoichiometry are the two most critical conditions for film growth. The (100) STO surface receives chemical treatment before thin film deposition. The chemical treatment results in an atomically flat single terminated TiO₂ (100) surface[1]. The procedure can be formulated in the following way;

Rinsing 20 min in acetone + ethanol

Reacting 30 min with water



Etching 30 second with HF



Thermal treatment at 960°C oxygen atmosphere for $1\text{hr} \leq t \leq 2\text{hrs}$

The exact annealing time depends on the length of terraces (L) which can be determined from the miscut angle α as $L=a \tan\alpha$, being a the step (unit cell) height. If the annealing time exceeds the optimal time, double-termination occurs on the surface. Figure 2.1 a) and c) shows AFM topography images of the terraces in two and three dimension, respectively. The treated surface shows unit cell size steps of 4\AA (figure 2.1 b)). For all the films grown on STO substrates in this work, the same procedure for substrate treatment was followed.

2.2.1 Pulsed Laser Deposition

Pulsed Laser Deposition (PLD) was introduced by Smith and Turner as a versatile tool to grow thin films in a controlled way. Compared to MBE, PLD offers the advantage that the growth of oxide thin films can be controlled in a wider deposition parameter range. PLD is typically performed at higher oxygen pressure. This allows higher substrate temperatures in PLD which leads to improved crystallinity of the grown films. In the absence of an oxygen background pressure, the higher substrate temperatures would lead to endothermic oxygen release of the thin film. Therefore, the

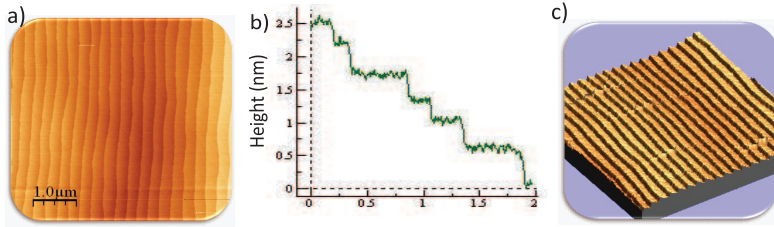


Figure 2.1: a) and c) Typical AFM topography two and three dimensional image for a single terminated (001) substrate with TiO_2 as the last termination. b) Line profile along the steps which is evidence for 4 Å height steps as well as flat terraces.

higher oxygen pressure is required to prevent oxygen vacancies. A further advantage of PLD is that the stoichiometry of the target is retained in the plasma plume after ablation.

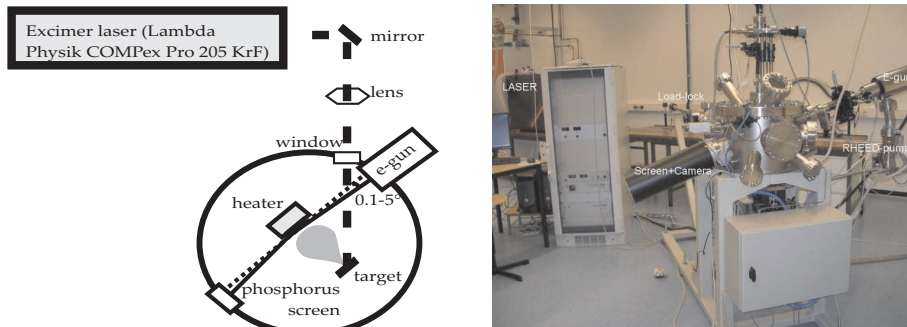


Figure 2.2: Top view sketch of the PLD set-up, used in the Nanostructures of Functional Oxides group of University of Groningen. Sketch taken from A.H.G. Vlooswijk thesis, Groningen University, (2009).

The setup that is used to grow films with PLD is shown in a simple sketch in figure 2.2. It consists of 1) high vacuum chamber (background pressure of 10^{-7} to 10^{-8} mbar), that contains: 2) a target to be ablated which is located inside the vacuum chamber, 3) the heater where the substrate is glued and it is used to set the sample at the proper growth temperature and for annealing, 4) the optical path (including lens and mirrors), which is located outside the chamber to focus the laser on the target, 5)

an ablation laser which is directed at a polycrystalline target, 6) RHEED, camera and phosphorescent screen to monitor the growth while the deposition takes place. The source material is ablated from a target with an intense focused Lambda PhysiK COMPex Pro 205 KrF excimer laser pulse ($\lambda = 248\text{nm}$, $\tau = 25\text{ns}$) with a controllable repetition rate. In this UV wavelength region, the target material shows strong absorption. As a consequence, the laser pulse both heats and ionizes the ablated material. This process is the so called ablation process. To retain the stoichiometry of the ablated plume the same as that of the target, the laser energy density should be determined carefully with respect to the other growth conditions, in order to prevent preferential ablation (or incongruent deposition)[2]. A low laser fluence leads to simple evaporation of the topmost layers of the target, whereas a high laser fluence generates a plasma. For the series of the films grown in this thesis, the used energy density is around 2 J/cm^2 and the laser voltage varies between 19kV - 24kV . The wavelength of the excimer laser, the laser power density, pulse repetition rate and pulse duration determine the ablated material flux and hence the growth rate.

The generated plasma plume is deposited on a heated substrate attached to a heater with silver paste to enable heat transport. The growth takes place in an UHV chamber that is pumped down to ultra high vacuum base pressure of 10^{-7} mbar and then filled with oxygen to a pressure of 0.1 - 0.3 mbar. The oxygen gas fulfils two functions: the oxidizing gas interacts with the plasma to form molecular species and limits the kinetic energy of the plasma species. The oxygen gas pressure determines the dimensions of the ablated plume and as a consequence the deposition rate and uniformity. The oxygen pressure controls the kinetic energy of the adatoms as they arrive at the surface. Inelastic collisions with the gas molecules change the kinetic energy distribution of ablated atoms arriving at the surface. The oxygen pressure controls the activation energy of the diffusion of the adatoms. We distinguish two different phases in one operational cycle: The deposition of ablated material during the laser pulse and when the shutter is closed, the subsequent growth of the film to monolayer coverage when the adsorbed particles can arrange and diffuse along the surface (plasma phase transits to crystalline phase). During the deposition pulse, islands grow that subsequently coalesce when the shutter has closed. At this time, adatoms migrate to the island edges with a characteristic relaxation time. Layer-by-layer growth is the generally preferred growth mode because it leads to atomically flat surfaces and allows the control of the growth atomic

layer by atomic layer. To ensure layer-by-layer growth, special care has to be taken to choose the right deposition conditions. The kinetic energy of the plasma particles can be accurately controlled. The amount of material deposited in each pulse, the substrate temperature and oxygen pressure are the most important parameters to control the nucleation behaviour at the surface.

Thermodynamically, we can distinguish three growth modes: (1) Frank-Van der Merwe or layer-by-layer growth, (2) Volmer-Weber growth or island growth and (3) Stranski-Krastanov growth. Stranski-Krastanov growth mode is an intermediate form in which a combination of island growth and layer by layer growth occurs, shown in figure 2.3. In this case the first monolayers are fully covered, and then a change in growth mode to island growth occurs.

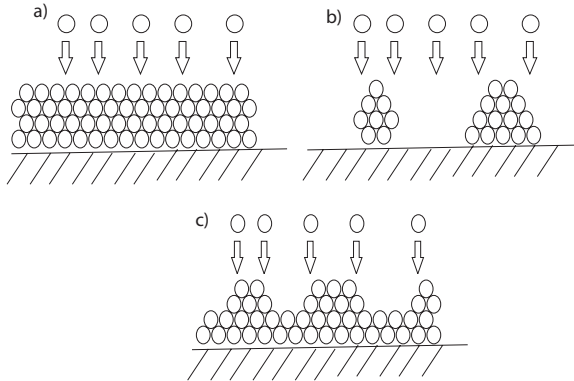


Figure 2.3: Typical thin film growth modes close to thermodynamics equilibrium. a) layer by layer growth (Frank-Van der Merwe), b) 3D island growth (Volmer-Weber), c) Stranski-Krastanov[3].

Which mode takes place depends on the relative surface energy of the substrate and film. However, in general, the growth mode depends not only on surface energies but also on nucleation kinetics. For PLD the latter is more important as the system is not in thermodynamic equilibrium during growth. Thus, the morphology of the as-deposited film is not controlled by thermodynamical factors such as the surface energies, thin film energy or the interface between substrate and film. Instead, kinetics determines the prevailing growth mechanism. The deposited adatoms can move along the island surface to the edge with a characteristic diffusion length described

as $l_{th} = \sqrt{c * \tau}$, with τ as a measurable characteristic relaxation time. Sufficient lateral mobility of the adatoms without the coalescence of these individual islands is not possible. The exact growth mode and growth rate are determined by the kinetic energy of the species arriving at the surface. A too low substrate temperature limits the diffusion of species arriving at the surface, leading to cluster formation. Too high temperature prevents the adsorption. A change in the substrate temperature results in a change of the number of nucleation islands and a change in diffusivity of the absorbed adatoms[3].

The in-house PLD has in-situ High Energy Electron Diffraction (developed by TSST industrial group and Twente University, the Netherlands[4]). It will be further explained in the next section.

2.3 Reflection High Energy Electron Diffraction (RHEED)

The thin film growth can be monitored in-situ with Reflection High Energy Electron Diffraction (RHEED). RHEED is an elegant in-situ characterization tool for the top monolayers of film growth. In other words, RHEED is a surface sensitive technique, because both the incident angle as well as the probing angle are small. Moreover, it is particularly more sensitive to surface roughness. An electron gun accelerates RHEED probing electrons to high energies in the range of 10-30 keV and hits the substrate surface at an angle of about 3 degree. After the probing electrons are diffracted by the substrate, they are projected on a fluorescent screen. The electroluminescence is imaged on a planar CCD detector, presented in figure 2.4 (top). However, the RHEED does not normally work with high oxygen pressure because of the scattering of electrons with the gas. To prevent that, the incident electron emanating from the RHEED gun are led through a tubular section that is kept at low pressure and contains a small orifice at its endpoint, very close to the substrate, where the incident electron enters the reaction chamber. To achieve that, the guidance tube is pumped down differentially to lower pressure with respect to the reaction chamber pressure and connects the RHEED gun with the chamber.

The magnitude of high energy electron wave-vector depends on its acceleration energy.

$$k_0 = \frac{1}{h} \sqrt{2m_0E + \frac{E^2}{c^2}} \quad (2.1)$$

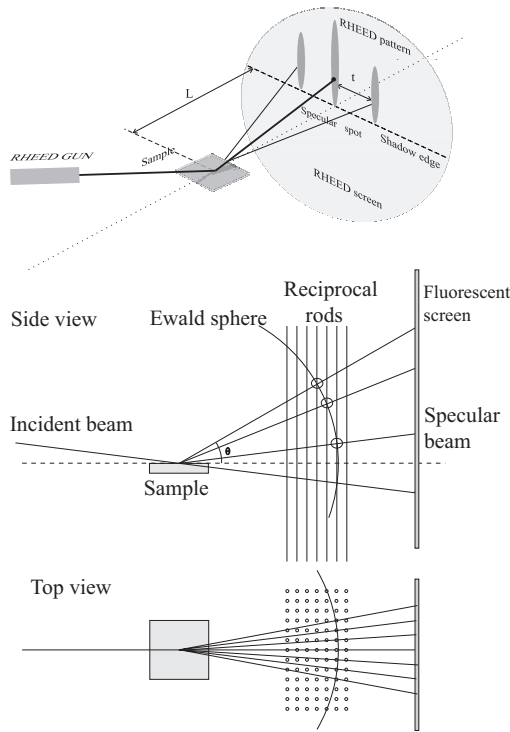


Figure 2.4: Sketch of RHEED set up in PLD chamber together with the Ewald sphere construction for the RHEED case. Top view of the circles represent the position where the Ewald sphere intersects the reciprocal lattice rods. Top view. Radius K_0 proportional to incident wavelength vector, reproduced from Szilard Csiszar PhD thesis, (2005).

Here, m_0 is the rest mass of the electron, E is the electron energy and c is the speed of light. The first term is the classical term and the second term is a relativistic correction (determine 3% of 20keV electrons)[5]. Because of the grazing incidence the component of the wave vector normal to the surfaces is very small. The mean free path into the material ranges from only 20-100 Å which makes RHEED an extremely shallow probe. The shallow probe nature of RHEED, results in the fact that the Laue condition needs to be fulfilled for only two lateral dimensions, which leads to reciprocal lattice rods/truncation rods. The Ewald sphere intersects the rods where the Laue condition is obeyed, leading to a few visible diffraction

spots. In the other words, the electrons do not see any periodic lattice in the out of plane direction, thus, the reciprocal lattice points form rods in the perpendicular direction to the sample surface. Therefore, this method mainly studies the crystal periodicity of the lateral directions along the plane. Figure 2.4 shows the real space geometry of the RHEED along with the Ewald sphere construction for determining the diffraction conditions. Moreover, RHEED also provides insight in the kinetics of layer formation.

The oscillations in specular RHEED intensity provide the most valuable information on surface roughness and step density during layer-by-layer growth, figure 2.5 a). A maximum step density corresponds to minimum RHEED intensity, which is particularly sensitive to steps. In island growth, the transmission of the electrons through the growing islands can occur. The transmission depends on both size and spacing between the grown islands. The difference between reflection and transmission can be distinguished by rotating the azimuth of the sample. The reflection spot (in layer by layer growth mode) rotates accordingly, while transmission spots (in 3D growth mode) stay, shown in figure 2.5 c). This is due to different diffraction conditions in both cases. Moreover, the growth rate and thickness can be followed during growth with RHEED oscillations. Nucleation of islands takes place shortly after the plume hits the surface decreasing the reflected electron intensity. As the islands grow and coalesce, the intensity increases. The reflectivity is maximum for a completed surface layer. The relaxation time is based on an exponential increase in intensity as soon as a new monolayer with uniform coverage is formed[6]. The RHEED specular intensity drops and then grows exponentially in time according to:

$$I(t) = I_0(1 - \exp(\frac{-t}{x})) \quad (2.2)$$

Oxygen pressure also has influence on the relaxation time as it affects the kinetic energy of the diffusing species as mentioned before. High temperatures and low oxygen pressure typically leads to enhanced diffusivity favouring step flow growth (nucleation at steps) over layer by layer growth, where individual islands laterally expand to eventually coalesce, shown in figure 2.5 b). Typical relaxation times can be obtained investigating the evolution in RHEED intensity with time. Diffuse scattering can also arise from diffusing adatoms which can lower the RHEED intensity as well.

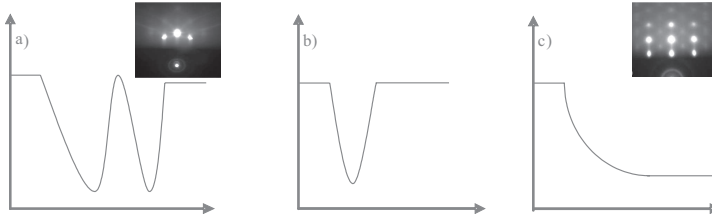


Figure 2.5: Typical RHEED oscillations of thin film growth modes by PLD technique. a) layer by layer (Frank-Van der Merwe). b) layer + island c) 3D (island) growth (Volmer-weber), adapted from C.J.M. Daumont PhD thesis, Groningen, (2005).

2.4 X-ray Diffraction (XRD)

Compared to RHEED, x-rays have a longer wavelength (shorter radius of the Ewald sphere). The interaction strength of x-rays with the electron density in the material is weaker than that of electrons and scales with the Thomson scattering length. Therefore, x-ray diffraction is well described in the kinematical approach and the description of the integrated intensities is easier as only single elastic scattering events have to be taken into account and as a consequence, a more accurate determination of lattice parameters and strain states is possible with x-ray diffraction. Inelastic (Compton) scattering is incoherent and does not contribute to interference pattern. An overview of the scattering geometry is shown in figure 2.6. The vectors of the incident wave \vec{K}_0 and the diffracted wave \vec{K} are of equal length $2\pi/\lambda$, λ being the x-ray wavelength. Their difference scattering vector \vec{Q} is described in terms of a momentum transfer, known as the scattering vector $\vec{Q} = \vec{K}_0 - \vec{K}$. The scattering plane is described by the incident beam (runs through the x-ray source) and the surface normal vector. The scattered intensity is proportional to the square of scattering amplitude $F(\vec{Q})$, which is the product of the unit cell structure factor and the lattice sum. The first summation term is the unit cell structure factor which reflects the spatial distribution of elements of electron density within the unit cell and determines the intensity of the diffraction. The second term is called the lattice sum which becomes large when the Laue condition is fulfilled, which occurs when the scattering vector \vec{Q} coincides with a reciprocal lattice vector \vec{R}_j . The product $\vec{Q} \cdot \vec{r}$ denotes the phase difference.

$$F^{crystal}(Q) = \sum_{j=1}^{Nk} f_j(Q) e^{(iQ \cdot r_j)} \sum_{R_n} e^{(iQ \cdot R_n)} \quad (2.3)$$

The observed intensity is $|F(Q)|^2$. Due to the higher penetration depth of x-rays, the single substrate peaks will become visible and are superimposed on the thin film peak structure. A thin film is a thin crystalline slab with infinite lateral dimensions and finite thickness, which gives rise to truncation rods in reciprocal space. The finite film thickness gives rise to interference between x-ray reflecting at both interfaces and causes intensity oscillation around the Bragg peaks. The periodicity of these oscillations can be used to determine the film thickness. Laue oscillations and Kiessig fringes (that will be discussed later) provide valuable information on interface quality and crystalline quality.

2.4.1 Grazing incidence

Two characteristic parameters limit the resolution of a diffractometer: the angular divergence and the wavelength spread. The former depends on the optics such as the divergence slit, the latter depends on the monochromator. At our in-house diffractometer, the $\text{CuK}\alpha$ beam is selected by the monochromator and the $\text{K}\alpha_2$ is almost completely suppressed. The angular divergence can be improved with optical elements at the expense of the loss in integrated intensity. Synchrotron beamlines are 10^{12} times more intense sources for x-ray radiation than lab diffractometers. An insertion device such as a wiggler forces oscillations of electrons to produce the x-rays. The high brilliance allows the use of more elaborate monochromators and optical elements resulting in less angular divergence. This higher resolution allows the collection of reciprocal space maps at beam lines at higher resolution. The Doris-W1 and Petra-09 beamlines at HASYLAB in Hamburg have two additional rotational axes, which allows diffraction in grazing incidence geometry[7].

Purely in-plane reflections can only be measured with grazing incidence. In grazing incidence geometry, the incident and diffracted beam do not describe a unique scattering plane. Moreover, grazing incidence diffraction is performed slightly below the critical angle for total reflection (0.1° - 0.3° for most materials) and leads to evanescent waves with limited penetration depth into the film. In grazing incidence diffraction, the

surface normal, incident and diffracted wavevector are not coplanar. This diffraction geometry is mainly used to study the in-plane crystal structure.

2.4.2 Reciprocal space maps

A reciprocal lattice map is essentially a scan around the diffraction peak structure and provides information on the lattice parameters of the film and the strain that develops when the film accommodates to the substrate. A series of coupled scans is generally transformed into a reciprocal space map. The angles ω and 2θ are directly observable angles which together with integrated intensity can be readily transformed into reciprocal space maps. The earlier described procedure can be used to bring the crystal plane in the Laue diffracting condition as a starting point for mapping.

$$\begin{aligned} Q_{\perp} &= \Delta K (\cos \delta) \\ Q_{//} &= \Delta K (\sin \delta) \\ \delta &= \frac{2\theta}{2} - \omega \end{aligned} \quad (2.4)$$

For constant wavelengths and elastic scattering $|K_0| = |K|$, the length of the scattering vector is proportional to $|Q| = 2k \sin(\theta)$. The reciprocal sphere, shown in figure 2.6 has radius $2k$. The scattering vector should coincide with a surface normal to a scattering crystal plane, which corresponds graphically to touching a reciprocal lattice point with the end points of vector tip situated on the Ewald sphere. \vec{K}_0 is stationary under all circumstances and detector and sample must be rotated to change the orientation of the scattering vector \vec{Q} . Angle dependent intensities are collected in real space and transformed into reciprocal space. The scattering plane is defined by the incident and reflected wavevectors \vec{K}_0 and \vec{K} . We distinguish the radial scan (2θ - ω) from ω scans. The 2θ - ω scan changes the length of the diffracted wavevector \vec{K} . A radial scan (offset scan) 2θ - ω scan changes length of the vector but retains the orientation (angle δ). However, ω scans change the direction of the diffracted wavevector but keep the magnitude of \vec{K} constant. A reciprocal space map is generated from a series of $(\omega + \omega_0)/2\theta$ scans series for different offset angles ω_0 . The magnitude of $\Delta\vec{K}$ is varied for each individual fixed ω line scan. The direction is changed with ω offset $\delta = \theta - \omega$. The out-of-plane lattice parameters and possible impurity phases can be derived from a specular scan with $\omega = \theta$. Any finite non-zero offset (δ) gives

diffraction peaks which also contain an in-plane component. In addition, the off-specular scan provides information on the film accommodates to the substrate lattice parameters as well as the structural symmetry of the film, whether it is monoclinic, rhombohedral, tetragonal or other symmetries. It can also be distinguished from off-specular scans that the film is fully clamped on the substrate or it is partially relaxed.

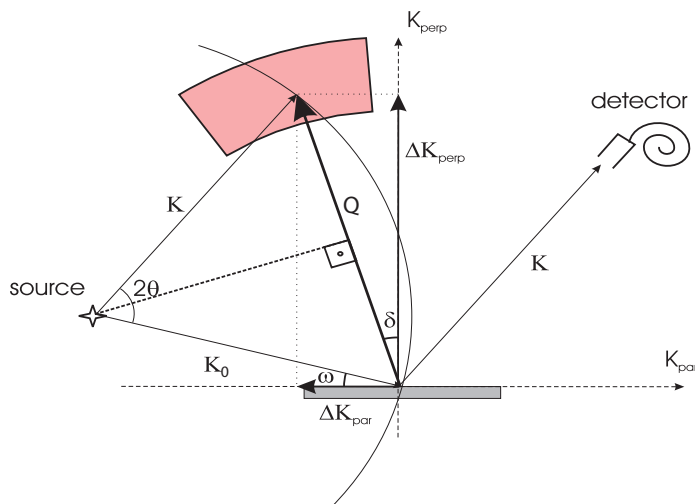


Figure 2.6: Execution of X-ray Reciprocal Space Mapping. The angles and relate directly to real space variables of the spectrometer. adapted from Szilard Csizsar PhD thesis, Groningen, (2005).

2.4.3 X-ray reflectivity

In addition to diffraction, x-ray reflectivity is based on intensity oscillations as a result of an interference effect of the different interfaces, called Kiessig fringes, which can be used both for crystalline as well as amorphous layers. A simple x-ray reflectivity measurement provides valuable information on thickness, micro roughness and electron density of the as-deposited films. A rapid decrease of reflected x-ray intensity over 5 to 6 orders of magnitude is observed at the critical angle for total reflection. Generally the reflectivity measurement is performed over a small angular range. The reflectivity can be calculated from Snell's law knowing the refractive index of the materials.

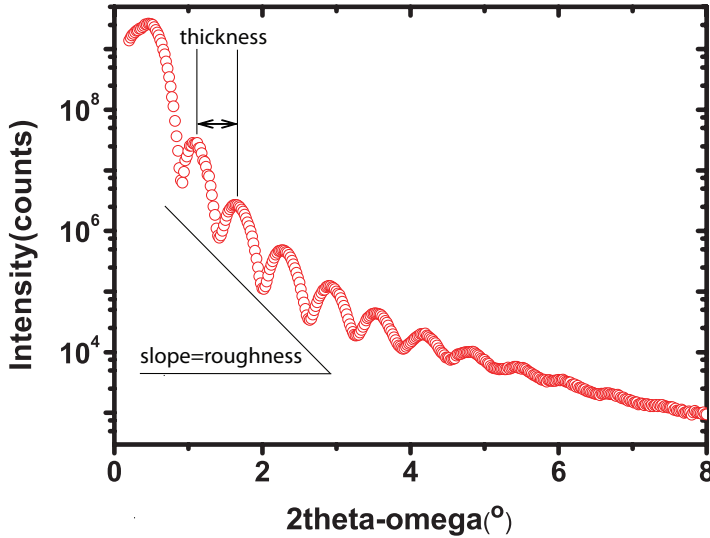


Figure 2.7: *Periodic intensity oscillations recorded in a reflectivity measurement under the critical angle of 10nm BFO thin films*

The peaks and wells in intensity as shown in figure 2.7 correspond to respectively constructive and destructive interference effects. The periodicity of the Kiessig oscillations provides information on the film thickness. The amplitude of reflectivity of the thin layer of material is described as:

$$r = -i \left(\frac{4\pi\rho r_0\Delta}{Q} \right) \left(\frac{\sin(Q\Delta/2)}{Q\Delta/2} \right) e^{iQ\Delta/2} \quad (2.5)$$

Here, ρ is the density, r_0 is the scattering length and Q is the wavevector transfer in reciprocal Angstroms. The intensity is measured at acute angles and is proportional to $|r|^2$. A plot of $|r|^2$ against the measured wavevector transfer Q shows a periodic structure of Kiessig oscillations which is fitted to equation 2.5 in order to obtain Δ which is the film thickness[8–10]. The level of reflected intensity decays with increasing incidence angle and provides information on the surface roughness of the film under study.

2.5 Atomic Force Microscopy (AFM)

Recent ongoing research in oxide electronic devices necessitates measurements with new developed techniques suitable for the nanoscale regime.

This stimulates the local study of different types of materials with various Scanning Probe Microscopy techniques. Scanning probe microscopes (SPMs) constitute an important class of experimental tools for imaging the local mechanical, atomic and electronic properties of samples at nanoscale dimensions[11]. SPMs allow the visualization of structures that would not be visible using an optical microscope. The magnification of an SPM is up to 6 orders of magnitude, while that for an optical microscope is only up to 1000-2000 times. The class of SPM technique gives rise to observation of different local physical properties depending on the way the probe interacts with the sample. Some of these techniques will be mentioned below. The invention of Scanning Tunneling Microscopy (STM) dates back to 1982 by Binnig, Rohrer, Gerber and Weibel[12]. An STM records the tunneling current between a metallic tip and a metallic surface at a given tip position by varying the applied potential. The magnitude of tunneling current depends on the distance between the sample and the tip (it should be smaller than few Angstroms). The interdependence between the polarity of applied bias and electron flow determines the direction of electron transfer between the sample and tip. This depends on the local electronic density of states at the tip/sample (the Tersoff-Hamann approach). Shortly after the invention of the STM in 1982, Binnig et al. realized that the forces between the probing tip and the sample were measurable and in this way, Atomic Force Microscopy (AFM) was developed[13]. One of the advantages of AFM is that it can also be applied on insulators. AFM, itself, provides a variety of information according to the way and strength of the interaction between the probe and the sample. This ranges from topography, electrical, magnetic properties and surface potential and field measurements, which means that depending on the modes, the dominant forces differ. They range from Van der Waals, capillary forces, chemical bonding, electrical and magnetic forces, etc. For instance, in the case of AFM in tapping mode, among various types of forces, Van der waals is the dominant force, whereas in MFM it originates from the resulting forces from magnetic dipole interactions. In turn, Piezo Force Microscopy (PFM) measures the coupling between the electric field applied to the material and the mechanical strain that it induces (in piezoelectric materials).

2.5.1 Experimental set up

AFM is equipped with a probing tip, four-quadratic photo detectors, a function generator and a lock-in amplifier. A function generator supplies

an AC voltage between the tip and the bottom electrode. The core of AFM is based on the probing technique. A probe consists of three important constituents; substrate, cantilever and the tip. The substrate is the main body of the probe and it is the means to position the probe on the tip holder to be attached to the piezo scanner of the AFM. The radius of the tip strongly determines the lower limit of the lateral resolution of the images. For obvious reasons, it is preferable to keep it as small as possible, especially in PFM studies related to ferroic domain wall investigations.

The friction between the surface of the specimen and the tip (especially in ambient working conditions) causes broadening of the radius of the tip curvature as well as decrease the life time of the coated tip (commonly used for electrical analysis). This results in lower resolution and unreliable results. In this case, special care has to be taken to account for choosing the right contact force to stay at the limit of friction action. The size of the tip is about a few tens of nanometers. The tips which are used in this work are ranging from 10 to 50 nm. It has to be mentioned that the Z direction can vary in the level of nanometers. A reliable measurement is strongly influenced by proper selection of the probe in different AFM modes. This is determined by several parameters, such as; cantilever resonance frequency and cantilever spring constant. The tip spring constant should be as small as possible for optimum vertical sensitivity. A smaller spring constant of the cantilever enhances the sensitivity (deflection is proportional to the force by Hooke's law). Moreover, soft cantilevers are preferred for topological imaging, because they allow imaging at higher frequencies decreasing the $1/f$ noise. However, for PFM a large force constant allows better contact with the surface. In this thesis, a tip with the cantilever spring constant of 5 N/m is mainly employed. The tip is made of Silicon coated either with "Cr-Co" or "Pt".

Typically, the frequency required for Vertical Piezo Force Microscopy (VPFM) analysis vary from 1-3 kHz to 2-5MHz which is limited by the bandwidth of an optical detector. However, in Lateral Piezo Force Microscopy (LPFM), the transduction of the signal from the surface to the tip requires operation in the 1-30kHz frequency regime. In this mode, though, the signal is amplified by the natural torsional motion of the tip. It has to be mentioned that investigation of the samples with a low piezoresponse, requires higher modulation frequencies like studying phenomena in resonance mode (so called DART).

2.5.2 Operating principle

The tip deflection is proportional to the force exerted by the surface. In a scan the tip is swept over surface in the lateral direction. The vertical deflection of the cantilever is optically detected by a segmented photodiode. A microfabricated cantilever connected to a pyramid shaped tip with a length of 115-135 μm and a tip radius of 10-50nm determines the lateral resolution. Photodiodes situated in quadrants are employed to distinguish the vertical or lateral distortions of the cantilever that reflects laser light. During a lateral scan along the film surface, the static deflection or the RMS oscillation amplitude is adjusted to a setpoint value. This is done by a piezo actuator that can dynamically adjust the separation between tip and sample. The contact force is simply related to the tip deflection with Hooke's law. The tip height is corrected and from these corrections the topology is imaged.

2.5.3 AFM modes

As mentioned in the introduction, an AFM can be operated in different modes: non-contact mode, contact mode and tapping mode. In the non contact mode the interaction between sample and tip is reduced to allow non destructive mapping of the surface topology. Contact mode allows additional measurement of local physical properties such as conduction. These scans can be performed rapidly at the highest possible resolution, however, the occurrence of surface damage and tip shear forces should be considered. Next, the modes which are applied in this thesis will be presented in more detail.

Tapping mode

The cantilever is driven into an oscillatory motion by a piezoelectric element (piezoactuator). The possibility to probe the surface of the sample in both air and liquid environment in combination with a variety of specimens in this mode makes it widely used in different fields. The cantilever taps on the surface of the sample close to its resonance frequency which can be obtained by tuning the tip before engaging on the surface. At the drive resonance frequency of the tip, the change in oscillation amplitude (frequency, phase change) is compensated in a feed back loop. As the piezoactuator scans along the sample surface the amplitude modulation is measured. The amplitude of the oscillation changes with respect to the

tip-film distance. It provides the highest resolution of all the scanning modes and a better accuracy at the expense of a longer scanning time. When the cantilever approaches the surface, a force is exerted between the sample and the probing tip. The interactions can be described in terms of the Lennard-Jones potential with an attractive r^6 term and a short range repulsive r^{12} term. The forces ($-d\varphi/dr$) exerted on the cantilever tip are typically in the range of nano to micro Newton.

$$\varphi(r) = 4\epsilon \left[\left(\frac{\sigma}{r_{ij}} \right)^{12} - \left(\frac{\sigma}{r_{ij}} \right)^6 \right] \quad (2.6)$$

The average separation between the tip and the surface of the sample alters the amplitude of the oscillation. The vertical movement of the scanner should stay constant with respect to the setpoint value. A laser measures the deflection of the cantilever that reflects the laser beam at the rear side, acquired by an array of photo detectors. A feed back loop ensures that the tip retains the same constant height above the surface. The corrections contain information on the surface topography. The lateral resolution is limited by the tip curvature and is typically 1-10 nm. The resolution in the vertical direction is in the range of Angstroms and is limited by thermal and electronic noise.

Additional physical properties can be superimposed on the topographical image maps of the thin films. AFM can also be extended to probe local dielectric and magnetic properties. The following sections will explain the principle of Conductive-AFM and PFM modes as surface sensitive techniques.

Contact mode

Contact mode is the typical option for PFM and conducting AFM techniques. A metallic tip is used. The tip engages the surface by extending the Z scanner. Additionally, a function generator is used to apply an AC voltage between the tip and bottom electrodes. The voltage induced cantilever deflection occurs as the result of the contact between the tip and the surface of the sample. The feedback loop adjusts the Z scanner position in a way to conserve the deflection constant with respect to the setpoint. The extension of the Z scanner stops when the cantilever deflection reaches the chosen value of the setpoint which is determined by contact force values.

2.5.4 Piezo Force Microscopy (PFM)

The Piezo Force Microscopy technique has been known as a powerful means to investigate local piezoelectricity and ferroelectricity of thin films, ceramics and single crystals at the nanoscale. Ideally, one should be able to correlate the electromechanical response to the polarization, considering the piezoelectric constant tensor[14; 15]. Note that, one of the big challenges in PFM is to distinguish the electrostatic force and the electromechanical response of the surface which both contribute to the PFM signal[8; 16]. Considering this fact, reliable quantitative measurements depend on contact forces. In the high contact force regime, the electrostatic contribution is the dominant contribution to the piezoresponse. However, in the low contact regime, that role becomes less relevant. Other aspects which need to be carefully considered for quantitative analysis of the PFM signal are related to the cantilever properties, including: mechanical properties and resonance frequency[17].

Piezo Force Microscopy in contact mode can principally be formulated as follows:

$$x_{jk} = d_{ijk}E_i \quad (2.7)$$

where x_{jk} is the strain tensor, E_i are the 3 components of the applied electric field and d_{ijk} is the 3-rank tensor that describes the piezoelectric response of a material. The tensor component measured in the direction of electric field is called longitudinal coefficient: the transverse coefficient is measured perpendicular to the field, and the others are called shear coefficients. D_{ijk} values are maximum 2000pm/V, so one should consider that the magnitude of the electromechanical response in the presence of an electric field is in the range of surface roughness of the sample and thus it is not detectable. This issue was solved by using a lock-in technique with an AC voltage, so-called "modulation voltage". In this approach, the above formula can be re-written as for the longitudinal piezoelectric response:

$$z(t) = d_{33}V_{AC} \sin(\omega t + \phi) \quad (2.8)$$

where ϕ is the polarization phase difference with the applied electric field due to the sample vibration in the presence of the modulation voltage. That means that in the out of plane mode, so-called "VPFM", the sample can be either in phase ($\phi=0$) or out of phase ($\phi=\pi$). Here, ϕ is the Piezo-response phase and $(d_{33}V_{AC})$ is the Piezo-response amplitude. Here,

the piezoelectric tensor has been re-written in the most convenient way, as a 2-rank tensor $P_i = d_{ij}X_j$, where $i=1-3$ and $j=1-6$. This uses the following convention: $X_{ij} = X_{ji}$, also $d_{ij}=d_{ijj}$ (for $j=1,2,3$) and $d_{ij}=2d_{ikl}$ (for $j=4,5,6$)[18]. Typical operation frequencies in this mode range from 1kHz to 5MHz. Moreover, a four-quadrant photo detector allows separate detection of lateral piezo-response (LPFM) as well as vertical responses. The in-plane polarization gives rise to the lateral vibration of the sample, related to the transverse coefficient. In LPFM, the transduction of the signal from the tip requires a frequency in the range of 1-30 kHz.

2.5.5 Domain imaging process by PFM

To understand both qualitative and especially quantitative measurements, one should take care about PFM contrast formation. There are three forces involved when the tip is in contact with a dielectric sample; capacitive forces due to the electrostatic force between the tip and sample, electromechanical response of the surface due to converse piezoelectric effect and a non-local electrostatic force between the cantilever and the sample. The latter is only relevant when the size of the domain is much smaller than the cantilever length, and even in this case, it can be subtracted from the PFM data. As mentioned earlier, the electromechanical force should be maximum and one of the interfering reasons is the strong electrostatic force due to interfacial layer between the surface and tip which prevents good electrical contact between the tip and sample. This layer can be easily formed when working in air because of surface contamination (water, CO_2). We have been able to improve our contact quality, and thus PFM image contrast, by chemical and thermal treatments. After the brief review on different forces that affect the PFM signal and the way to improve the signal, in principle the domains should be properly imaged as it will be further explained. In the case of a downward polarization, by applying an electric field parallel to the polarization, the sample expands. Consequently, the cantilever will be pushed up and the resultant response d_{33} should be positive which means the displacement in z direction is positive. When the sample contracts due to anti-parallel direction of the polarization with the applied field, then the cantilever will be pushed down. These possible events are typical for an out of plane polarization investigation. It should be mentioned here that the out of plane displacement causes the transversal piezoelectric responses as well, namely, d_{31} and d_{13} .

For the measurement of the in-plane polarization (LPFM), the electric

field is applied orthogonal to the polarization. The applied field produces a torsional deformation of the cantilever, thus, shear piezoelectric coefficients which are named d_{15}/d_{51} . In some materials the polarization has both out of plane and in plane components, giving rise to both vertical and torsional displacements of the cantilever. For a precise investigation of the polarization orientation, one should rotate the sample at least by 90° . Nevertheless, the real orientation of the polarization is only known when all the elements of the piezoelectric tensor are calculated[19; 20].

2.5.6 Conductive-AFM

Conductive Atomic Force Microscopy (C-AFM) provides a unique opportunity to get insight to the electrical conductivity inside the medium at local scale. This mode is derived from contact mode AFM. The C-AFM module is designed in such a way that the tip is on a virtual ground. The voltage difference is applied between the tip and sample chuck. Moreover, the extra grounding in the mentioned module has been provided to ground the cantilever holder which improves the signal-to-noise-ratio.

The current flowing through the sample is sensed by using a so-called TUNA amplifier from VEECO at constant force, kept constant by the feedback loop. The current can be detected in a range of femto-amp to micro-amp. The sample and tip are placed in series in an electrical diagram as presented in figure 2.8.

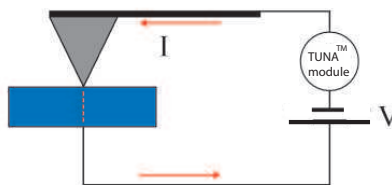


Figure 2.8: *Sketch of conduction-AFM geometry*

The two electrodes which apply the voltage bias are the sample chuck (=bottom of the sample) and the tip. Since they are designed in series, any current going from the bottom electrode of the sample, through the sample, the tip and finally the current amplifier. The latter is responsible to read the same amount of the current. The results of a simultaneous topography

and current imaging scan are combined with PFM results, which makes it possible to evaluate the conduction properties at different type of ferroelastically/ferroelectrically ordered domains and domain walls. Besides this exclusive opportunity, by varying the applied force on the sample, one can investigate the role of mechanical deformation on conduction effects. In this project the Veeco (now Bruker) Dimension V SPM has been used with the Nanoscope software package provided by the same company.

Bibliography

- [1] G. Koster et al., Appl. Phys. Lett. **73**, 2920 (1998).
- [2] B. Dam et al., J. of Appl. Phys. **73**, 3386 (1998).
- [3] Pulsed Laser Deposition of Thin Films, R.Eason(Ed.), Wiley (2007).
- [4] TSST company, www.tsst.nl.
- [5] G. Rijnders, "Solid Surfaces Interfaces and Thin Films", Springer-Verlag, Berlin Heidelberg New York, 4th edition (2001).
- [6] W. Braun, "Applied RHEED", Springer-Verlag, Berlin Heidelberg New York, (1999).
- [7] Hasyllab.desy.de/facilities/doris_iii/beamlines/e6436/index_eng.html
- [8] J.W. Hong et al., Rev. Sci. Instrum. **70**, 1735 (1999).
- [9] V. Holy, U. Pietsch, and T. Baumbach, "High-Resolution X-ray Scattering from Thin Films and Multilayers", Springer-Verlag, Berlin Heidelberg New York (1999).
- [10] J. Als-Nielsen and D. McMorrow,"Element of Modern X-Ray Physics", John Wiley and Sons (2001).
- [11] S. Kalinin and A. Gruverman, "Scanning Probe Microscopy", 1st edition (2001).
- [12] G. Binning et al., Phys. Rev. Lett. **49**, 57 (1982).
- [13] G. Binning et al., Phys. Rev. Lett. **56**, 930 (1986).
- [14] A.F. Devonshire et al., Philos. Mag. **40**, 1040 (1949).

- [15] A.F. Devonshire et al., *Philos. Mag.* **42**, 1065 (1951).
- [16] K. Franke et al., *Surf. Sci.* **415**, 178 (1998).
- [17] C. Harnagea et al., *Appl. Phys. Lett.* **83**, 338 (2003).
- [18] R.E. Newnham, "Properties of Materials: Anisotropy, Symmetry, Structure", Oxford University (2005).
- [19] C. Harnagea et al., *Integr. Ferroelectr.* **38**, 667 (2001).
- [20] S.V.Kalinin et al., *Microscopy and Microanalysis* **12**, 206 (2006).

Chapter 3

Tuning atomic and domain structure of epitaxial multiferroic BiFeO₃

3.1 Abstract

Recent works have shown that the domain walls of room-temperature multiferroic BiFeO₃ (BFO) thin films can display distinct and promising functionalities. It is thus important to understand the mechanisms underlying domain formation in these films. In this chapter, we show our characterization of both the atomic and domain structure of BFO films grown under compressive strain on (001)-SrTiO₃, as a function of thickness, by means of high-resolution x-ray diffraction and piezoforce microscopy, combined with first-principles simulations. For our films with thicknesses below 100 nm, the effect of clamping of the substrate has been observed to differ in two regimes: ultrathin, $d \leq 18$ nm, and thin, $d \geq 18$ nm. When this is taken into account in the calculations, an excellent agreement between the predicted and observed lattice parameters is obtained. We also show our determination of a twinning model that describes the experimental observations and has implications on properties of domain walls (including their conductivity), as described in later chapters. This understanding of the exact mechanism for domain formation can provide a new degree of freedom to control the structure and, thus, the properties of BiFeO₃ thin films.

This chapter has been partially published as: C.J.M. Daumont, S. Farokhipoor, A. Ferri, J.C.Wojdel, J. Iñiguez, B.J.Kooi, and B. Noheda, *Phys. Rev. B* **81**, 144115 (2010).

3.2 Introduction

Magnetoelectric multiferroics exhibit coupled electric and magnetic orders, which might lead to a variety of novel devices that would benefit from the fact that the magnetization (polarization) of these materials can be controlled by means of an electric (magnetic) field[1]. For practical devices, multi-ferroics are preferred in thin film form. Moreover, the strain induced by the mismatch between the film and the substrate lattice parameters can sometimes be used to tune the film properties with respect to the bulk[2]. Since the ground state of bulk bismuth ferrite, BiFeO₃ (BFO), is rhombohedral (space group R3c), symmetry arguments suggest that the thin films grown on cubic substrates under compressive epitaxial strain should be monoclinic (space group Cm or Cc, depending on whether the O₆ octahedra rotations are clamped by the substrate or not, respectively). Indeed, several authors[3–6] have reported a monoclinic unit cell that is similar to that of strong piezoelectric PbZr_{1-x}Ti_xO₃ with $x \approx 0.5$ [7]. The proposed link between the strong piezo-electricity and the symmetry of the unit cell[8], which allows the polarization to rotate, adds to the interest of BFO films[6]. Beyond their intrinsic properties, BFO films are currently receiving renewed attention because of the novel functionalities observed to occur at domain walls (DWs). Indeed, recent works have shown that some BFO DWs are highly conductive[9], and that the DW density controls the magnitude of the (exchange bias) coupling between BFO and other (metallic) layers in complex heterostructures[10]. It is thus of prime importance to achieve control of the domain structures and understand their formation. In contrast, it is striking to note the scarcity, and lack of agreement, of experimental information on the atomic structure of the films and its evolution with thickness[3; 5; 11]. Indeed, we believe that a complete picture of the structure of these films does not exist yet. We have grown BFO thin films on SrRuO₃ -buffered SrTiO₃ (STO) substrates (where this conducting bottom electrode is needed for the piezo-force characterization) and followed the unit-cell distortion as a function of thickness during the first stages of strain relaxation. Our c/a ratios are consistent with those in Ref.[5]. Additionally, we have been able to resolve the monoclinic distortion and measure the evolution of the full unit cell. The comparison of the experimental results with several structural models simulated ab initio allowed us to resolve the monoclinic space group (Cc) and atomic structure, as well as the polarization direction which are discussed in the next section.

3.3 Methodology

The local ferroelectric response of the films was characterized by means of piezo-force microscopy (PFM)[12], with a conducting tip and no top electrode. All the films showed ferroelectric response with the polarization vector pointing toward the substrate and all could be switched with the electric field applied between the bottom SrRuO₃ electrode and the tip. Both the in-plane and the out-of-plane piezoelectric responses have been imaged. X-ray diffraction (XRD) data and synchrotron sources analysis for mapping both out-of-plane and in-plane show that epitaxy fixes the [001] direction in reciprocal space to be perpendicular to the substrate surface. As a consequence, the number of possible monoclinic domains with polarization pointing up or down is reduced to four each and the reciprocal space maps are significantly simplified (similar to the case of a crystal under an electric field[13], but not a priori restricted to one orientation of the polarization projection, i.e. up or down). In particular, if all domains are present, looking at the areas around the substrate (hhl)_c, which corresponds to the (h0l)_m reflection in the monoclinic structure[14], one can extract the three lattice parameters and the monoclinic angle, as sketched in Fig 3.1.

Our first-principles simulations were based on the so-called "LDA+U" approach to density-functional theory, the technical details being exactly as those in Ref.[15]. We checked that our calculation conditions were well converged and reproduced basic results for BFO in the literature (as, e.g., the related ones in Ref.[16]). It has been shown that ferroelectric thin films can be successfully studied by simulating the corresponding bulk material subject to elastic boundary conditions that mimic the epitaxial constraints imposed by the substrate. In this work we extended such an approach to make a distinction between the cases of ultrathin ("uth") and thin ("th") films, for which we consider different elastic constraints. More precisely, in the "uth" case we assumed the film is strongly clamped by the substrate, and impose a tetragonal structure, i.e. $a_{pc} = b_{pc} = a_{STO}$ and $\alpha_{pc} = \beta_{pc} = \gamma_{pc} = 90^\circ$. Note that a_{STO} is the lattice parameter of the SrTiO₃ substrate, which imposes an epitaxial strain of about - 1.5% to the BFO film. In contrast, in the "th" case we only imposed that the in-plane area be constrained to be a_{STO}^2 . This allowed us to model the ultrathin-to-thin transition evidenced by the experimental results (see the discussion of Fig 3.3).

Finally, in our simulations we considered two structural models, with

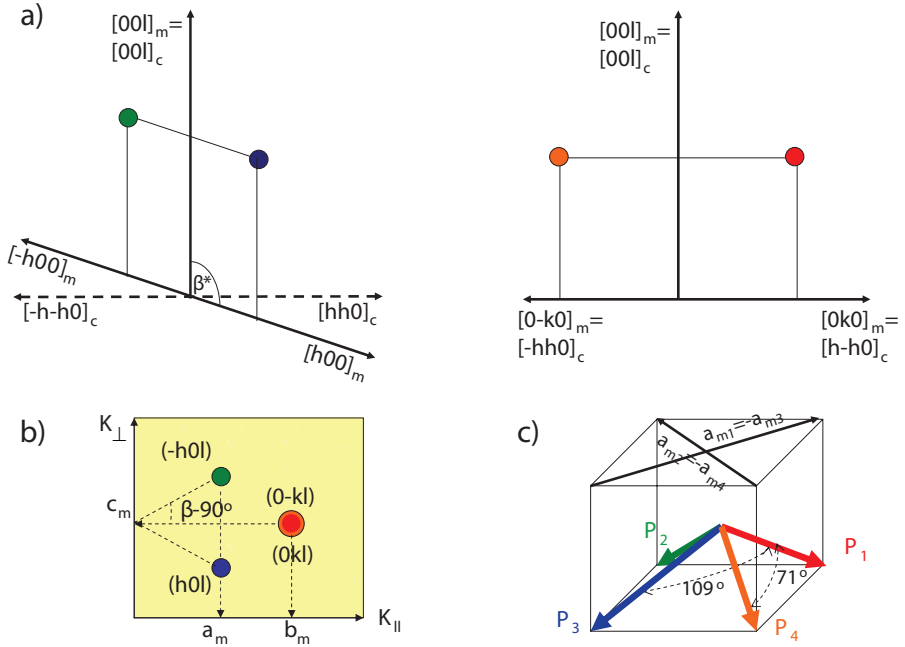


Figure 3.1: (a) Monoclinic domains in BFO thin films under compressive strain, in the $(h0l)_m$ (left) and $(0kl)_m$ (right) scattering planes. (b) Diffraction map around the $(h0l)_m$ reflections when all four domains are present. (c) Directions of the polarization and the monoclinic lattice parameter, a_m , for the four down polarized domains. In our films, the structure is M_A monoclinic with and in-plane doubled ($\sqrt{2} \times \sqrt{2}$) unit cell, and a_m and b_m are not parallel to a_{pc} and b_{pc} and the polarization direction has been calculated to be rotated 5° away from the $[111]$ toward the $[001]$ direction. (see text).

and without rotations of the O_6 octahedra, which correspond, respectively, to the Cc and Cm space groups. For clarity, a drawing of mentioned space groups is shown in Fig 3.2.

3.4 Results and discussion

Typical reciprocal space maps (RSMs) around the $(113)_c$ STO substrate reflections for selected ultrathin (≤ 18 nm) and thin (≥ 18 nm) films are shown on Fig 3.3 a).

The RSMs of the thinnest BFO films display a broad $(113)_c$ peak (using

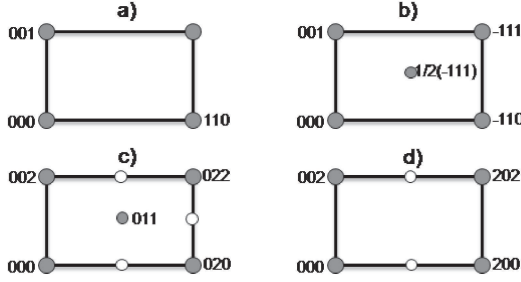


Figure 3.2: Sketch of the reciprocal lattice expected in the pseudocubic $[110]$ zone for a) the monoclinic Cm phase, b) the monoclinic Cc phase, c), and d) the monoclinic Pc phase, (here using Pc indices for clarity, adapted from Ref[17]).

the pseudocubic notation), at the same k_{par} (in-plane component of the scattering vector) of the substrate, showing that they are fully coherent with the substrate. The FWHM of these films agrees with what is expected for their thicknesses. There is thus no indication of unresolved splitting. Therefore, the films appear fully coherent and tetragonal. Only distortions of the oxygen octahedra, to which these measurements are poorly sensitive, would therefore contribute to a deviation from the tetragonal symmetry. The RSMs of thicker films display a splitting of the $(113)_{pc}$ BFO peak, as expected (see Fig 3.1). The monoclinic lattice parameters (a_m , b_m , c_m) extracted from these patterns are plotted in Fig 3.4. Interestingly, c_m shows no changes with increasing thickness. This is in agreement with the report by Kim et al.[5], who showed that the lattice parameters of the strained films are constant below 100 nm, a puzzling and up to now unexplained result. However, for thickness above 18 nm we observe a splitting of the in-plane parameter values and $\beta \neq 90^\circ$, characteristic of a monoclinic distortion. Figure 3.4 reveals a gradual increase in the monoclinic distortion a_m - b_m with thickness. Also shown in Fig 3.4 is the in-plane pseudocubic angle γ_{pc} , determined from grazing incidence XRD. In addition, grazing incidence XRD has shown that the in-plane pseudocubic angle, γ_{pc} is, indeed, different from the out-of-plane angle β , and that such a difference decreases with increasing thickness (γ_{pc} becomes closer to β in the relaxed structure). Interestingly, the deviation of a_m and b_m from the value of $2 d(110)$ (i.e., the fully coherent case) is nearly symmetric. As a consequence, the in-plane area of the cell remains essentially constant, which seems consistent with the fact that the out-of-plane lattice parameter

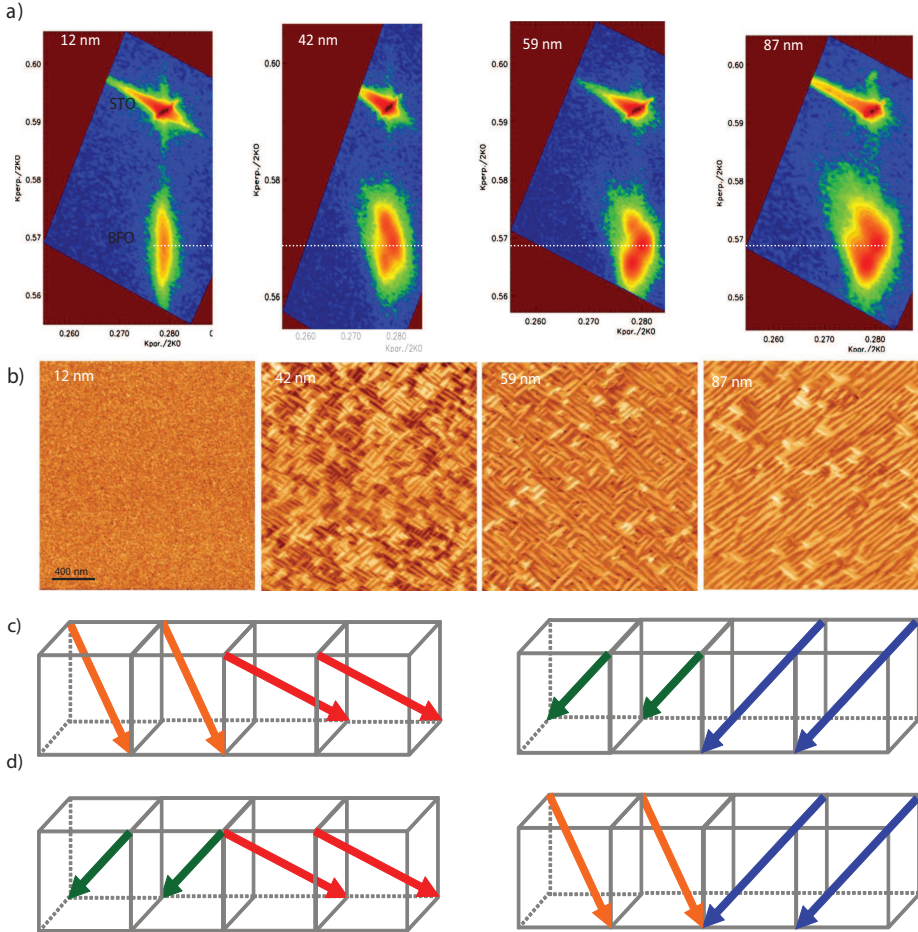


Figure 3.3: (a) Reciprocal space maps around the $(103)_m=(113)_{pc}$ reflections for different thicknesses of the BFO films. The axes are in units of $2k_0 = 4\pi / \lambda$, with $\lambda = 1.5405 \text{ \AA}$. The horizontal line through the maps indicates the out-of-plane reciprocal lattice spacing, which is unchanged in the range of studied thicknesses. (b) In-plane piezoresponse images of the same films. (c) and (d) Cartoon sketches of possible type of domain walls (head to head, tail to tail and/or head to tail domain in BFO films walls).

is unchanged. First-principles simulations allowed us to ratify these results and gain further insight into the atomic structure of the BFO films. Our results clearly indicate that the BFO films present significant O_6 rotations and thus the Cc space group. Indeed, when allowing for O_6 rotations we computed $a_m^{th}/a_m^{uth}=1.0012$ and $b_m^{th}/b_m^{uth}=0.9989$ for the splitting of in-plane lattice parameters, in reasonable agreement with the experimental values of 1.0018 and 0.9989 derived from Fig 3.4 using the data points immediately adjacent to the ultrathin-to-thin transition.

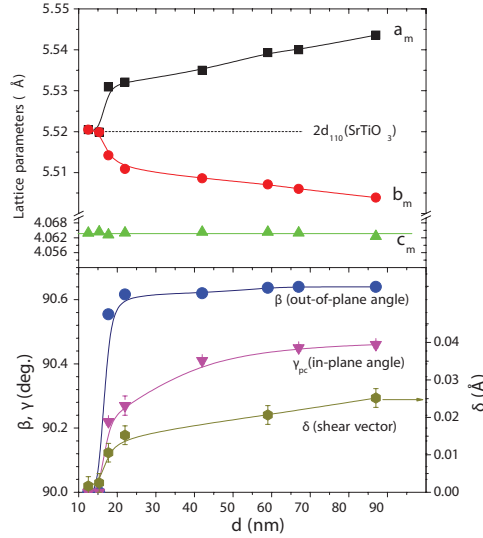


Figure 3.4: Evolution of monoclinic lattice parameters and shear displacement as a function of thickness.

In contrast, when the O_6 tiltings are clamped in the simulations, we obtained $a_m^{th}/a_m^{uth}=1.0044$ and $b_m^{th}/b_m^{uth}=0.9956$. The c_{pc}/a_{pc} ratios follow the same pattern: the value computed with (without) O_6 tiltings is about 1.03 (1.09), to be compared with the experimental result of approximately 1.04, which strongly suggests that even in the thinnest films the O_6 rotations are not fully clamped by the substrate. These results provide a justification to first-principles studies of monoclinic BFO films in which a structural model with O_6 rotations is adopted (see, e.g., Ref.[16]). Additionally, for the calculated monoclinic angle we obtained $\beta=90.1^\circ$, which seems compatible with our experimental results, and we computed $c_m^{th}/c_m^{uth}=1.00004$, in agreement with our experimental observation that the c_{pc} lattice con-

stant is weakly dependent on thickness. Finally, the computed polarization is very weakly affected by the *uth*-to-*th* transition: We obtained $P=88 \mu\text{C}/\text{cm}^2$, with in-plane and out-of-plane components of 66 and $58 \mu\text{C}/\text{cm}^2$, respectively. The polarization forms an angle of about 5.1° with the body diagonal of the pseudocubic cell, being rotated toward the [001] direction. The observed c_{pc}/a_{pc} aspect ratio of our BFO films deserves one additional comment. In the course of this study, in an attempt to investigate the relationship between the value of c_{pc}/a_{pc} and the out-of-plane polarization, we simulated the hypothetical case of a strained BFO film forced to be in a centrosymmetric (paraelectric) structure but allowing for the O_6 rotations; we obtained a c_{pc}/a_{pc} of about 1.04, a result that is similar to the one mentioned above for the polarized case and compatible with our experimental data. (Interestingly, if the O_6 rotations are also artificially suppressed, which corresponds to a fully symmetric strained film with the $P4/mmm$ space group, the computed c_{pc}/a_{pc} drops to 1.02.) Note that this lack of correlation between c_{pc}/a_{pc} and the magnitude of the polar distortion constitutes an important difference between BFO and traditional ferroelectrics such as PbTiO_3 or PZT. Indeed, our results suggest that one should avoid using crystallographic information about the (tetragonally distorted) unit cell as proof for a polar state; direct evidence for the polarization (e.g., as provided by our piezoresponse measurements) is mandatory. Let us now describe the evolution of the domain structure. Analyses of the RSMs and possible charged and uncharged domain walls (see Fig 3.3 b), c), d)) show that the domain walls that prevail in our samples are the 71° ones (see Fig 3.1 c)) which is in agreement with previous reports[18]. In the following, we provide a structural model that explains why. The predominance of 71° domain walls is confirmed by PFM imaging (Fig 3.3 b)) as well as by grazing incidence diffraction (Fig 3.5) showing similar type of domains. Out-of-plane PFM measurements show that all the films are polarized down, also in agreement with previous reports[18]. In Fig 3.3 b), in-plane PFM (IP-PFM) images of the same films are shown. In agreement with the XRD data, we observe a clear evolution of the domain pattern. For the thinnest films, no contrast is detected on the IP-PFM images. IP-PFM images for intermediate films show a clear stripelike pattern. These stripes indicate four polarization variants, which are in good agreement with rhombohedral-like monoclinic distortions[19] [see Fig 3.1 c)] and with the RSM maps. We observe that the number of variants decreases from four to two variants with further increasing thickness, allowing for longer

stripes for the thicker films. Mapping of the in-plane reciprocal space has also been performed and the main results are shown in Fig 3.5.

In Fig 3.5 a) we sketch the expected reflections around the (110), (010), and (100) reciprocal lattice points when the four domains are present. Maps around these directions are shown in Figs 3.5 c) - 5 e), respectively, for films with different thicknesses. The directions of the parallel and perpendicular components of the scattering vector in each case are shown in Fig 3.5 b). These measurements confirm the domain evolutions previously described: the 12-nm-thick films are fully coherent; for thicknesses larger than about 18 nm, four domains variants appear; finally, for the 87-nm film, we see that two of the four variants are preferred. Several works have already shown two-variant stripe domains for (001)-oriented BFO films, by using high miscut STO substrates[11; 20] or orthorhombic substrates[21]. The origin of this reduction in polarization orientations in BFO films was reported to be the step-flow growth and the substrate anisotropy, respectively. In our case at least during the first 4 monolayer, all the sample grow layer by layer and the substrate miscut angle in all our films is the same, thus, our results point to yet a different mechanism. All this evidence fits a simple but powerful model by which the domain formation enables and controls the monoclinic distortion of the unit cell. Figure 3.6 a) shows how twinning reduces the in-plane strain introduced by the pseudocubic angle, γ_{pc} (characteristic of the monoclinic distortion). Two pairs of twins, coherent along [100] or along [010], can form. It can also be seen that, in order to do that, the in-plane lattice parameters of the film, a_f and b_f , deviate in different direction, nearly symmetrically, from the fully strained values of $a_{str} = b_{str} = \sqrt{2} a_{STO}$, i.e., $\vec{a}_f = a_{str} \vec{e}_1 - \vec{\delta}$ and $\vec{b}_f = b_{str} \vec{e}_2 - \vec{\delta}$, as sketched in Fig 3.6 b).

The magnitude of the shear vector δ , therefore, determines both a_f and b_f , which change in different direction (increasing and decreasing, respectively) with increasing thickness as long as γ is close to 90° , excellently explaining our experimental observations (see Fig 3.4). In this model, the in-plane area of the film is unchanged with respect to the fully coherent film, which in turn seems compatible with the observation that the cm lattice parameter does not vary during strain relaxation (for thicknesses up to 100 nm). A more subtle result of this relaxation process is that the symmetry of the film unit cell is actually lower than monoclinic, it is actually triclinic; indeed, it can be seen from Fig 3.6 b) that the angle between a_f and b_f is given by $\gamma_f = \cos^{-1}(\delta/a_f b_f)$, and thus different from 90° . A

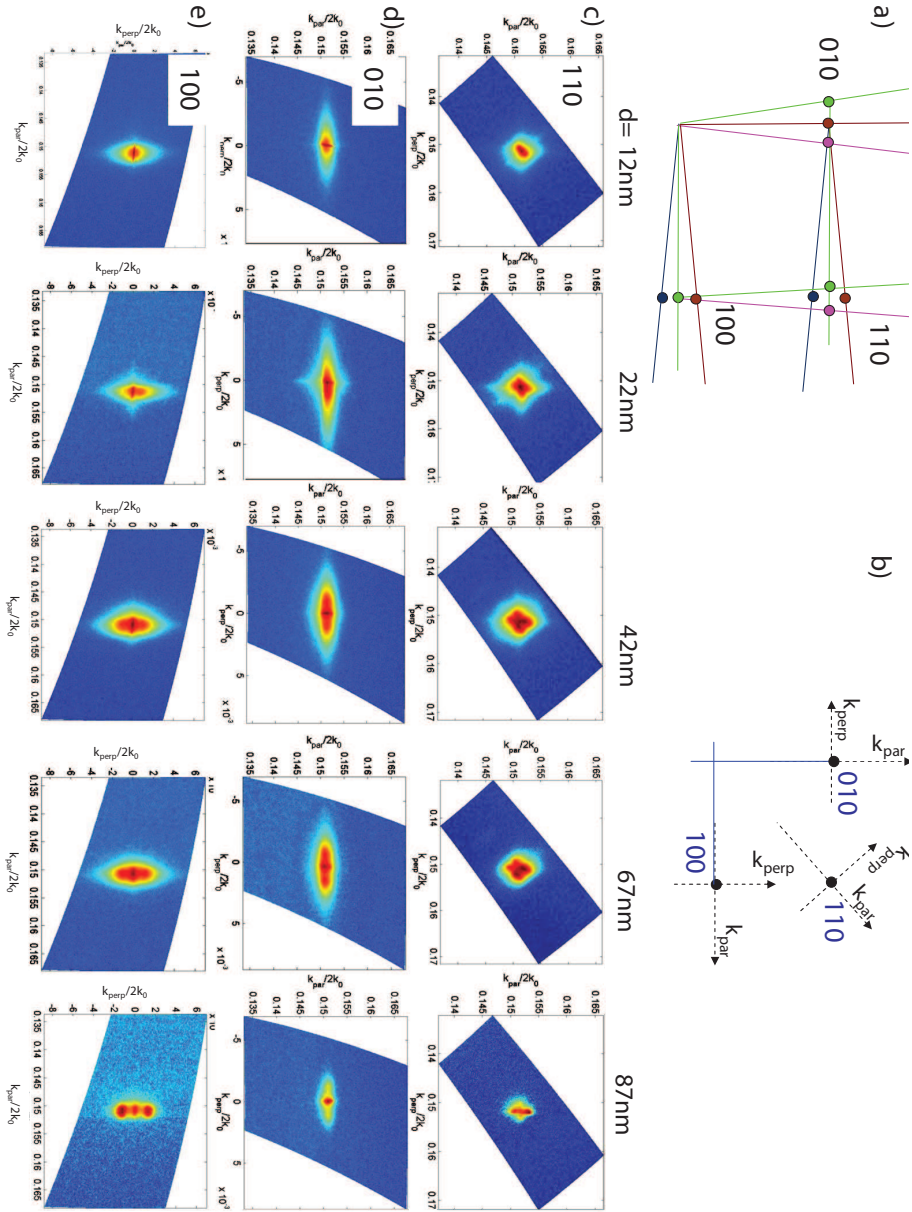


Figure 3.5: (a) Sketch of the RSM's expected around the (100), (010), and (110) pseudocubic reflections when all four domains are present; (b) directions of k_{par} and k_{perp} in each case; [(c)-(e)] maps around (110), (010), and (100), respectively, for different film's thicknesses. The axes are in units of $2k_0$, where $k_0 = 2\pi/\lambda$.

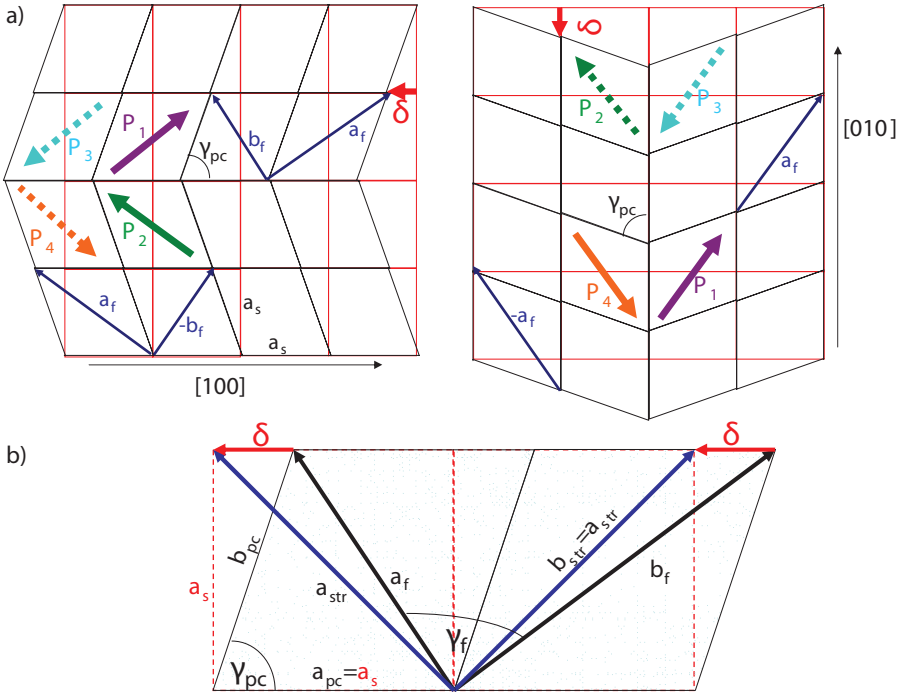


Figure 3.6: (a) The two types of twins present in the films, each including 71° walls: (left) is coherent along $[100]$ and (right) is coherent along $[010]$. (b) Detail of the film distortion.

very similar twinning mechanism with symmetry lowering has been found in thin films of TbMnO_3 grown on (001)-STO substrates[22], which suggests it may be typical of low-symmetry perovskites on cubic substrates. As observed in Fig 3.6 a), the two pairs of variants, 90° rotated from each other, are in agreement with the PFM maps of the 42- and 59-nm films and give rise to both 71° and 109° walls. Even though both nucleate with equal probability in the growing film, on a low-miscut substrate, because of the relatively large-strain energy store at the boundary between them, for thicker films (and therefore larger strain energy at those boundaries) one of the two variants will be preferred, as observed in the thicker 87-nm film, and mostly 71° walls remain. In the presence of a substrate miscut, the steps can indeed determine which of the two variants is present[11] but this will also happen in exact substrates provided that the films have enough time to relax. These 71° walls can be atomically perfect and defect-free

(see Fig 3.6). This is of importance to our discussion of domain wall conductivity in subsequent chapters. It is worth mentioning that the domain orientations observed here, after slow PLD growth, have rarely been reported so far[3] and that, typically, more complex reciprocal space maps than those in Fig 3.3 are observed around the $(h0l)_m$ reflections[4; 11; 23]. The reason for that is that most of the films reported contain domains that have crystal orientations with out of plane tilts and, thus, do not share the pseudocubic [001] direction with the substrate.[23] However, the lack of a coherent interface can, in some cases, be advantageous since these films are less clamped and could better allow polarization rotation[6] or a lower leakage characteristic[23; 24]. These differences are determined not only by the substrate miscut but also by the growth conditions. Here we show that it is possible to control not only the structure and the type of domains but also their orientation relative to the substrate, which is of crucial importance to understand the ferroelectric properties of the films.

3.5 Conclusion

We have observed clear trends in the evolution with thickness of the structure and microstructure of BiFeO₃ films on (001)-SrTiO₃ substrates. We have shown that the lattice parameters and the film symmetry do not result simply from the mismatch with the substrate but also from the occurrence of a particular twinning that allows for the observed monoclinic distortion. Such an effect provides us with a new degree of freedom for tuning the structural and physical properties of the thin films. This twinning model explains why the 71° domain walls are so often observed in atomically flat films on (001)-SrTiO₃, also confirmed by TEM studies (section 3.6). Our results suggest that the physics behind the effects of epitaxial strain is richer than usually thought, and that traditional thermodynamic phase diagrams and first-principles models need to be complemented with knowledge of the domain structure in order to reach a full understanding of the behavior of the materials.

3.6 Experimental

Several (001)-oriented BFO thin films with thickness ranging from 12 to 87 nm were grown on atomically flat, TiO₂-terminated (001)-STO substrates with low miscut angle (0.1°). Conductive layers of SrRuO₃ with

a thickness of 5nm were deposited in between the substrate and the BFO layer. The BFO films were grown by pulsed laser deposition (PLD), assisted by reflective high-energy electron diffraction, using a pulsed KrF excimer laser ($\lambda=248$ nm) with a repetition rate of 0.5 Hz. The deposition was performed at 670 °C in an oxygen pressure of 0.3 mbar. After deposition, the films were cooled down slowly to room temperature under an oxygen pressure of 100 mbar. The local ferroelectric response of the films was characterized by means of piezo-force microscopy (PFM)[12], using a Dimension V (VEECO) microscope with conducting tip and no top electrode. The evolution of the crystallographic distortion with thickness was investigated by mapping the reciprocal space using x-ray diffraction (XRD) from laboratory sources, for mapping out-of-plane scattering planes, and synchrotron sources (W1 beamline at HASYLAB-DESY) for scattering in the plane of the film.

In addition, BFO thin films were prepared for Transmission Electron Microscopy (TEM), following a method introduced by Strecker et al.,[25]. The thin film samples were supplied as plates, with sides of 5 mm and a thickness of 1 mm. On one side, 0.5 mm were removed using a diamond wire saw (Well Precision Vertical Diamond Saw 3242), resulting in a square of 5 mm x 4.5 mm. It was then sawed in half in the same direction as before so that two pieces of 2.25 mm x 5 mm were gained. These were then glued together with the epoxy Gatan G1 in a way that the sides on which the thin film was deposited face each other. The resulting sandwich-like structure was inserted into a brass tube with a length of 6.6 mm, an outer diameter of 3 mm and an inner diameter of 2.4 mm and filled with Gatan G1. From this tube, slices with a thickness of roughly 220 μm were cut. They were then grinded with a Gatan Disc Grinder 623 using grinding paper with grains of 40 μm and 15 μm from both sides to a thickness of roughly 70 μm . To avoid shear forces at the interface region, the sample was grinded only along a direction parallel to the interface between the two slices. To further reduce the thickness of the slice, a Gatan Dimple Grinder 656 was used. In combination with a diamond grinding compound with a particle size of 3 μm , the thickness at the middle of the sample was thinned to roughly 30 μm using a grinding wheel. The surface was smoothed with a felt wheel assembled to the dimpler and a diamond grinding compound with a particle size of 0.25 μm . Only one of the two sides was treated in this way. For the final thinning step, a Precision Ion Polishing System (PIPS) by Gatan was used where the sample is thinned from both sides

with an argon ion beam. The energy of the argon ions was 4 keV and the beam was inclined at an angle of 5° to 7°. Finally, the surface was cleaned by low energy ion milling for 10 min each at 0.9 keV, 0.6 keV and 0.3 keV. Prior to insertion of the sample into the TEM, the sample was plasma cleaned for 4 min. Image of one of the samples (20nm BFO on 5nm SRO on STO) studied by TEM is shown in Figure 3.7. All films show an epitaxial orientation relationship as will be discussed later and fairly abrupt interfaces without massive reaction phases.

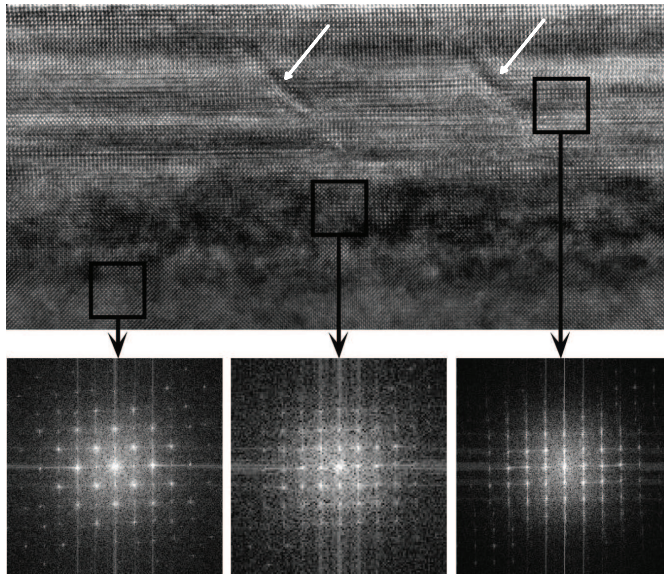


Figure 3.7: HRTEM image of the 20 nm BFO / 5 nm SRO / STO sample. The areas where the Fast Fourier Transformations (FFTs) are calculated are marked by squares. The FFT show that the viewing direction of the HRTEM image is [100], moreover, a 71° DW (defect line) is indicated by an arrow (adopted from master thesis of A. Müller, Für die Masterprüfung in Chemie an der Ludwig-Maximilians-Universität München).

As shown in the figure 3.7, the orientation relationship is (001) STO || (001) SRO || (001) BFO and [100] STO || [100] SRO || [001] BFO. These findings completely correspond to already published results where a cube on cube relationship is reported[2]. Additionally, in the same sample, defects could be observed in HRTEM image, which are known as 71° domain walls, shown with white arrows[26].

Bibliography

- [1] R. Ramesh and N. A. Spaldin, *Nature Mater.* **6**, 21 (2007).
- [2] J. Wang et al., *Science* **299**, 1719 (2003).
- [3] G. Xu et al., *Appl. Phys. Lett.* **86**, 182905 (2005).
- [4] H. Bea et al., *Philos. Mag. Lett.* **87**, 165 (2007).
- [5] D.H. Kim et al., *Appl. Phys. Lett.* **92**, 012911 (2008).
- [6] H.W. Jang et al., *Phys. Rev. Lett.* **101**, 107602 (2008).
- [7] B. Noheda et al., *Appl. Phys. Lett.* **74**, 2059 (1999).
- [8] L. Bellaiche et al., *Phys. Rev. Lett.* **84**, 5427 (2000).
- [9] J. Seidel et al., *Nature Mater.* **8**, 229 (2009).
- [10] L.W. Martin et al., *Nano Lett.* **8**, 2050 (2008).
- [11] H.W. Jang et al., *Adv. Mater.* **21**, 817 (2009).
- [12] M. Alexe and A. Gruverman, "Nanoscale Characterization of Ferroelectric Materials", Springer-Verlag, Berlin (2004).
- [13] B. Noheda et al., *Phys. Rev. Lett.* **86**, 3891 (2001).
- [14] The indexes are with respect to the C_m space group, as in Ref. 14. With XRD we are not sensitive to oxygen rotations as thus we cannot distinguish between C_c and C_m .
- [15] O.E. Gonzalez-Vzquez and J.iguez, *Phys. Rev. B* **79**, 064102 (2009).
- [16] A.J. Hatt et al., *Phys. Rev. B* **81**, 054109 (2010).

- [17] B. Noheda et al., *Phys. Rev. B* **66**, 060103 (2002).
- [18] Y.H. Chu et al., *Appl. Phys. Lett.* **90**, 252906 (2007).
- [19] F. Zavaliche et al., *Phase Transitions* **79**, 991 (2006).
- [20] R.R. Das et al., *Appl. Phys. Lett.* **88**, 242904 (2006).
- [21] Y.H. Chu et al., *Adv. Mater.* **18**, 2307 (2006).
- [22] S. Venkatesan et al., *Phys. Rev. B* **80**, 214111 (2009) and C.J.M. Daumont et al., *J. Phys.: Condens. Matter.* **21**, 182001 (2009).
- [23] H. Liu et al., *Appl. Phys. Lett.* **96**, 012901 (2010).
- [24] L. Pintilie et al., *Appl. Phys. Lett.* **94**, 232902 (2009).
- [25] A. Strecker et al., *Praktische Metallographie* **30**, 482 (1993).
- [26] Y.B. Chen et al., *Appl. Phys. Lett.* **90**, 072907 (2007).

Chapter 4

Conduction through domain walls in BiFeO_3 thin films

4.1 Abstract

In the previous chapter, we have reported that BiFeO_3 thin films epitaxially grown on SrRuO_3 -buffered (001)-oriented SrTiO_3 substrates show orthogonal bundles of twin domains, each of which contains parallel and periodic 71° domain walls. A smaller amount of 109° domain walls are also present at the boundaries between two adjacent bundles. In this chapter, we report enhanced conduction at all as-grown twin walls - both 109° and 71° domain walls. Conduction at domains and domains walls is investigated as a function of bias, temperature. In the next chapter, we will discuss the conduction mechanisms as well as the tunability of the conduction magnitude.

This chapter has been partially published as: S. Farokhipoor and B. Noheda, *Phys. Rev. Lett* **107**, 127601 (2011) and S. Farokhipoor, B. Noheda, *J. Appl. Phys.* **112**, 5 (2012).

4.2 Introduction

Ferroelastic, or twin walls, in ferroic materials provide highly localized regions of large strain gradients and local symmetry breaking in such materials, with the potential to display distinct additional physical responses than those of the host materials. Moreover, because of the intense strain gradients, they can attract large concentrations of dopants or defects, which will also modify greatly and very locally the materials' properties[1]. Ekhard K. H. Salje, a pioneer in research on twin walls, has recently gathered the most prominent examples in the past couple of decades, when twin walls in oxides have been reported to show distinct functional properties, including electrical polarization in non-polar CaTiO₃ or superconductivity in insulating WO₃ [2]. In addition, with the renewed interest in multiferroic materials, the enhanced coupling of these two order parameters and the distinct magnetoelectric response at domain walls of multiferroic oxides have been subject of much recent attention[3–6]. Twin domain walls in antiferromagnetic TbMnO₃ have been proposed as the origin of a net magnetic moment in TbMnO₃ thin films[7], while the net magnetic moment in twin domain walls in antiferromagnetic BiFeO₃ is believed to cause the observed exchange bias in a BiFeO₃-permalloy bilayer[8]. Even if tantalizing results on twin walls have been known and twin walls had been accessed and imaged[9; 10], it has only recently become clear that, using thin film deposition techniques, reproducible control and tunability of the type, orientation and periodicity of domain walls, separated by distances of only tens to hundreds of nanometers, are possible.

Recently, the potential of domain walls has reached a new milestone, with the observation of conductivity at certain types of ferroelectric / ferroelastic domain walls in insulating multiferroic BiFeO₃ [11; 12] thin films. Although conductivity at domain walls has been postulated in the past (see Ref.[13]and references therein) it is only recently that measuring it has become possible. Thus, also due to the widespread use of local probes, it is now realistic to think of using the domain walls and their unique properties as devices[14; 15]. But what has boosted the general interest on domain walls is the recent discovery that domain walls of multiferroic (ferroelectric and antiferromagnet) BiFeO₃ thin films are considerably more conducting than the domains and, thus, provide well-defined, local paths of conduction through the thin films[11].

BiFeO₃ thin films are monoclinic[16] however, in fact, they are quasi-rhombohedrally distorted and, thus, the ferroelastic domain walls that they

present are very similar to those expected in a rhombohedral perovskite, that is 71° and 109° domain walls[17]. Initially, conducting behavior was observed only in artificially-written 109° domain walls[11]. However, it was later reported that also as-grown 71° walls displayed enhanced conductivity with respect to the domains[18], although that was one order of magnitude smaller than the conductivity found in as-grown 109° domain walls. This seems to be in agreement with the theoretical calculations that assign the origin of conduction to a decrease in the band gap of the material at the domain walls[11; 18], due to the different atomic arrangement at the wall. Because domain walls in ferroelastic epitaxial thin films can be now controlled to a great extent[19; 20], this discovery opens the door to novel nanometer-sized devices, as long as we are able to engineer and control the conduction paths in these materials.

4.3 Results and discussions

As described in the previous chapter (see also ref.[21]), the as-grown samples are monoclinic (pseudo-rhombohedral), actually, the samples with twins even have lower symmetry and they are triclinic (see chapter 3, section 3.4). From the eight possible twins[17], only the four variants pointing towards the SrRuO_3 electrode are present in the films, in agreement with other reports[19]. Due to the interdependence between conduction mechanisms and the domain configurations, a specific thickness range is investigated. For this study, the thickness of the thin layer is ranging from 48nm to 72nm for which orthogonal bundles of parallel domains can be easily obtained. Most of the domain walls (DWs) are 71° DWs (where 71° is the approximate angular difference between the polarization vectors at both sides of the wall). In between two perpendicular sets of 71° DWs, some 109° DWs can also be found[21]. These ferroelectric/ferroelastic domains can be imaged by in-plane piezo-force microscopy (IP-PFM), using a metallic tip (Co-Cr coated Si in our case) of an AFM microscope. In Figure 4.1 a) and b) the sample position and its polarization state (the color code is the same as that in Figure 3.1) has been shown. In Figure 4.1 c) and d), different polarization directions are shown in both phase and amplitude images, which allows to extract the types of domain walls and their neutrality. Figure 4.1 e) shows the enhanced conduction at localized area of both 71° and 109° domain walls. Figure 4.1 f) shows the difference in the magnitude of the current within a domain and at the wall.

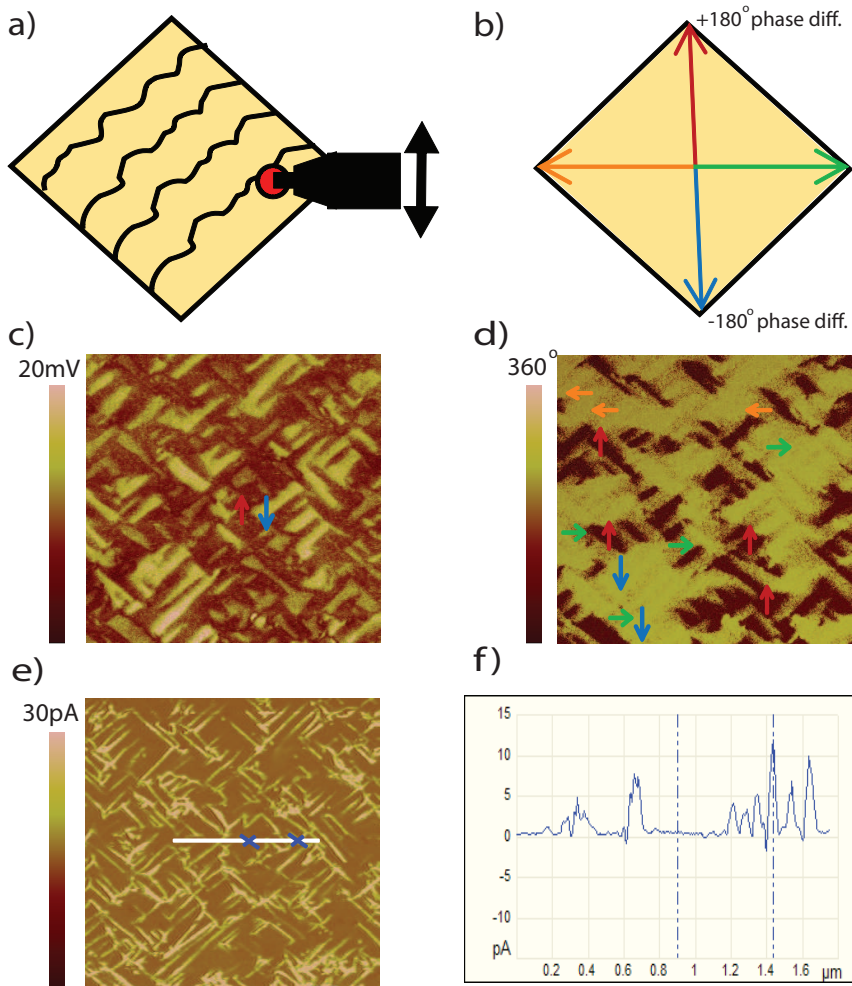


Figure 4.1: a) The position of sample and tip respect to each other while scanning is performed, b) plane-view polarization state from figure 3.1. showing different polar vectors, c) and d) present in-plane piezo-force microscopy images of both amplitude (c) and phase (d) needed to determine the type of domain walls and their neutrality (the same polarization color code has been used), e) Conducting AFM image taken simultaneously in the same area and with a bias voltage applied to the sample of 2.75V (in the low current regime). f) Line scan across several domains and domain walls showing the difference in the current level (the corresponding line is shown in fig 1 e). Size of the images is $3\mu\text{m} \times 3\mu\text{m}$.

Chiu et al.,[22] also observed enhanced conduction at 71° DWs, using scanning tunneling microscopy, while our conduction maps has been locally measured and mapped using a TUNATM amplifier, which is designed to measure leakage currents, (for more details, see section 5). In our films, unlike in those of ref.[22], the magnitude of the current in the 71° walls is as large as that of the 109° walls. This difference between the two studies could be due to the nature of the interfaces (out-of-plane twinning versus in-plane twinning)[23; 24], or the role of oxygen vacancies which will be further discussed. Moreover, the 71° domain walls in our investigated films showed a somewhat more (statistically) consistent behavior than that of the 109° walls, probably due to the fact that the latter are located at the edges of the orthogonal bundled regions, where the strain is enhanced, possibly inducing dislocations or other defects.

To complete our studies on the chosen series of the thicknesses, similar data is shown for 72nm thick film in figure 4.2. One such map is reproduced in figure 4.2 c) and, when compared to the IP-PFM images, it reveals that the 71° (as well as the 109° domain walls) in these films are conducting at room temperature, while the domains are not conducting at this temperature. Figure 4.2 d) shows both the in-plane piezoelectric response and the current when scanning across a 71° domain wall, showing the maximum conductivity in the middle of the wall (characterized by the minimum piezoelectric response).

This is different from what is observed in other BiFeO₃ samples grown on different, substrates, DyScO₃, at higher deposition rates and with higher oxygen pressure by Seidel et al.[11]. There, conduction was found only at 109° DWs. The observation of conduction at the 71° domain wall is particularly important because these walls are more stable and can be more easily moved with an electric field[17; 25], and because our current understanding (see previous chapter) suggests that these domain walls can be formed without the creation of structural defects.

Figure 4.3 displays I-V curves for the 71° DWs, 109° DWs and off-wall at room temperature in linear scale, showing the rectifying diode behavior of the domain walls, as previously reported for the 109° walls[11]. BiFeO₃ containing oxygen vacancies can be considered as an n-type semiconductor. The forward diode direction coincides with that of the electrical polarization and it indicates that carriers are electrons injected from the (grounded) top electrode (AFM tip)[26; 27]. No apparent difference exists, at this temperature, between the two types of walls. In order to

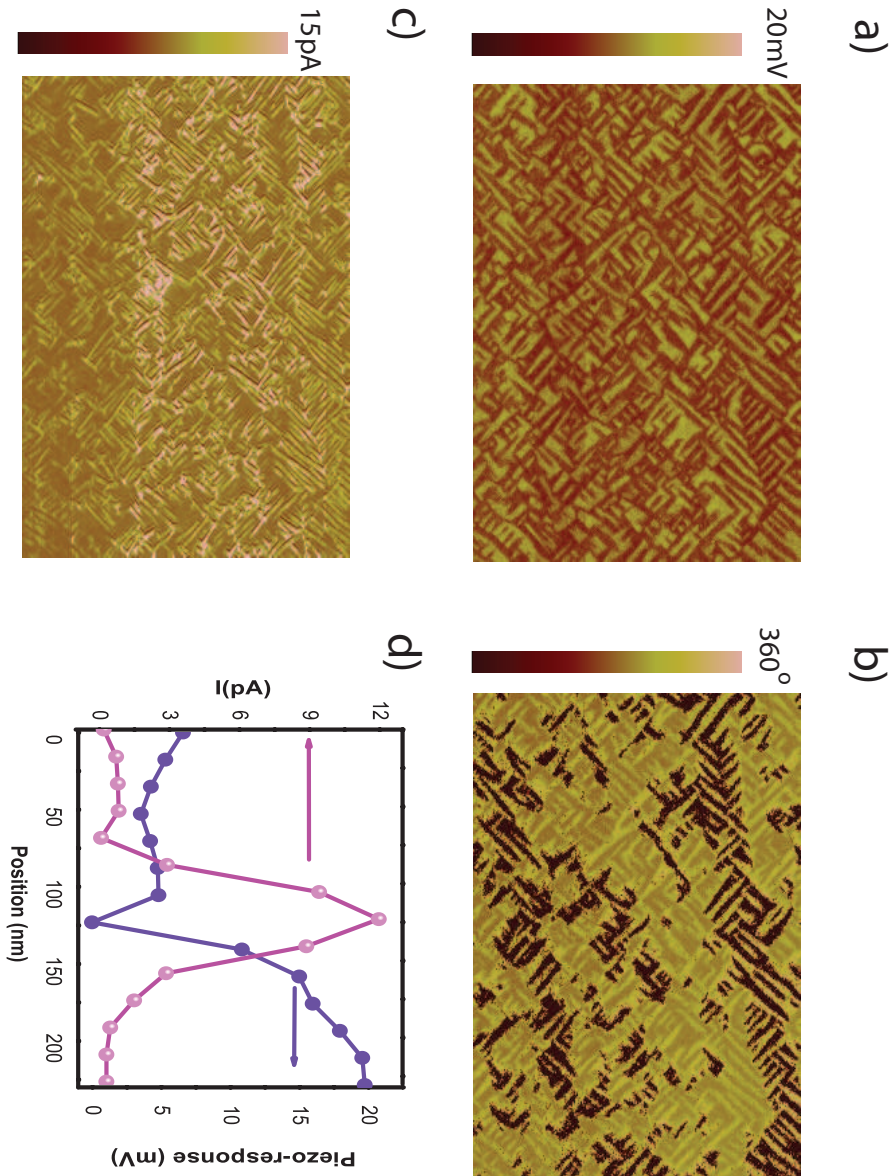


Figure 4.2: In-plane piezo-force microscopy images of a $4\mu\text{m} \times 4\mu\text{m}$ area. Amplitude (a) and phase (b) images. c) Conductive-AFM image of the same area of the film showing enhanced currents at the domain walls. Both 71° and 109° domain walls show similar magnitudes of the current. The image is taken simultaneously to a) and b), with a bias voltage applied to the bottom electrode of $+2.4\text{V}$. d) Line scan across one domain wall in both the piezoresponse amplitude (a) and the current (c) images.

gain control on the currents, it is important to understand the conduction mechanisms (this will be extensively discussed in chapter 5). For that we have measured the I-V curves at different temperatures (from 20 °C to 200 °C, in air). These curves are plotted in two different style (linear and logarithmic) in Figures 4.4 a) - f) for the 71° DWs, the 109° DWs, and off-wall, respectively. About 100 walls were investigated and all showed similar behavior.

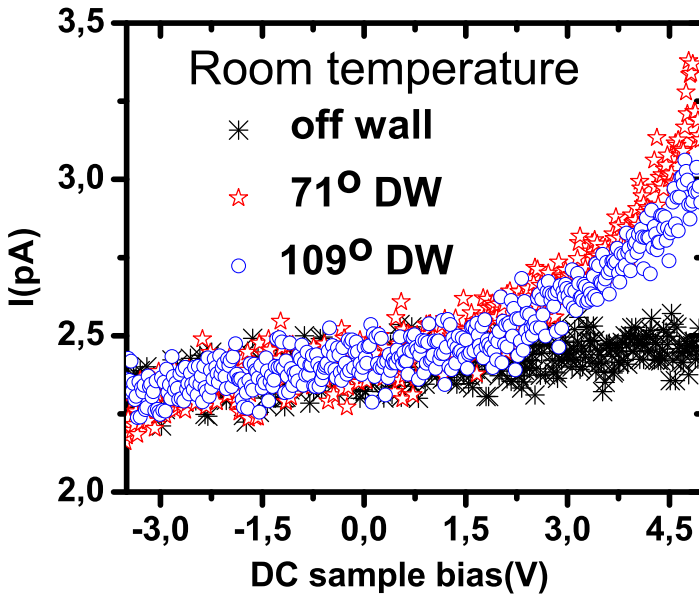


Figure 4.3: *I-V curves at room temperature for 71° DWs, 109° DWs and off-wall.*

We have looked for signatures of interface-limited conduction, such as Fowler-Nordheim tunneling ($\ln(I/V^2) \propto E^{-1}$) or Richardson-Schottky-Simmons emission ($\ln I/(T^{3/2}V) \propto V^{1/2}$)[28], as well as of bulk-limited Poole-Frenkel emission ($\ln(I/V) \propto V^{1/2}$). The possibility of current-limitation due to built-in space charge ($I \propto V^2$) is also investigated, as discussed in the next chapter. Interestingly, qualitatively similar behavior has been found for the three conduction paths (109°, 71° and off-wall), while the current level is quantitatively (one order of magnitude) lower in the case of

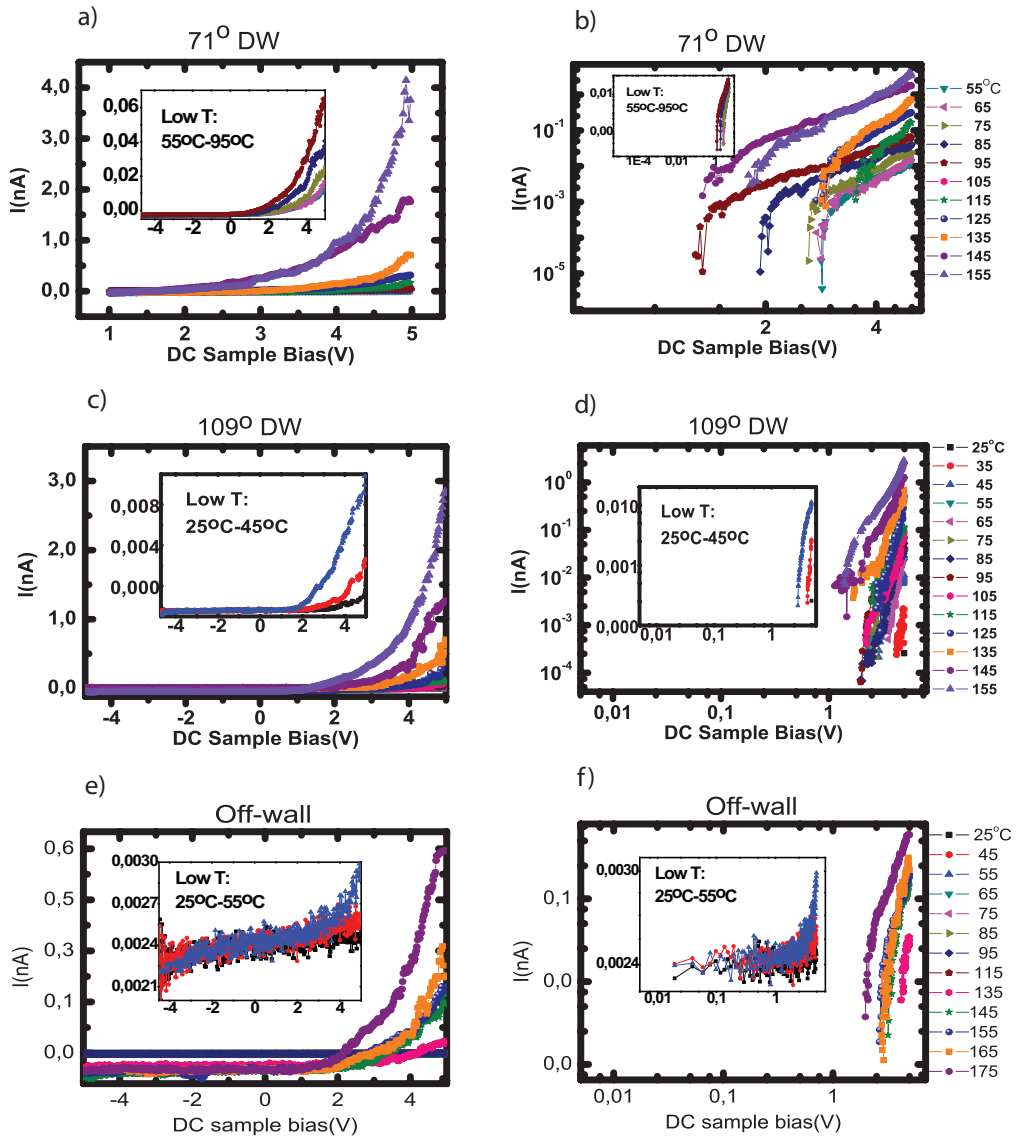


Figure 4.4: linear a), c), e) and logarithmic b), d), f) I-V curves at different temperatures at 71° DW, 109° DW and off-wall, respectively. The lower temperature curves are plotted separately in the insets.

domains compare to those at two different walls for the same temperature and voltage range.

4.4 Conclusion

To conclude, we report that both 71° and 109° , naturally-formed, ferroelastic domain walls of BiFeO_3 grown on SrRuO_3 -buffered SrTiO_3 provide well-defined conducting paths through the films, from the metallic tip acting as top electrode to the bottom SrRuO_3 electrode. Conduction is provided by n-type carriers and the qualitative behavior of conduction is similar for both type of domain walls and domains. However, the conduction level is one order of magnitude smaller in domains compare to those of in both 71° and 109° walls. In the next chapter, we will investigate the conduction mechanisms and we will show that it enhances our ability to control the current level. Moreover, the role of defects and their interplay with polarization will be further studied.

4.5 Experimental

Thin films of (001)-oriented BiFeO_3 films with thicknesses ranging between 40-70 nm have been slowly grown on SrRuO_3 -buffered SrTiO_3 substrates by pulsed laser deposition (PLD) assisted by RHEED using a system designed by Twente Solid State Technology (TSST)[29] provided with an excimer laser (Lambda Physik COMPex Pro 205) filled with KrF to produce a wavelength of 248 nm. The operating laser frequency and fluence were 0.5Hz and 2 J/cm^2 , respectively. The chamber was evacuated up to a background pressure of 10^{-8} mbar. The films were grown at a temperature of 670°C in an oxygen pressure of 10^{-1} mbar. After growth, the oxygen pressure was increased to 100mbar and the films were cooled down at a rate of 3° C/min . The films are grown on single-terminated $(\text{TiO}_2)(001)$ -oriented SrTiO_3 substrates[30]. The 5nm thick SrRuO_3 layer was deposited also by PLD immediately before the BiFeO_3 deposition, with a substrate temperature of 600°C , an oxygen pressure of 0.13 mbar and laser frequency and fluence of 1 Hz and 2J/cm^2 , respectively (see also ref.[21]). These films show atomically flat terraces (see Figure 4.5 a) - b), flat interfaces and good crystal quality (Figure 4.5 c)). They form monoclinic, pseudo-rhombohedral, domains with the polarization very close to the pseudo-cubic $[111]_p$ direction. From the eight possible polarization ori-

entations, only the four down oriented domains are present in these films, in agreement with other reports[31; 32], and thus no 180° domain walls are present. The observed domains are organized in bundles[33] of parallel 71° domain walls[7]. Adjacent bundles are oriented orthogonal to each other and at the boundaries in between bundles some 109° domain walls are also found. From the reciprocal space maps around non-specular reflections (inset of Figure 4.1 c) and ref.[7]), it can be inferred that the (001) atomic planes of the film are parallel to those of the substrate and buffer layer and, thus, that there is no out-of-plane tilt or buckled interface, as reported for some (001)-oriented rhombohedral perovskites[23; 31; 34]. This is important because the nature of the interfaces will largely influence the conduction properties of the films[24].

The domains have been imaged by in-plane piezo-force microscopy (IP-PFM), using the metallic tip (Co-Cr coated Si) of an AFM microscope. The conduction through the sample, from the electrically grounded tip to the bottom SrRuO₃ electrode (held at variable bias voltages), can be locally measured and mapped using a TUNATM amplifier (Bruker Corp.), which is designed to measure leakage currents from fA to μ A. We have performed DC transport measurements on a VEECO (now Bruker) *Dimension V* Conductive Atomic Force Microscope (CAFM) provided with a (Co-Cr coated Si) metallic tip. Electrically, the tip is connected to the ground of the microscope and a bias voltage is applied to the metallic sample holder, which is connected to the SrRuO₃ bottom electrode using silver paste on the side of the sample. A so-called TUNATM amplifier allows to measure currents through the film in the range of 100 fA-10 μ A, using four different gain factors (and sensitivities). Measurements are performed both as a function of temperature and applied voltage in the range of -5 V to +5V, well below the voltages at which currents associated with domain switching are observed (at about 7 V). The temperature was increased in steps of 10 K in ambient conditions from room temperature up to 155 °C. In order to prevent spurious transient currents that are related to ionic conductivity, we included a delay time of several minutes from the application of the voltage to the start of the measurements.

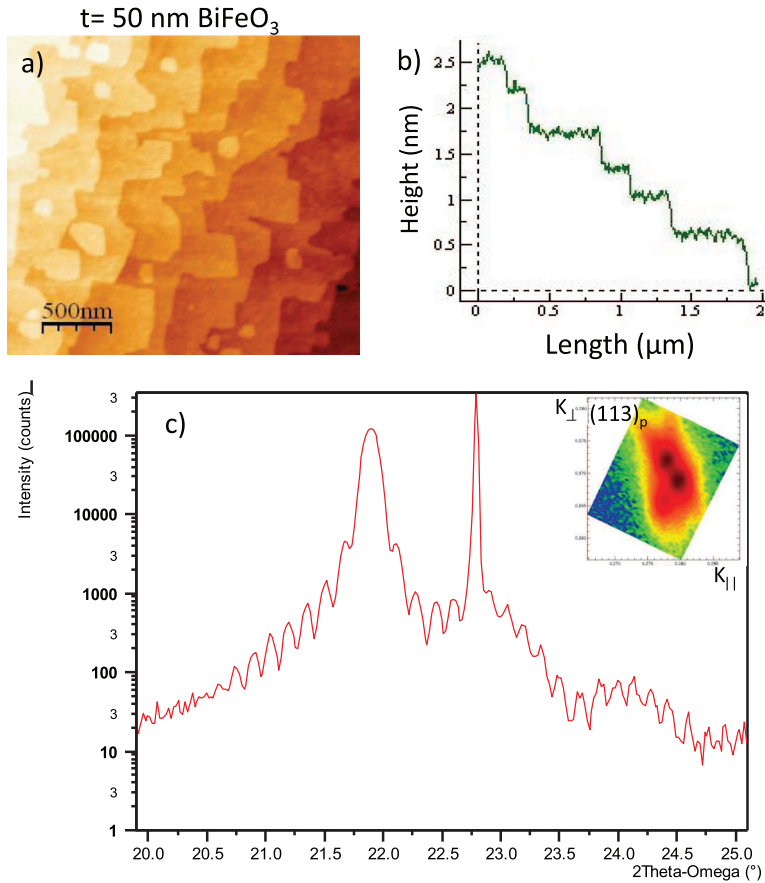


Figure 4.5: a) $2\mu\text{m} \times 2\mu\text{m}$ atomic force microscope (AFM) image of the topology of a 50 nm thick BiFeO_3 film grown by PLD on a 5 nm thick SrRuO_3 electrode on a low miscut, single-terminated, (001)-oriented, SrTiO_3 substrate. b) A linear scan of such image shows atomically flat terraces following the substrate steps. c) XRD pattern of the same film around the (001) reflection of the BiFeO_3 film (low-angle peak) and SrTiO_3 substrate (high-angle peak). The thickness fringes corresponding to both the film and the electrode are clearly visible and indicate the excellent quality of the interfaces. In the inset, a reciprocal space map around the pseudo-cubic (113)_p reflection of the film shows that it is monoclinic with the [001] direction parallel to that of the substrate[7].

Bibliography

- [1] W.T. Lee et al., J.of Phys.: Condens. Matt. **15**, 2301(2003).
- [2] E. Salje and H.L. Zhang, Phase Transitions **82**, 452 (2009) and refs. therein ; E.K.H Salje, Chem. Phys. Chem **11**, 940 (2010) and refs. therein.
- [3] J. Privratska and V. Janovec, Ferroelectrics **201**, 321 (1997); Ferroelectrics **222**, 33 (1999).
- [4] A.V. Goltsev et al., Phys. Rev. Lett. **90**, 177204 (2003); T. Lottermoser and M. Fiebig, Phys. Rev. B **70**, 220040 (2004).
- [5] M. Mostovoy, Phys. Rev. Lett. **96**, 067601 (2006).
- [6] M. Daraktchiev et al., Phys. Rev. B **81**, 224118 (2010).
- [7] C.J.M. Daumont et al., J. Phys.: Condens. Mat. **18**, 182001 (2009); S. Venkatesan et al., Phys. Rev. B **80**, 214111 (2009).
- [8] L.W. Martin et al., Nano Lett. **8**, 2050 (2008).
- [9] E.K.H. Salje and W.T. Lee, Nature Mat. **3**, 425 (2004).
- [10] D. Shilo et al., Nature Mater. **3**, 453 (2004).
- [11] J. Seidel et al., Nat. Mat. **8**, 229 (2009).
- [12] J. Seidel et al., Phys. Rev. Lett. **105**, 197603 (2010).
- [13] M.Y. Gureev et al., Phys. Rev. B **83**, 184104 (2011).
- [14] E.K.H. Salje, Chem. Phys. Chem. **11**, 940 (2010).
- [15] H. Bea and P. Paruch, Nature Mater. **8**, 168 (2009).

- [16] G.Y. Xu et al., Appl. Phys. Lett. **86**, 182905 (2005).
- [17] S.K. Streiffer et al., J. Appl. Phys. **83**, 2742 (1998).
- [18] Y.-P. Chiu et al., Adv. Mater. **23**, 1530 (2011).
- [19] H.W. Jang et al., Adv. Mater. **21**, 817 (2009).
- [20] A. Vlooswijk et al., Appl. Phys. Lett. **91**, 112901 (2007).
- [21] C.J.M. Daumont et al., Phys. Rev. B. **81**, 144115 (2010).
- [22] Y.-P. Chiu et al., Adv. Mater. **23**, 1530 (2011).
- [23] H. Liu et al., Appl. Phys. Lett. **96**, 012901 (2010).
- [24] L. Pintilie et al., Appl. Phys. Lett. **94**, 232902 (2009).
- [25] R. Ramesh (personal communication).
- [26] P.W.M. Blom et al., Phys. Rev. Lett. **73**, 2107 (1994).
- [27] T. Choi et al., Science **324**, 63 (2009).
- [28] J.G. Simmons, Phys. Rev. Lett. **15**, 967 (1965).
- [29] <http://www.tsst.nl/>
- [30] G. Koster et al., Appl. Phys. Lett. **73**, 2920 (1998).
- [31] H.W. Jang et al., Appl. Phys. Lett. **92**, 062910 (2008).
- [32] D.H. Kim et al., Appl. Phys. Lett. **92**, 012911 (2008).
- [33] Y. Ivry et al., Nanotechnology **21**, 065702 (2010).
- [34] D.L. Marasco et al., Appl. Phys. Lett. **79**, 515 (2001).

Chapter 5

Conduction mechanisms around twin walls of (001)-BiFeO₃ films

5.1 Abstract

In the previous chapters, we have first shown that we are able to engineer the shape of twin domain walls in BiFeO₃ thin films, by control of the growth conditions on a particular substrate. Second, we have shown that all as-grown twin walls display enhanced conductivity with respect to the domains during local probe measurements, though, the domains also start conducting at high enough temperature. In this chapter, we will show that both domains and domain walls are governed by the same conduction mechanisms: in the low voltage regime, electrons trapped at defect states are thermally activated, but the current is limited by the ferroelectric surface charge; in the large voltage regime, Schottky emission prevails and the Schottky barrier is locally reduced at the domain walls. Due to the selective lowering of the Schottky barrier between the film and the AFM tip, the current level quantitatively differs from a domain wall to the domain. We further discuss these results and show why other conduction mechanisms are discarded. As an example, the tunability of the conductivity upon changes in the top electrode's work function or the vacancy content is also demonstrated. This understanding provides the key to engineering conduction paths in BiFeO₃.

This chapter has been partially published as: S. Farokhipoor and B. Noheda, Phys. Rev. Lett **107**, 127601 (2011) and S.F and B. N, J. Appl. Phys. **112**, 5 (2012).

5.2 Introduction

As discussed in the previous chapter, the conductivity at 71° domain walls can be as large as that in 109° domain walls. Therefore, if we want to achieve control of walls either as devices or as parts of a device, it is crucial to understand the mechanism or mechanisms for selective conduction through domain walls and, in case that there is more than one possibility, to find out which one is most robust and convenient. We show in this chapter that the main origin is the lowering of the Schottky barrier between the BiFeO₃ n-type semiconducting film and the metallic top electrode. The predicted reduction of the band gap at the walls[1] would then appear as a secondary effect, responsible for subtler changes in conduction. This becomes now essential because, according to recent reports, conduction at domain walls is a rather general phenomenon[2], only the most relevant mechanisms seem to vary. As one can expect, different conduction mechanisms are likely to have different relevance in different types of walls. Fowler-Nordheim (FN) tunneling has been put forward as the mechanism for conduction in artificially-written 109° domain walls[3; 4]. Recent work has also focused on walls between ferroelectric 180° domains, which do not involve strain gradients[2; 5] and indeed a different conduction mechanism (bulk-limited Poole-Frenkel emission) has been observed in this case. Similarly, charged walls show again different conduction characteristics[6]. Later work has gone further in exploring the conduction involved in truly one-dimensional conduction paths defined by vortex states in ferroelectrics, around which both charged walls and large strain gradients coexist[7]. In this chapter, we focus on ferroelastic domain walls of BiFeO₃ thin films to complement the results reported in chapter 4. We include here a detailed analysis of the different conduction mechanisms that have been considered and the reasons why they have been discarded, as well as how the Schottky barriers have been calculated. In the view of chapter 6, this could simply be explained by the fact that DW's are non polar. For that we need to know when the oxygen content decreases, what happens with the conduction level at the domains, while the conduction at DW increases. We also point out that the lowering of the barrier at the walls is likely to be induced by migration of charged defects to the walls (as it is common in other perovskites[8]), since that would create a potential step at the interface[9]. We postulate that the charged defects are oxygen vacancies, based on our observations. Although some work has already been done regarding this issue[3], no clear picture exist yet. The present chapter provides signific-

ant progress in this direction. In addition, our results on different types of top electrodes corroborate our claim of a dominant interface-limited mechanism.

5.3 Results and discussion

As mentioned in chapter 4, the large differences in the current level displayed by 71° DWs in BiFeO_3 films grown on SrTiO_3 by Chiu et al.[10] using scanning tunneling microscopy and by us can be explained by three reasons: a) due to the nature of the interfaces[11; 12], which may invoke different conduction mechanisms, b) the role of oxygen vacancies, and/or c) large strain effect induced by the substrate[13]. The first two reasons will be discussed in more details in the following chapter. It has to be mentioned that due to high stability of 71° domain walls, we have focused most of our studies on those. The magnitude of the measured current at the walls is about 10 pA at 3 V at room temperature and can increase up to 3nA for temperatures around 150°C . By measuring I-V curves as a function of temperature (above room temperature), we have evaluated the three most likely mechanisms leading to conduction through a metal-semiconductor-metal system, as well as the possibility of space charge limiting the current.

In this chapter, the high and low voltage regime will be used as referring to ranges of voltages in the 3.8-5V (SRS mechanism) and 2-3.5V, respectively. The lower voltages regime ($\leq 2\text{V}$) is eliminated due to zero conduction level with respect to the noise level of our microscope. Higher voltages are not considered as they impose the risk of undesirable ferroelectric switching event(at $\sim 7\text{V}$). We have considered a linear dependence between the applied voltage and the electric field, which is not obvious given the fact that one of the electrodes is a sharp tip. However, recently, Guyonnet et al.[2] have shown that this is, indeed, a good approximation. Figure 5.1 a) represents the data in coordinates related to Fowler-Nordheim tunneling (see chapter 1), that is $\ln(I/V^2)$ is plotted against $1/V$ for different temperatures. Fowler-Nordheim tunneling should be temperature-independent and, in these coordinates, should show a linear dependence. Figure 5.1 a) shows quite linear behavior mainly in the 3-5V region but there is a clear temperature dependence that indicates that this is not the relevant mechanism for conduction.

Another possible mechanism is Poole-Frenkel (PF) emission, by which

current is supported by thermal emission from trapped carriers in the bulk of the semiconductor, where the trap barrier is lowered by the electric field. This has been reported to be the main conduction mechanism in some ferroelectric oxides, including BiFeO₃ [12] and PZT[2]. The field and temperature dependence of the PF currents are similar to those of the Richardson-Schottky (RS) emission, a third mechanism to be considered. Typically, the best way to distinguish between the two of them are thickness dependent measurements. In cases where the structure of domain walls and the types of defects may depend on the film thickness, this is not generally possible. In addition, it is highly probable that tunneling would become dominant at very low thicknesses. Therefore, an alternative test is to extract the high-frequency (dynamic) dielectric constant from the slopes of the linearized plots, and to check in which case it agrees with that known for the material[14]. Note that the Richardson-Schottky equation is only strictly correct in the case of semiconductors with relatively small electronic mean free paths; while for insulators the modification proposed by Simmons (which we will call Simmons-Richardson-Schottky (SRS) emission)[15] should apply.

Thus, in Fig 5.1 b) - c), we plot the data in the coordinates that make the current data due to PF emission or SRS emission linear and temperature-independent ($T \ln(I/V)$ versus $V^{1/2}$ and $T \ln[I/(VT^{3/2})]$ versus $V^{1/2}$, respectively). In this way, in both plots, all the curves (independent of temperature) should show the same intercept and the same slope, which is inversely-related to the optical dielectric permittivity[14]. The linearity of the fits is considerably improved compared to the FN tunneling fit, in particular at higher temperatures and higher voltages. One can see that the slopes are in both cases (PF as well as SRS) temperature-independent in a very good approximation. The collapse of the intercept seems better in the SRS case (leading to a well-defined Schottky barrier). However, it is the value of the optical dielectric permittivity extracted from the slopes what makes us conclude that Schottky emission (SRS) is the pertinent conduction mechanism in this case: In the case of PF emission an unphysical (≤ 1) value of 0.4 ± 0.1 for the optical dielectric permittivity is obtained from the slopes of Fig 5.1 b) for 71° domain walls and a value of 0.16 ± 0.06 is found for the domains. For SRS emission, a dielectric permittivity of 6.5 ± 1.5 is found at the 71° domain walls (from figure 5.1 c)), in perfect agreement with the expected value of 6.25 (see e.g.[16]). A value of 3.6 ± 0.1 is found at 109° domain walls; while a worse agreement of 1.8 ± 0.3

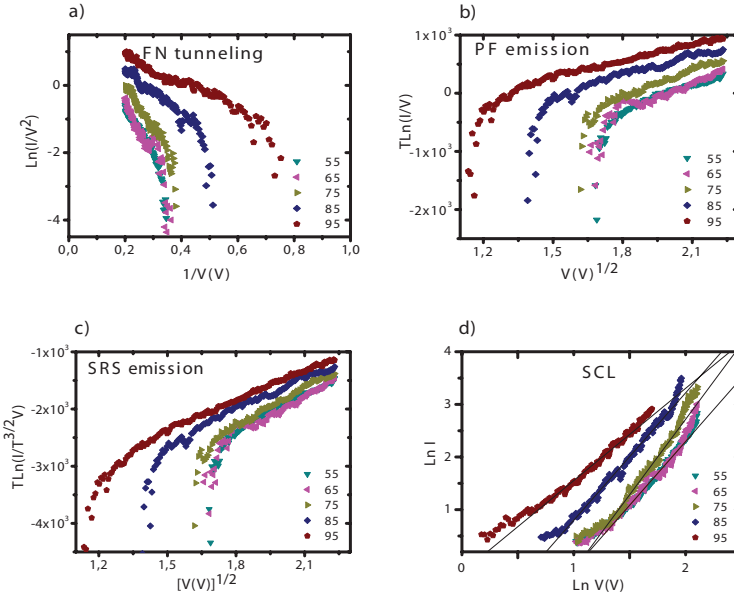


Figure 5.1: The measured I - V curves for different temperatures at 71° domain walls are plotted with different axes in order to make the curves linear and temperature-independent for a) Fowler-Nordheim (FN) tunneling; b) Poole-Frenkel (PF) emission; c) Simmons-Richardson-Schottky (SRS) emission and d) space charge limited (SCL) current. a) shows temperature dependent slopes that are inconsistent with the FN mechanism; the slope in b) leads to a too small optical dielectric constant of 0.4 ± 0.1 ; while the slope of c) gives the right value of 6.5 ± 1.5 . d) shows the data for voltages below 3.7 V, which deviate from linearity in figure 5.3 c). Power laws with exponents close to 2 seem to fit the data reasonable well in agreement with a space charge limited regime.

is obtained for the domains (still better than that of the PF mechanism). It is worth to mention that, due to the low values of the current inside the domains, these data are very noisy and only a few higher temperature curves could be analyzed.

One can see in Fig. 5.1 b) - c) that at the lower voltages the data deviates from the linear trend indicating a different behavior. The lower the temperature, the higher the voltage at which the SRS regime crosses over to this low voltage regime. It is known that the general signature of space charge limited (SCL) conduction in an insulator of thickness d (with parallel-plate electrodes) is $I \propto V^n / d^{n+1}$, where V is the applied voltage and

$n \geq 2$ ($n = 2$ in the absence of traps)[17]. Typically, the SCL regime is found at the higher voltages (once there are enough carriers in the insulator to build up space charge). However, charged defects or, in a ferroelectric material, the polarization surface charges themselves can behave similarly to the space-charge regions and could lead to a similar I-V dependence[18]. In Fig. 5.1 d) we plot the low voltage data that, according to Figure 5.1 c), deviates from the linear Schottky emission behavior. As will be discussed further, in this low voltage regime (2.5-3.5V) this deviation is more frequently observed at the lower temperatures and it is in reasonable agreement with an $n = 2$ slope. Therefore, our studies on conduction mechanisms on different domain walls and domains put forward two types of mechanisms. For low voltages, conduction behaves as space-charge limited. This can be observed from the slope of the curves in the left column of figure 5.2 for a domain and two different domain walls. The temperature dependence in this regime shows Arrhenius thermal activation (see Figure 5.3). The slope is around 2[19] for voltages ranging from 2 V (where appreciable conduction starts) to about 3-3.5 V (depending on temperature), and the activation energies corresponding to the upper(3.3V) and lower(2.4V) voltage limits in this regime from Arrhenius fits are 1.003 eV and 0.56 eV, respectively. In figure 5.3, we show the fit for $V=3$ V. The activation energies extracted from the Arrhenius plots are 0.73(9)eV, 0.9(4)eV and 0.65(1)eV for 71°, 109° and off-wall, respectively, consistent with defect states located below the bottom of the conduction band. These values are too large for single electron traps at oxygen vacancies but they agree with those at clusters of oxygen vacancies in perovskites, and those reported for 109° domain walls[3]. At large enough voltage (and temperatures), Simmons-Richardson-Schottky (SRS) is observed[15], as evidenced by the linear behavior in Figure 5.2 (right column). The axes in the plots are chosen such as to display the same slope for the different temperatures. The slopes are shown with dashed lines. It can be seen that the higher the temperature, the larger the voltage range for which SRS is observed.

It is unusual that a space-charge-limited-like regime takes place at low currents, but an explanation for this is provided by Blom et al.[18]: the ferroelectric surface charges themselves create a space-charge-like region giving rise to the $I \propto V^2$ dependence.

However, for the high voltage regime, the barrier heights obtained from fitting the SRS equation[9; 20] differ considerably between points on the domain walls and points within a domain, being 0.8(1)eV, 0.9(1)eV for the

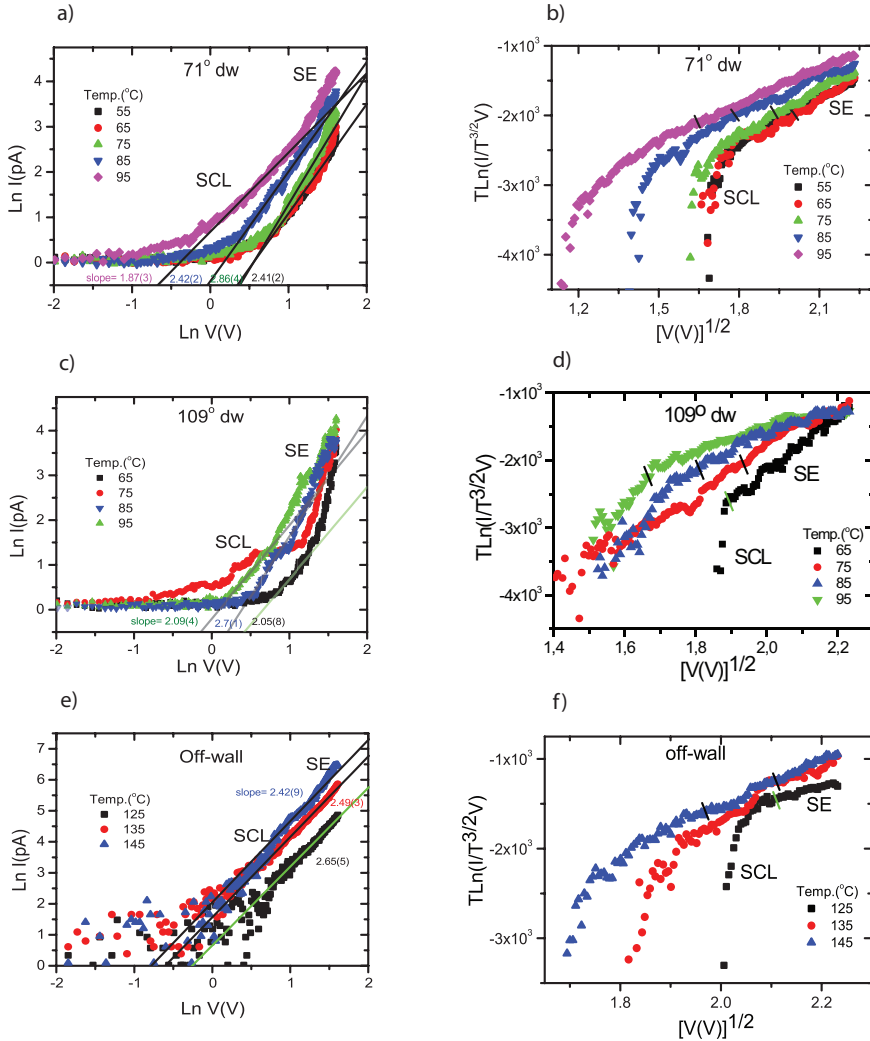


Figure 5.2: The I - V characteristics of figures 5.3 b), 5.3 c) and 5.3 d) (shown in chapter 4) plotted in: (left column) log-log scale in order to show linear behavior with slope around 2 in the space-charge limited (SCL) regime and (right column) as $(\ln I / (T^{3/2} V))$ versus $V^{1/2}$ to show linear behavior in the Schottky-Simmons emission regime. In this regime, the slope, which should be common to all temperatures, is represented as dashed lines. The short marks - leading to the best regression coefficient - on the curves indicate the crossover to the Schottky emission regime. The I - V curves are measured at the 71° DW (top), 109° DW (center) and off-wall (bottom).

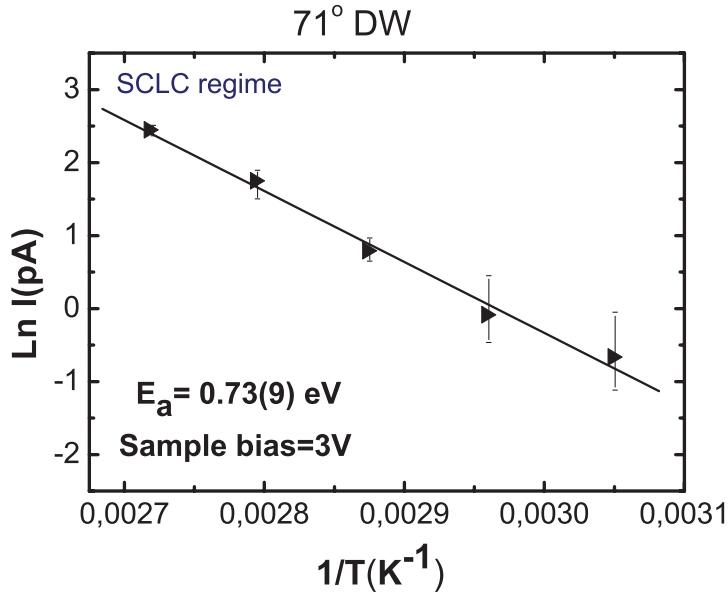


Figure 5.3: Arrhenius plot for the 71° domain walls in the low voltage regime, where the current shows a V^2 dependence (SCLC). An activation energy of 0.73(9)eV is obtained at sample bias equal to 3 volt.

71° and 109° DWs, respectively, and 2.6(7)eV off the wall. It is worth to mention that we are measuring in air through a layer of adsorbates and therefore, these values correspond to effective Schottky barrier height. This large difference explains the lower currents measured at the domains and its reduction at room temperature below the sensitivity limit of the TUNATM amplifier(5fA). To calculate the Schottky barrier height we follow ref.[22]: we first plot $\text{Ln}(I/VT^{3/2})$ versus $1/T$. A linear fit should be obtained for the proper voltage regime (voltage large enough to support the Schottky emission mechanism, in our case above 3.8V). Figures 5.4 a) - f) show the fits for specific voltages. Φ_{apparent} is defined as the slope of these linear fits. This is the exponential term in the Simmons-Richardson-Schottky emission[15]: $(-\Phi_o/k_B)+(e/k_B)(eV/d\pi\epsilon_o K)^{1/2}$, where Φ_o is the Schottky barrier, k_B is the Boltzmann constant, ϵ_o is the permittivity of free space, K is the dielectric constant, V is the applied DC bias and d is the thickness of the film. Next, we plot the slopes versus $V^{1/2}$ (Figure 5.4 g)). The intercept of the obtained graph (at $V=0$) is the Schottky barrier height.

The barrier height for 71° domain walls is determined to be (0.8 ± 0.2) eV, however, inside domains this value changes to (2.6 ± 0.6) eV, (error bars are determined from linear regression).

Oxygen vacancies play a very important role in controlling the conduction in these film. This has been clearly observed by making samples with different oxygen contents, either by changing the cooling rate or the oxygen pressure after growth, but otherwise growing them under identical conditions. These results are summarized in Figure 5.5 and 5.6. In figure 5.5, three C-AFM images are displayed for samples with low, medium and high vacancy content. An increasing amount of current is obtained with decreasing oxygen content at the domain walls. A clear dependence of the current with growth oxygen pressure was also observed by Seidel et al.,[3] in 109° twin walls. However, in figure 5.6, the oxygen vacancy distribution inside one domains in the same type of samples is shown (the corresponding piezoresponse presenting the exact boundary between two domain walls by a domain). As it can be seen the current value increases by a factor of 10 from high oxygen content sample to low oxygen content. However, the current magnitude inside a domain just changes by a factor of 2 or less. This is the key issue for resistive switching in our samples which will be discussed in more detail in chapter 6.

The presence of n-type defect states in the band gap (oxygen vacancies) will have two effects: first, to enable the thermally activated electrons from defect states inside the band gap to be promoted to the conduction band, and second, the effect of reducing the Schottky barrier[23]. This second effect is critical to control conduction at domains and domain walls, since it determines the large current regime. The role of oxygen vacancies is, thus, direct only in the low current regime. In the large current regime (the interesting one for applications) the oxygen vacancies do not directly provide the carriers, but lower the Schottky barrier more in the domain walls ($0.8(1)$ eV) than in the domains (2.6 eV), probably caused by a larger density of oxygen vacancies in the domain walls, meaning that the Schottky barrier will be adjustable by changing the density of oxygen vacancies, both during growth and annealing procedure (as shown in figure 5.5). In other words, the carriers are electrons injected from the conductive AFM tip. A large number of vacancies must be present in the films in order to avoid the current to be limited by the ferroelectric polarization. Further support for our model is provided by samples grown at a higher oxygen pressure (300 mbar instead of 100 mbar). In this case, the "space charge

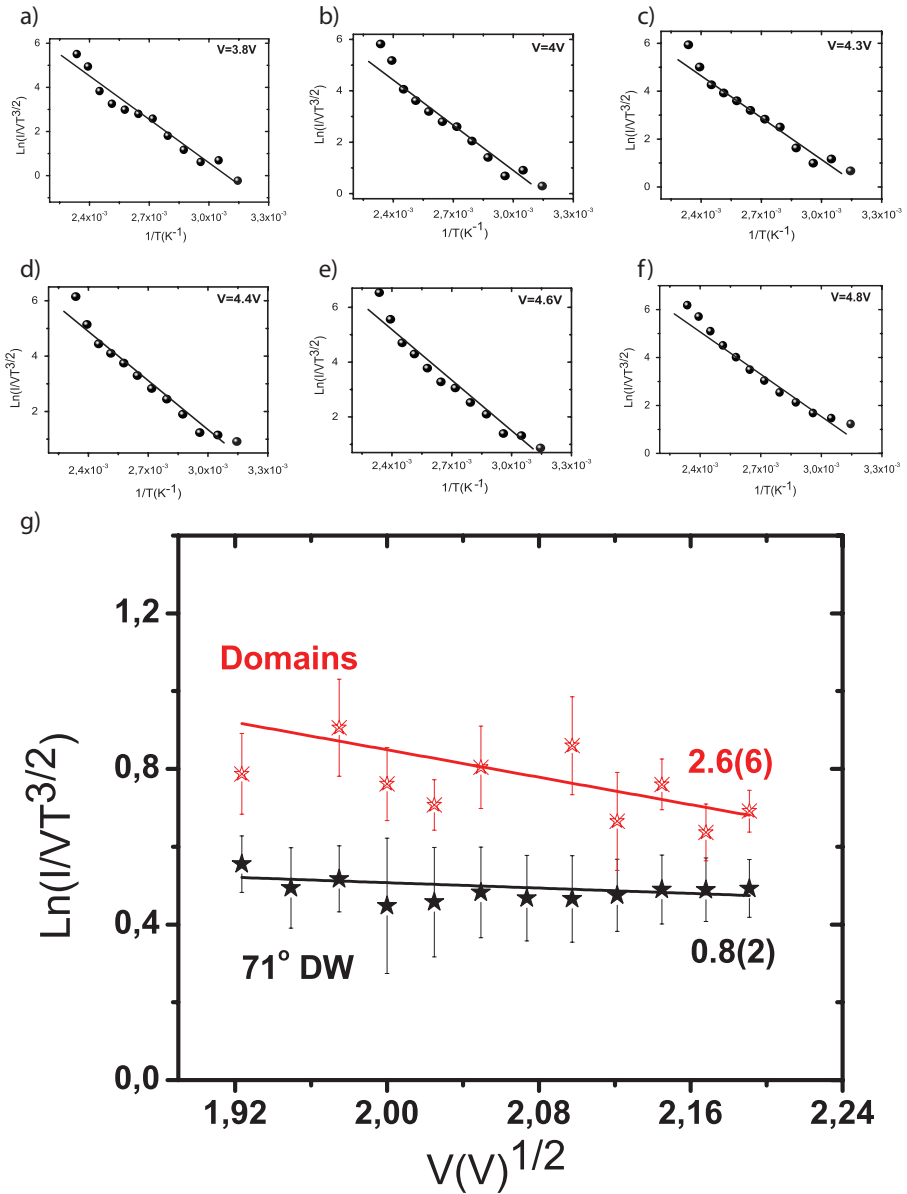


Figure 5.4: $\text{Ln}(I/(VT^{3/2}))$ versus T^{-1} for 6 particular voltages, $V= 3.8 \text{ V}$ (a), $V=4\text{V}$ (b), $V=4.3\text{V}$ (c), $V=4.4\text{V}$ (d), $V=4.6\text{V}$ (e), $V=4.8\text{V}$ (f), limits within which the SRS mechanism is observed. The slopes of those curves correspond to what has been called ϕ_{apparent} [12]. g) According to the SRS mechanism, ϕ_{apparent} vs. $V^{1/2}$ should show linear behavior, with the intercept at the origin being the Schottky barrier height (ϕ_o). The ϕ_o values extracted in this way for domains and domain walls are indicated in the plot.

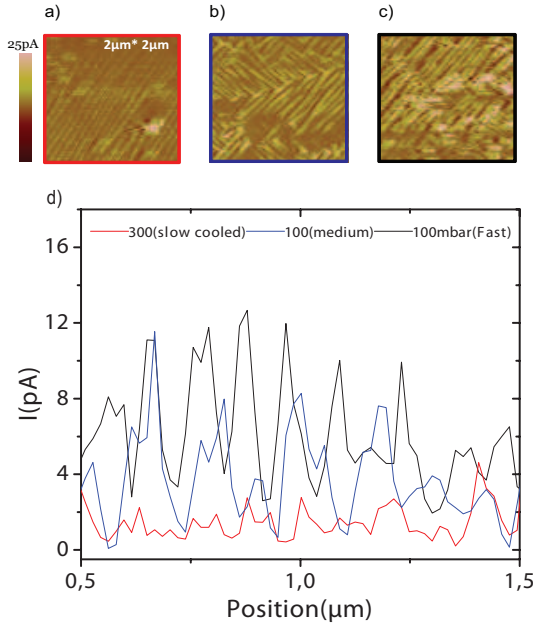


Figure 5.5: C-AFM images on an $2\mu\text{m} \times 2\mu\text{m}$ area for three samples grown under identical conditions but cooled down after growth a) under an oxygen pressure of $PO_2 = 300$ mbar and a cooling rate of $2\text{K}/\text{min}$; b) under $PO_2 = 100\text{mbar}$ and cooling rate of $3\text{K}/\text{min}$ and c) under $PO_2 = 100\text{mbar}$ and cooling rate of $30\text{-}4\text{K}/\text{min}$. The current scale is the same for the three images d) Linear scans across $1\mu\text{m}$ of the previous images are shown in red (for a)), blue (for b) and black (for c)).

limited regime” (or more properly, the $I \propto V^2$ regime governed by the ferroelectric polarization) prevails up to the maximum measured bias (5V) for temperatures below 85°C and only above this temperature is an increase in the current observed. The behavior in the large temperature regime resembles that reported by Pintillie et al.[16]: Schottky emission with an unphysically small barrier of (0.14eV , in our case) due to the influence of the ferroelectric polarization. This is indeed consistent with the fact that, in this sample with a lower number of oxygen vacancies present, the surface charges of the ferroelectric polarization are not completely neutralized by the oxygen vacancies.

This brings forward the following scenario, shown in figure 5.7: the conduction observed in the low voltage regime is originated from thermally ex-

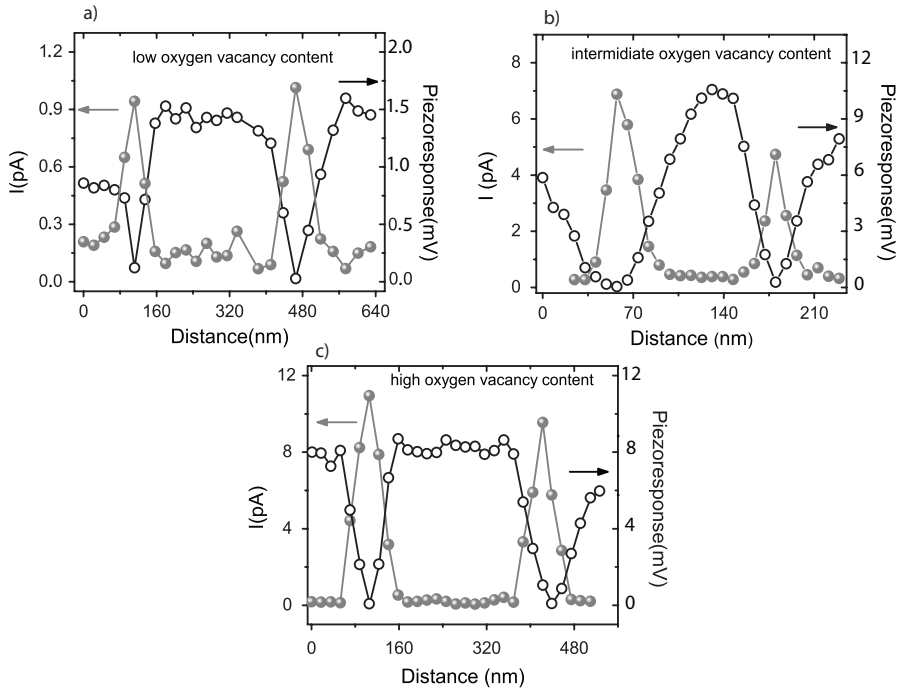


Figure 5.6: *C-AFM and amplitude of piezoresponse images of a domains and two adjacent domain walls on three samples grown under identical conditions but cooled down after growth a) under an oxygen pressure of $PO_2 = 300$ mbar and a cooling rate of $2K/min$; b) under $PO_2 = 100$ mbar and cooling rate of $3 K/min$ and c) under $PO_2 = 100$ mbar and cooling rate of $30-4 K/min$.*

cited electrons from defect states (possibly related to oxygen vacancies) located close to the bottom of the conduction band. With increasing voltages, oxygen vacancies move towards the surface and reduce the Schottky barrier with the top electrode, which eventually allows large conduction through the films.

This effect is, however, not homogeneous across the film: strain gradients associated to ferroelastic domain walls create an inhomogeneous distribution of oxygen vacancies and the selective reduction of the Schottky barrier around the walls. The mechanism for conduction is thus expected to be different in non-ferroelastic domain walls, and thus there is no driving force for accumulation of defects (assuming that walls are not charged).

Our analysis of the $I(V,T)$ dependencies can be summarized as follows:

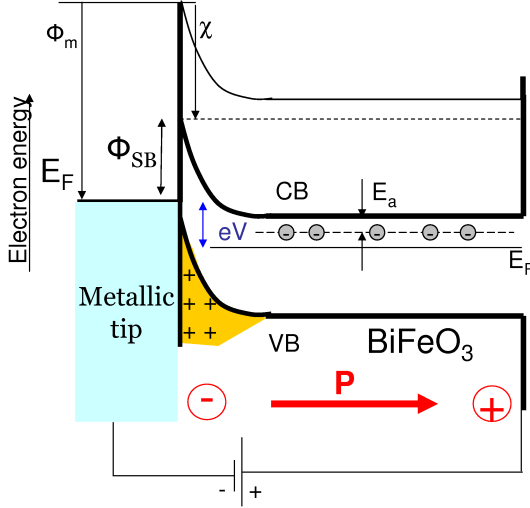


Figure 5.7: Sketch of the band bending at the tip- BiFeO_3 interface in the large voltage regime showing the Schottky barrier. In the low voltage regime, before emission takes place, electrons trapped in defect states are thermally promoted to the conduction band (activation energy E_a). In this low voltage regime, the ferroelectric polarization limits the current, the band diagram drawn in the case that the voltage has been held at zero bias.

the large currents (high voltage -high temperature) are interface-limited, while the low currents are bulk-limited. While these conclusions drawn from the $I(V,T)$ dependencies are convincing on their own, additional support of our interpretation can be gained by comparing results obtained for different top electrode materials (AFM tips). In fact, the bottom electrode has been grown at high temperature and low pressure, and is thus an epitaxially grown layer. This implies that the bottom interface should be free from extended structural defects, in contrast to the top interface, which is the contact between the surface of the sample and the microscope tip that is held at ambient pressure during the measurements. This contact depends on more parameters, such as contact force and depletion setpoint. Therefore, here we investigate the role of different type of top electrodes. This can contribute to the tunability of barrier height, as well as provide supplementary proof of an interface conduction mechanism. As it is presented in figure 5.8, the obtained Schottky barrier heights from

SRS analysis are 0.79eV and 0.98eV for two types of silicon tip with chromium/cobalt and platinum coatings, respectively. Importantly, however, the optical dielectric constants obtained for BFO with the two different tips are in good agreement with each other.

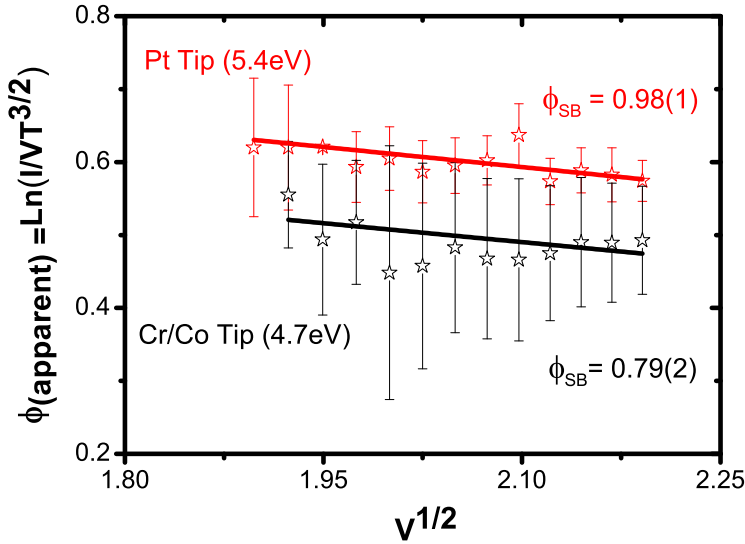


Figure 5.8: SRS representation of $I(V)$ curves obtained with two different types of top electrodes, giving rise to two different Schottky barrier according to the SRS mechanism (values extracted for two different types of top electrodes are indicated in the plot).

5.4 Conclusion

To conclude, we have observed that in (001)- BiFeO₃ thin films grown on SrRuO₃-buffered (001)-SrTiO₃ substrates, the mechanisms for conduction are the same both at the domain walls and at the domains: the low current regime is supported by thermally activated electrons from defect (oxygen vacancies) states and limited by the ferroelectric polarization; the large current regime, biased above about 3.8 V (for films with thickness of about 50nm) are determined by the Schottky barrier heights at the interface between the BiFeO₃ film and the Co-Cr tip. This barrier is largely

decreased in the domain walls with respect to the domain, causing the observed conduction enhancement at the walls. The large currents are therefore interface limited and can be controlled by engineering the work function of the injection electrode and the defect density (significant role of oxygen vacancies) in the BiFeO_3 layer. At low voltages the current behaves as if it would be limited by space charge. The importance of the interplay between the surface polarization charges and the charged defects have been recently put forward in BiFeO_3 single crystals by [24] and in films [6; 7]. This interplay is, of course, very different at the domain and at the walls and it has been investigated in relation with domain/domain wall conductivity in the present BiFeO_3 thin films. The results will be discussed in the next chapter [25].

5.5 Experimental

BiFeO_3 thin films were grown by pulsed laser deposition (PLD) assisted by RHEED using a system designed by Twente Solid State Technology (TSST) [26] provided with an excimer laser (Lambda Physik COMPex Pro 205) filled with KrF to produce a wavelength of 248 nm. The operating laser frequency and fluence were 0.5 Hz and 2 J/cm², respectively. The chamber was evacuated up to a background pressure of 10⁻⁸ mbar. The films were grown at a temperature of 670°C in an oxygen pressure of 10⁻¹ mbar. After growth, the oxygen pressure was increased to 100 mbar and the films were cooled down at a rate of 3° C/min, except in particular cases in which we intended to investigate the effect of different oxygen vacancy content, for which the cooling rate was decreased (increased) or the oxygen pressure was increased (decreased).

Bibliography

- [1] A. Lubk et al., Phys. Rev. B **80**, 104110, (2009).
- [2] J. Guyonnet et al., Adv Mater. **23**, 5377 (2011).
- [3] J. Seidel et al., Phys. Rev. Lett. **105**, 197603 (2010).
- [4] P. Maksymovych et al., Nano Lett. **11**, 1906 (2011).
- [5] P. Maksymovych et al., Nanotechnology **22**, 254031 (2011).
- [6] E.A. Eliseev et al., Phys. Rev. B **85**, 045312 (2012); E.A. Eliseev et al., Phys. Rev. B **83**, 235313 (2011).
- [7] N. Balke et al., Nat Phys. **8**, 81 (2011).
- [8] W.T. Lee et al., Phys. Rev. B **72**, 104116 (2005); M. Calleja et al., J. of Phys.: Condens. Matt. **15**, 2301 (2003).
- [9] S.M. Sze and K.N.G. Kwok, "Physics of Semiconductor Devices", Third Edition. Ed. Wiley- Interscience, New Jersey (2007).
- [10] Y.-P. Chiu et al., Adv. Mater. **23**, 1530 (2011).
- [11] H. Liu et al., Appl. Phys. Lett. **96**, 012901 (2010).
- [12] L. Pintilie et al., Appl. Phys.Lett. **94**, 232902 (2009).
- [13] A.N. Morozovska et al., Phys. Rev. B **86**, 085315 (2012).
- [14] J. G. Simmons, Phys. Rev. **155**, 657 (1967).
- [15] J. G. Simmons, Phys. Rev. Lett. **15**, 967 (1965).
- [16] L. Pintilie et al., J. Appl. Phy. **98**, 124104 (2005).

- [17] A. Rose, Phys. Rev. **97**, 1538 (1955).
- [18] P.W.M. Blom et al., Phys. Rev. Lett. **73**, 2107 (1994).
- [19] It is worth to notice that these are local measurements using the AFM tip and that the electric field is highly inhomogeneous. A perfect quantitative agreement with the well-known conduction equations is thus not expected and our slope values of 1.8-2.8 can be considered in good agreement with the expected slope 2.
- [20] In this work we are assuming that the BiFeO₃ is fully depleted and that the field at the interface (E_o) is proportional to the applied bias (V)[16; 21].
- [21] P. Zubko et al., J. of Appl. Phys. **100**, 114112 (2006); P. Zubko et al., J. of Appl. Phys. **100**, 114113 (2006).
- [22] L. Pintillie et al., Phys. rev. B **75**, 104103 (2007).
- [23] M. Dawber et al., J. of the Europ. Ceramic Soc. **21**, 1633 (2001).
- [24] H.T. Yi et al., Adv. Mater. **23**, 3403 (2011).
- [25] S. Farokhipoor and B. Noheda (to be submitted); Oral presentation at the Fall MRS meeting (symposium P14.3), Boston December (2011).
- [26] <http://www.tsst.nl/>

Chapter 6

Ferroelectric resistive switching in BiFeO_3 thin films

6.1 Abstract

In the previous chapters, we have discussed the mechanisms underlying domain formation in BFO epitaxial films, showing the possibility of engineering twin domain structures as a function of BFO layer. We have also shown that both domain walls and domains are conductive and dominant conduction mechanisms were determined by detailed studies looking at all possible conduction mechanisms. Also, the crucial role of oxygen vacancies on the conduction level has been demonstrated. In this chapter, we will discuss another way to tune the conductance. We will show that upon switching the ferroelectric polarization in a BiFeO_3 film, a change of 1.7 eV in the height of the Schottky barrier with the electrode can be obtained. This agrees with recent predictions showing that the incomplete screening at the metal electrodes and the bound polar charges at the interfaces are the key ingredients to explain resistive switching in BiFeO_3 films. Moreover, these quantitative local measurements allow to estimate the relative effect of screening charges, and polar charges on the Schottky barrier heights.

This chapter has been submitted; S. Farokhipoor and B. Noheda, arxiv no. 1212.0483

6.2 Introduction

Using metal-ferroelectric junctions as switchable diodes was proposed several decades ago[1]. This concept was demonstrated by Blom et al.[2], who reported switching in the rectification direction and changes of the current of about 2 orders of magnitude upon switching the polarization direction of the ferroelectric layer. This form of resistive switching makes it possible to read the state of a ferroelectric memory faster than with the capacitive design and without destroying the information in each reading cycle[3–5]. Recently, Jiang and coworkers have shown that these Schottky barrier effects are enormous in BiFeO₃ giving thousand times more switched charge than found by Blom in PbZr_{1-x}Ti_xO₃ (PZT)[6].

Apart from the examples mentioned above and few others[7], transport through ferroelectrics had not been investigated in detail until less than a decade ago. The reason for that is the large turn-on voltages that were expected for the Schottky behavior of these large band-gap semiconductors[8]. However, as the thin film deposition techniques improve and better layers with lower thicknesses are achieved, metal-ferroelectric-metal heterostructures become more interesting: indeed, the surface charge in a ferroelectric semiconductor plays the same role as the doping charge and it is, in principle, possible to modify the barrier characteristics from Schottky to ohmic without having to dope the material[2; 8]. Resistive switching with ferroelectric layers has attracted a lot of attention in recent years[6; 9–15]. One can consider the metal-ferroelectric junction as a Schottky contact, with the ferroelectric polarization modelled as a charged sheet at a certain distance of the physical interface with the electrode[16; 17], in order to account for the so-called 'dead layer'[18]. Assuming small (and nonoverlapping) depletion layers, this model has given experimental Schottky barrier height (SBH) values in the range of $\Delta\phi=0.2-0.9$ eV for various ferroelectrics and orientations[19–21]. However, in order to model realistic metal-ferroelectric-metal heterostructures, considering the incomplete screening of the polarization surface charges is needed[22]. For bad metal electrodes (large screening lengths) and for ultrathin ferroelectric layers, as those requested for tunnel junctions[23; 24], the charge at the electrode may not be enough to screen the polarization and a large depolarization field may be present[25; 26].

Classically, the origin of the 'dead layer' (non-switchable interface layer) was assumed to be associated to defects in the film. But even in the case of an ideal, defect-free ferroelectric layer, a certain 'dead-layer' or series

capacitance always exists due to different ionic displacements at the interface, which could be in some instances more important than the electronic effects due to imperfect screening[27–29] or even give rise to a super-polarized layer (‘negative dead layer’)[30]. It is worth noticing that in all cases (defective interfacial layers, Thomas-Fermi screening lengths or different ionic displacement at the interface), the system can be modelled by adding an interfacial capacitance in series with the ferroelectric interface, the system can be modeled by adding an interfacial capacitance in series with the ferroelectric capacitance[27–30].

Following the Thomas-Fermi approach, Zhuralev et al.[31] pointed out that using electrodes with different screening lengths would lead to changes of several orders of magnitude in the tunneling conductance through a ferroelectric upon polarization switching (*giant electroresistance effect*)[22; 31]. Less discussed has been in the way in which ferroelectric switching modifies the resistance through thicker layers (when direct tunneling is not possible) in case of incomplete screening at the electrodes. In this case of thicker layers, the average potential barrier height across the ferroelectric layer is not the determining parameter for conduction and resistive switching can be obtained with symmetric electrodes[27].

First-principles calculations that consider the ferroelectric as a perfect insulator, predict changes in the SBHs of up to 2.6 eV, upon ferroelectric switching, in the case of PbTiO_3 (large ferroelectric polarization) with SrRuO_3 electrodes (large effective screening length)[27]. A 1D electrostatic model, that takes into account conduction through the ferroelectric as well as the imperfect screening at the electrodes, has recently shown that the SBH changes induced at the metal- BiFeO_3 interface are significantly larger at the Pt electrode than at the SrRuO_3 electrode.[12; 32]. This is in contradiction with first principles calculations[25; 27; 30] and recent experiments[33] that show smaller SBH changes for the noble metal electrodes (with smaller effective screening lengths). Moreover, it is believed that the presence of vacancies and charged defects plays an important role determining conduction through the ferroelectric layers (in fact, resistive switching is often found in non-ferroelectric materials)[34] so that both polarization charges and defect charges need to be considered to understand the resistive switching phenomena in ferroelectrics[6; 10–15]. However, there does not seem to be a clear understanding about the relative importance of the two. In order to shed light on the open problems discussed above, we have locally measured the SBHs in down-polarized

domains, up-polarized domains and non-polar domain walls (DWs) of epitaxial BiFeO₃, a ferroelectric that is known to display remarkable resistive switching[6; 11; 12]. We measure a change of the effective SBH as large as 1.7 eV between the as-grown down-polarized domains and the up-polarized domains, when used a Cr-coated tip of an AFM microscope as the top electrode and an epitaxial SrRuO₃ layer as bottom electrode. These measurements allow estimating the relative effect of polarization charges and screening charges on the conduction through the ferroelectric.

6.3 Results

BiFeO₃ thin films with thicknesses of 70 nm were grown by pulsed laser deposition on single-terminated (001)-oriented SrTiO₃ substrates covered by a 5nm thick buffer electrode layer of SrRuO₃, as described in chapter 3 and 4[35; 36] (see also experimental section). The as-grown films were self-polarized with the polarization pointing down (towards the substrate), that is, with only four of the eight pseudo-rhombohedral domains present, see chapter 3[37]. This preferential poling is common in ferroelectrics[38] and could be due to deviations in the surface chemistry or be caused by the preferential termination during growth.

In BiFeO₃ thin films similar to those used here (same substrate, same growth conditions, same lab), enhanced conduction through the DWs with respect to that of the domains, has been shown to be determined by the height of the Schottky barrier at the metal-semiconductor interface; the SBH is shown to be significantly reduced at the domain walls, as discussed in chapter 5[35; 36]. That is consistent with earlier reports by Pintilie et al. showing that the SBH determines the current through a thick BiFeO₃ films when using macroscopic electrodes[19]. Figure 6.1 shows the apparent SBH as a function of $V^{1/2}$, from the extrapolation to the ordinate axis, the (zero-voltage), SBH are obtained[19]. The SBH was measured to be as high as $\phi_{\downarrow} = 2.6(6)\text{eV}$ in the as-grown, down-polarized domains, (see chapter 5). All the experiments were consistent with a n-doped BiFeO₃ layer (as expected from the presence of oxygen vacancies) and injection of electrons from the top Cr-electrode. To a first approximation, the difference between the work function of the metal and the electron affinity of BiFeO₃ gives rise to the SBH[39; 40], of about $\phi_o = 1.4\text{eV}$ for the top Co/Cr-BiFeO₃ interface[41], if we considered non-polar BiFeO₃. A polarization pointing down inside the ferroelectric domains will induce negative surface charges

at the top interface and will increase the SBH for electrons injected from the Cr electrode, as indeed observed.

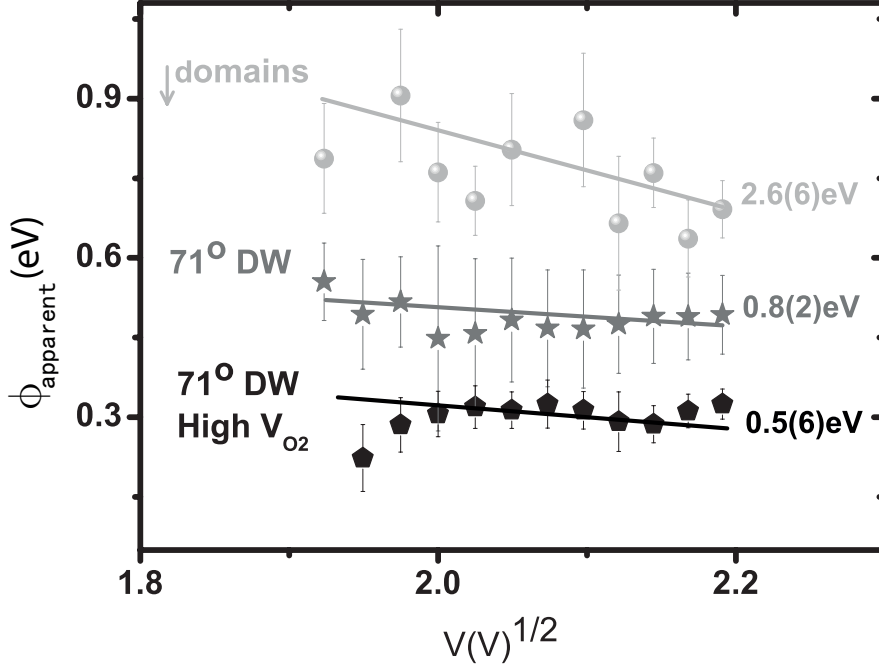


Figure 6.1: The intercept at the origin shows the experimental (zero voltage) Schottky barrier height (SBH) at the down-domains (red circles) and at 71° domain walls of two samples with less (black stars) and more (blue pentagons) oxygen vacancies.

In order to further investigate the effect of polarization, we locally switch the out-of-plane component of the polarization up, such that now positive bound charges are induced at the top interface. This should decrease the barrier for electronic injection. Indeed, as observed by other groups in bulk and thin film samples[6; 11; 12], a much larger conduction level is observed in the up-polarized region (see Figure 6.2). The I-V curves measured at different temperatures (at and above room temperature) both at the up- and down-polarized domains are shown in Figure 6.3. In Figure 6.4 a) the up-polarized Richardson-Schottky-Simmons[42] plots are shown (for those corresponding to the down-polarized domains see chapter 5). From these curves, the apparent Schottky barriers as a function of $V^{1/2}$ can

be obtained (see Figure 6.4 b)) and a zero-voltage SBH of $\phi_{\uparrow} = 0.9(1)\text{eV}$ can be extracted as the intercept at the origin[19]. Therefore, polarization switching induces a change of 1.7 eV in the SBH, which explains the huge change in the conduction level observed by us and various authors upon switching the polarization of a BiFeO₃ crystal[6; 11; 12].

Even though the polarization bound charges at the interface of non-perfect electrodes seem to be the crucial ingredient to explain this change of SBH (and thus conduction through the ferroelectric)[27; 32], it is often reported that oxygen vacancies play an important role in resistive switching. In order to separate the effect of polarization charges from that of charged defects it is useful to turn to the local measurements at DWs, because these are non-polar entities within the ferroelectric. When measuring locally at non-polar 71° DWs, a SBH of $\phi_{DW} = 0.8(2)\text{eV}$ and $\phi_{DW} = 0.5(6)\text{eV}$ have been observed in samples with lower and higher oxygen content, respectively[35; 36], as shown in Figure 6.1. This indicates that the oxygen vacancies in the two samples lower the SBH by $\Delta\phi_V = \phi_o - 0.8\text{ eV} = 0.6\text{ eV}$ and $\Delta\phi_V = \phi_o - 0.5\text{ eV} = 0.9\text{ eV}$, respectively. When comparing the conduction levels for samples with different oxygen contents, we observe that while the current at the DWs increased by a factor of 10 simply by increasing the cooling rate after growth (therefore, increasing the number of vacancies), the current of the domains remained unchanged (See Figure 5.6 in chapter 5). This seems to confirm the model of positively charged oxygen vacancies accumulating around the walls and reducing the SBH with the electrodes[35; 36].

Thus, from the results of Figure 5.6, we can then assume that the oxygen vacancies do not contribute significantly to lowering the SBH in the domains. In the as-grown down domains, the SBH with the top electrode is then modified mainly by the negative polar charges, $\phi_{\downarrow} = \Delta\phi_o + \Delta\phi_P = 1.4\text{eV} + \Delta\phi_P = 2.6\text{eV}$ (measured value) and, thus the effect of polarization bound charges is $\Delta\phi_P = 1.2\text{ eV}$. Upon polarization switching, the SBH will then become $\phi_{\uparrow} = \phi_o - \Delta\phi_P + \Delta\phi_{scr} = 1.4\text{ eV} - 1.2\text{ eV} + \Delta\phi_{scr} = 0.9\text{ eV}$ (measured value), which indicates the presence of a different screening mechanism contributing $\Delta\phi_{scr} = 1.7\text{ eV}$ to the total SBH of the up domains. The high conduction state in the up-polarized domains is stable at room temperature and can be measured for weeks after poling. However, increasing the temperature to (and above) 180°C the up-polarized regions switch back within one hour and the low conduction state is recovered (see Figure 6.5). If the screening adsorbates are removed at high temperatures,

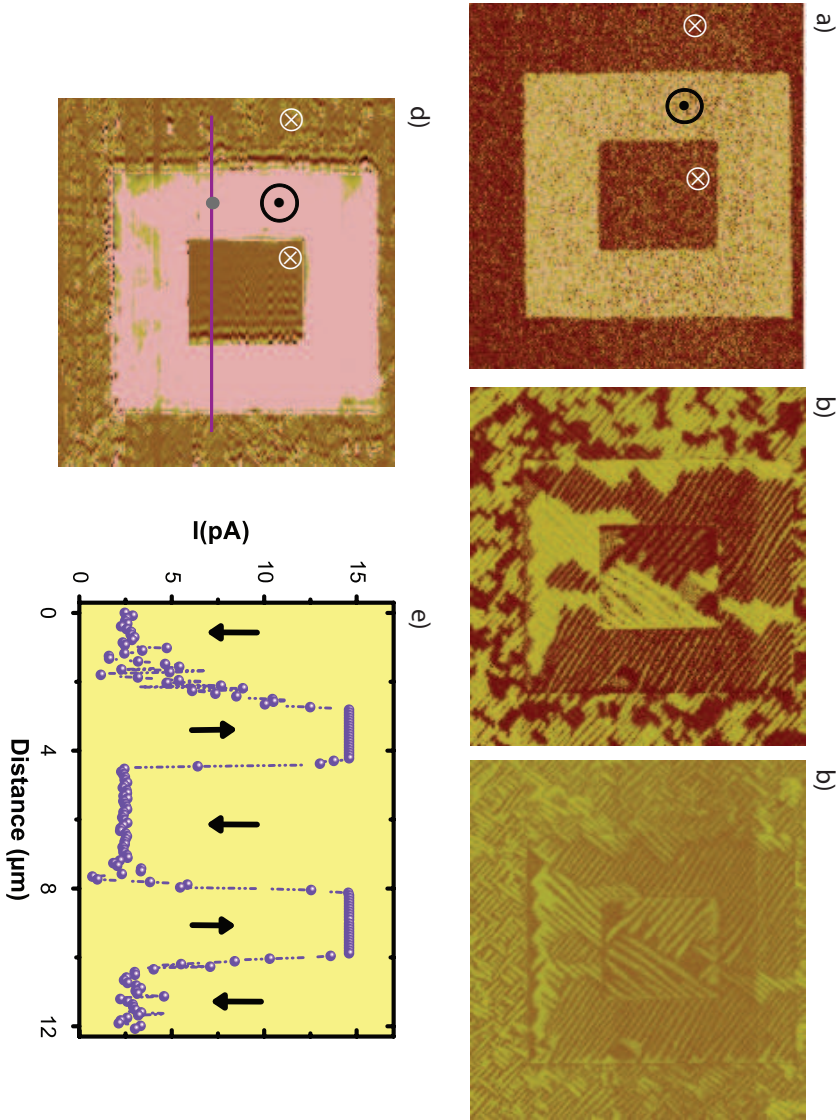


Figure 6.2: (a) Out-of-plane piezo-force microscopy (PFM) phase image showing the as-grown down-polarized state (cross, dark contrast). A square of polarization up (dot, light contrast) has been written. In a second inner square the polarization has been switched back down. (b) In-plane phase and amplitude (c) PFM images. Dot and cross are corresponding the up-polarized areas and down-polarized areas, respectively; (d) conductive-AFM (C-AFM) image of the same area of the film showing enhanced currents at the up-polarized area compared to those in the as-grown state and down-polarized regions. The applied voltage is 2.9 V; All areas are $20\mu\text{m} \times 20\mu\text{m}$ (e) Line scan along the line depicted in (d) across regions with different polarization states, showing the magnitude of the current. The TUNA amplifier is saturated in the up-polarized domains.

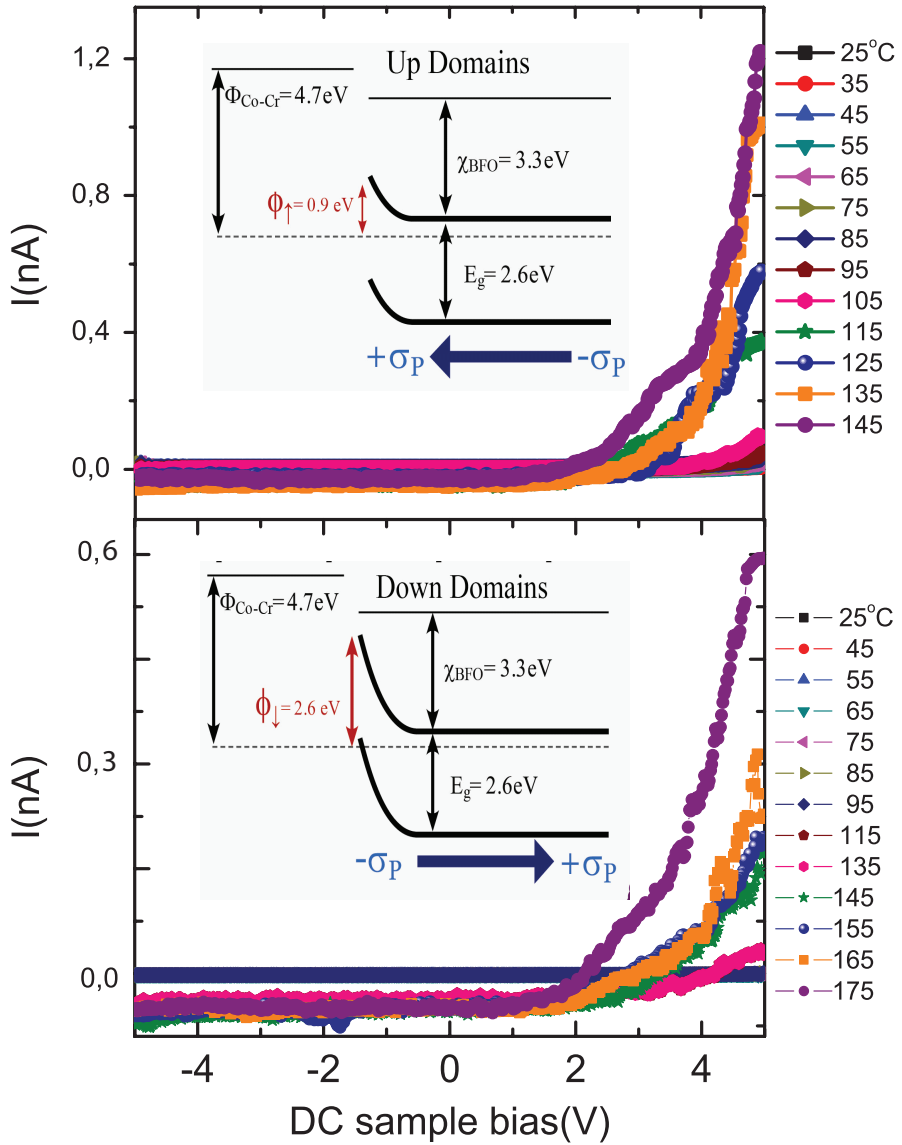


Figure 6.3: I - V curves measured at different temperatures in the up-domains (a) are compared to those previously measured in the down-domains [32] (b). The insets show sketches of the band structure at the interface in both cases.

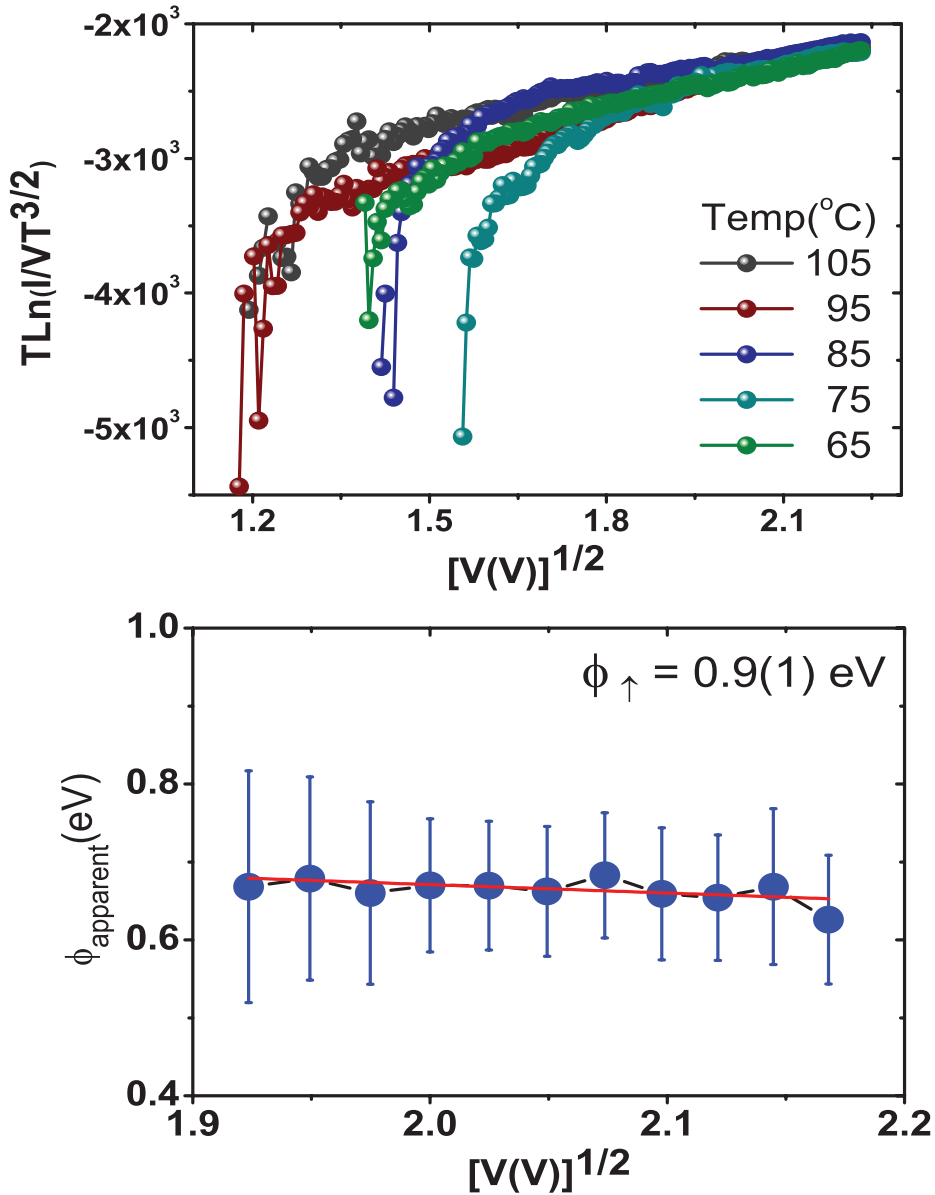


Figure 6.4: The IV curves are plotted such that those data points that fulfill the Simmons-Richardson-Schottky equation show[39] a linear dependence and collapse in a single line. From the slope of the curves a dielectric permittivity of 7.6(3) is obtained (top). Apparent SBH as a function of $V^{1/2}$ (bottom). From its intercept at the origin, a Schottky barrier height of 0.9(1)eV is obtained.

One can expect that diffusion of oxygen vacancies and other charge defects inside ferroelectric is easier in poly-crystalline samples or films showing columnar growth than in fully epitaxial films, therefore, the exact interplay between the polarization and defect charges varies considerably with the sample morphology explaining the different behaviors reported in the literature[6; 15]. Moreover, since this is mainly an interface effect, the type of structural interfaces and twinning is of crucial importance to determine the dominant type of conduction. The films discussed here exhibit only in-plane twinning, that is, the (001) planes of the film are parallel to those of the substrate (see chapter 3)[37], which should be favorable for conduction[19; 37]. It is also worth to mention that the in-plane twinning gives rise to a more clamped structure with larger coercive fields than when the interfaces are buckled by out-of-plane twinning[19; 43]. In fact, we can apply up to 5 V without switching the polarization or inducing domain movement, which allows to increase the current values up to 15 pA at room temperature. Given that the tip diameter, analyzed by Scanning Electron Microscopy, is in between 50nm (new tip) and 100nm (used tip), the observed current densities can be as high as 0.5 A/cm^2 at room temperature.

6.5 Conclusion

In summary, we have measured a 1.7 eV change in the SBH when switching the polarization of a 70 nm thick BiFeO_3 film from (as-grown) down polarized to up polarized. This gives explains the huge changes in resistance for bias voltages applied parallel or antiparallel to the polarization direction, as previously observed. The SBH values measured locally at at up-domains, down-domains and non-polar domain walls allow us to separate the polarization contributions from the screening charge contributions to the SBH. Current densities in the forward direction of 0.5 A/cm^2 are measured. Even larger current values of 5.4 A/cm^2 have been obtained in different BiFeO_3 films[6]. These values rival the dendritic short mechanisms investigated in non-ferroelectric resistive switching[34].

6.6 Experimental

High quality epitaxial BiFeO_3 thin films with thicknesses of 70 nm were grown by pulsed laser deposition on single-terminated (001)-oriented SrTiO_3

substrates covered by a 5nm thick buffer electrode layer of SrRuO₃, as described in chapter 3. After growth, the oxygen pressure in the growth chamber was increased to 100 mbar and the films were cooled down at a rate of 3° C/min.

Atomic force microscopy (AFM), as well as piezo-force microscopy (PFM) and conductive AFM (C-AFM) were carried out using Nanoscope Dimension V microscope from VEECO (now Brucker). For C-AFM measurements a TUNATM amplifier (Veeco/Brucker) was used. The TUNATM module allows three different amplification gains with current sensitivities ranging from 0.5 pA to 24 nA. The tip was grounded and the conductivity was mapped by applying a DC bias to the bottom electrode. Cr/Co-coated n-doped Si AFM tips were used as top electrodes and the SrRuO₃ buffer layer as bottom electrode.

Bibliography

- [1] L. Esaki et al., IBM Tech. Discl. Bull. **13**, 2161 (1971).
- [2] P.W.M. Blom et al., Phys. Rev. Lett. **73**, 2107 (1994).
- [3] J. F. Scott and C. A. Paz de Araujo, Science **246**, 1400 (1989).
- [4] V. Garcia et al., Nature **460**, 81 (2009).
- [5] D.S. Jeong et al., Rep. Prog. Phys. **75**, 076502 (2012).
- [6] A.Q. Jiang et al., Adv. Mat. **23**, 1277 (2011).
- [7] Y. Watanabe, Phys. Rev. B. **59**, 11257 (1999).
- [8] M. Singh et al., J. of Appl.Phys. **91**, 2989 (2002).
- [9] J. Rodriguez Contreras et al., Appl. Phys. Lett. **83**, 4595 (2003).
- [10] C.-H. Yang et al., Nat. Mat. **8**, 485 (2009).
- [11] T. Choi et al., Science **324**, 63 (2009).
- [12] C. Wang et al., App. Phys. Lett **98**, 192901 (2011).
- [13] A.Tsurumaki et al., Adv. Funct. Mater. **22**, 1040 (2012).
- [14] A. Sawa, Mater. Today **11**, 28 (2008).
- [15] X. Chen et al., J. of Alloy and Comp. **529**, 108 (2012); X. Chen et al., Appl. Phys. A **100**, 987 (2010).
- [16] L. Pintillie and M. Alexe, J. Appl. Phy. **98**, 124103 (2005).
- [17] L. Pintillie et al., J. Appl. Phy. **98**, 124104 (2005).

- [18] W. Kanzig, *Phys. Rev.* **98**, 549 (1955).
- [19] L. Pintilie et al., *Appl. Phys. Lett.* **94**, 232902 (2009).
- [20] W. Wu et al., *Phys. Rev. Lett.* **104**, 217601 (2010).
- [21] D. Lee et al., *Phys. Rev. B.* **84**, 125305 (2011).
- [22] H. Kohlstedt et al., *Phys. Rev. B* **72**, 125341 (2005).
- [23] E.Y. Tsymbal et al., *MRS Bulletin*, **37**, 138 (2012).
- [24] M. Bibes et al., *Advances in Physics* **60**, 5 (2012).
- [25] J. Junquera and P. Ghosez, *Nature* **422**, 506, (2003).
- [26] G. Gerra et al., *Phys. Rev. Lett* **98**, 207601 (2007).
- [27] M. Stengel et al., *Phys. Rev. B.* **83**, 235112 (2011); C. Lichtensteiger et al., "In Oxide Ultrathin Films: Science and Technology", Ch. 12, (Eds: G. Pacchioni and S. Valeri), Wiley-VCH (2012).
- [28] L.-W. Chang et al., *Adv. Mater.* **21**, 4911 (2009).
- [29] A.K. Tagantsev and G. Guerra, *J. Appl. Phys.* **100**, 051607 (2006).
- [30] M. Stengel et al., *Nature Mater.* **8**, 392 (2009).
- [31] M.Y. Zhuravlev et al., *Phys. Rev. Lett.* **94**, 246802 (2005); E. Tsymbal and H. Kohlstedt, *Science* **313**, 181 (2006).
- [32] C. Ge et al., *Appl. Phys. Lett.* **99**, 063509 (2011).
- [33] F. Chen and A. Klein, *Phys. Rev. B* **86**, 094105 (2012).
- [34] R. Waser and M. Aono, *Nature Mat.* **6**, 833 (2007).
- [35] S. Farokhipoor, B. Noheda, *Phys. Rev. Lett.* **107**, 127601 (2011).
- [36] S. Farokhipoor, B. Noheda, *J. Appl. Phys.* **112**, 052003 (2012).
- [37] C.J.M. Daumont et al., *Phys. Rev. B* **81**, 144115 (2010).
- [38] S. Hiboux and P. Muralt, *Integrated Ferroelectrics* **36**, 86 (2001).

- [39] S.M. Sze and K.NG. Kwok, "Physics of Semiconductor Devices", Third Edition. Ed. Wiley- Interscience, New Jersey (2007).
- [40] M. Dawber et al., J. of the Eur. Ceramic Soc. **21**, 1633 (2001).
- [41] S.J. Clark and J. Robertson, Appl. Phys. Lett. **90**, 132903 (2007).
- [42] J. G. Simmons, Phys. Rev. Lett. **15**, 967 (1965).
- [43] H. Liu et al., Appl. Phys. Lett. **96**, 012901 (2010).

Summary

This dissertation deals with one of the rare room temperature multiferroics, the well known BiFeO_3 . So-called multiferroic materials display simultaneous magnetic and ferroelectric orders, which is quite uncommon. This rarity, together with the interesting application scope of this group of materials, has caused intense theoretical and experimental research in the last decade. In thin film form, BiFeO_3 allows a great control of the crystallographic (ferroelectric and ferroelastic) domains. Interestingly, the domain walls of BiFeO_3 happen to offer novel functionalities and these (self-assembled) arrays of periodic domains and walls add new possibilities for room temperature applications, such as photovoltaic cells, logic memory devices and circuit designs for nano-scale devices. This thesis mainly focuses on the conduction properties of the domain walls of BiFeO_3 thin films and how and why they differ from those of the domains.

Chapter 1 introduces multiferroic materials, in general, and BiFeO_3 , in particular, as well as some notions on thin film epitaxy and domain formation that are relevant for this thesis. The experimental techniques used have been discussed in Chapter 2. In Chapter 3, BiFeO_3 has been grown in thin films form under epitaxial strain on single-crystal SrTiO_3 substrates with a thin buffer electrode layer of SrRuO_3 . BiFeO_3 under epitaxial strain uses domain formation (presence of regions with different crystal orientations) to better match the crystal structure of the substrate at the local scale. These domains minimize the elastic energy by forming particular patterns or orthogonal domain walls. In this way the low symmetry BiFeO_3 film mimics the four-fold symmetry of the SrTiO_3 substrates. We have observed an unexpected evolution of the lattice parameters with increasing thickness, with an out-of-plane lattice that remains constant up to the larger grown thicknesses (80nm) and the in-plane lattice parameters relaxing and changing quasi-symmetrically. We have been able to explain that observation by the type of domains present and their

relationship with the substrate. First principle calculations as well as a combination of high-resolution x-ray diffraction and piezo-force microscopy (PFM) have been employed to understand the mechanisms underlying domain formation in these films. An important consequence of this work is the realization that the film lattice parameters are not simply dictated by the mismatch between film and substrate, as commonly believed, but also by the domains. Therefore, the lattice parameters of epitaxial BiFeO₃ films on SrTiO₃ with a particular thickness can have different lattice parameters if the films grown with different kinetics.

The formation of different domains dictates the presence of distinct types of domain walls. In BiFeO₃ thin films grown on SrTiO₃ these domain walls are mostly the so-called 71 ° domain walls. That means that the polarization and the unit cell elongation that takes place along the body diagonals of pseudo-rhombohedral BiFeO₃ change by 71 ° across the walls. Nevertheless also some 109 ° domain walls are present in the films. In Chapter 4, the local transport properties inside the domains and at the domain walls have been investigated by means of conducting atomic force microscopy (C-AFM) in combination with PFM. By C-AFM a potential difference is applied between AFM tip and the bottom electrode of the sample (SrRuO₃ in this case) in contact mode and the current is measured.

In Chapter 4, the room temperature conduction at both types of domain walls (71 ° and 109 °) in the as grown state of our BiFeO₃ thin films has been observed for the first time using C-AFM and it turned to be similar in both types of walls and one order of magnitude larger than that of the domains, which are insulating at room temperature. The conduction is rectifying, diode-like, as also reported by other authors. The current density through the domain walls at room temperature can be as high as 0.5A/cm² which is higher than that reported by other types of resistive switching.

In Chapter 5, the possible conduction mechanisms to explain the temperature dependent I-V curves obtained in chapter 4 have been considered for both domains and domain walls. We conclude that both are governed with the same conduction mechanisms, that is: in the low voltage regime ($1V < V < 2.8V$), the conduction band gets populated from defect states close to the bottom of the conduction band. Because of the polarization charges and defect (oxygen vacancies) charges, the current behaves as space charge limited as it is commonly observed in ferroelectrics. However, in the high voltage regime ($3.2V < V < 4.8V$), Schottky emission dominates and

it is the different Schottky barriers with the metal of the tip what gives rise to the two different conduction levels (in the domains and at the domain walls). We postulated that this could be due to the accumulation of oxygen vacancies or charged defects at the walls, driven perhaps by large strain gradients. Charged defects at the interface create potential steps and change the Schottky barrier heights. Indeed, tunability of the current level has been achieved by changing the oxygen content in the sample, confirming our postulate. In addition, the tunability of the current level upon change of top electrodes (different tips with different top electrodes) has been also investigated.

In Chapter 6, the effect of ferroelectric polarization on the conduction level (so-called ferroelectric resistive switching) has been investigated. A huge increase in current is observed when the polarization is switched upwards, in agreement with previous reports. Following a similar approach as in Chapter 5 we find that the same mechanism of Schottky emission is responsible for conduction but that the switching of the polarization upwards reduces the Schottky barrier height by the significant amount of 1.7 eV. By comparing the transport in the up-domains, down-domains and the domain walls, we are able to separate the effect of screening charges from that of polarization charges.

In conclusion, engineered twin domain structures in epitaxial BiFeO_3 on SrTiO_3 substrates dictate distinct types of domain walls (71° and 109°), both of which show conduction levels larger than those previously reported in the literature. We have investigated the conduction mechanisms at both domains and domain walls by temperature-dependent local I-V curves and have shown that the Schottky barrier height at interface with the electrode determines the current level. In addition, we have revealed that oxygen vacancies are responsible for the decreased barrier and enhanced conduction at the walls. Finally, we have investigated the resistive switching in ferroelectric BiFeO_3 thin films, which is of great interest for memory applications.

Samenvatting

Dit proefschrift behandelt BiFeO_3 , een van de weinige multiferroïsche materialen die bij kamertemperatuur actief zijn. Deze zogenaamde multiferroïsche materialen verenigen zowel magnetische als ferroelektrische ordeningen binnen een fasetoestand. Deze bijzondere eigenschap komt niet veel voor en het interessante toepassingsveld van deze materiaalklasse heeft in de laatste tien jaar geleid tot enorme onderzoeksinspanningen op zowel theoretisch als experimenteel vlak. De kristallografische domeinen (ferroelektrische en ferroelastische domeinen) in dunne lagen BiFeO_3 kunnen zeer gemakkelijk worden gemanipuleerd. Een interessante bijkomstigheid is dat de domeinwanden van BiFeO_3 tal van nieuwe functionaliteiten bieden en deze zelf-geassembleerde structuren van periodieke domeinen en domeinwanden bieden nieuwe mogelijkheden voor toepassingen bij kamertemperatuur, zoals fotonische cellen, geheugencellen en circuit toepassingen voor devices op nano-schaal. Dit proefschrift richt zich in het bijzonder op de geleidingseigenschappen van domeinwanden van dunne lagen BiFeO_3 . Hierbij wordt getracht een verklaring te vinden voor de verschillen in geleidingseigenschappen van domeinwanden ten opzichte van de geleiding van de domeinen zelf.

In hoofdstuk 1 maken we kennis met multiferroïsche materialen in algemene zin en met BiFeO_3 in het bijzonder. Verder worden een aantal concepten met betrekking tot epitaxiale groei van dunne lagen en domeinvorming behandeld, die verderop in het proefschrift aan bod komen. De experimentele technieken die in dit onderzoek zijn toegepast, worden in hoofdstuk 2 nader beschouwd. Hoofdstuk 3 beschrijft de depositie en groei van dunne lagen BiFeO_3 onder epitaxiale spanning op een monokristallijn SrTiO_3 substraat dat reeds is voorzien van een dunne SrRuO_3 bufferelektrode laag. In BiFeO_3 onder epitaxiale spanning vindt domeinvorming (gebieden met verschillende kristalorientaties) plaats om de mismatch tussen de lokale schaal in de film aan te passen aan die van het kristal rooster van het sub-

straat. Deze domeinen minimaliseren de elastische energie door speciale patronen te genereren van loodrechte domeinwanden. Op deze manier kan een BiFeO_3 film met lage symmetrie de viertallige symmetrische eigenschappen van het SrTiO_3 substraat nabootsen. We hebben een onverwachte ontwikkeling van de roosterparameters waargenomen naarmate de laagdikte toeneemt, met een rooster loodrecht op het vlak dat niet wezenlijk verandert naarmate de laagdikten toenemen (80 nm), terwijl de roosterparameters in-het-vlak juist relaxeren en quasi symmetrisch veranderen. We zijn in staat om deze observatie te verklaren aan de hand van het soort domeinen dat aanwezig is en hun relatie tot het substraat oppervlak. De mechanismes die ten grondslag liggen aan domeinvorming in deze dunne lagen zijn nader bestudeerd aan de hand van ab initio berekeningen en hoge resolutie Röntgen diffractie in combinatie met piezo-kracht microscopie (PFM). Een belangrijk resultaat van ons onderzoek is het feit dat de roosterparameters van de dunne film niet simpelweg alleen worden bepaald door de roostermispassing van de film ten opzichte van het substraat, zoals eerder vaak werd verondersteld, maar dat ook de domeinen hierin een rol spelen. De roosterparameters van een op SrTiO_3 epitaxiale gegroeide BiFeO_3 laag met een bepaalde filmdikte kan dus wezenlijk verschillende roosterparameters vertonen wanneer de groeikinetiek van de lagen anders is.

De vorming van verschillende domeinen wijst op het bestaan van verschillende typen domeinen. De domeinwanden die voorkomen in BiFeO_3 films die gegroeid zijn op SrTiO_3 substraten, zijn veelal de zogenaamde 71° domeinwanden. In een dergelijke domeinwand verandert de polarisatie (en tevens de trekvervorming van de eenheidscel die plaatsvindt langs de lichaamsdiagonalen van pseudo-rhombohedraal BiFeO_3) 71° wanneer de domeinwand doorkruist wordt. Er zijn echter ook 109° domeinen aanwezig in de films.

In hoofdstuk 4, zijn de lokale transport eigenschappen binnen de domeinen en ter hoogte van de domeinwanden onderzocht met behulp van geleidende atoom kracht microscopie (C-AFM) in combinatie met PFM. In de C-AFM techniek wordt een elektrische potentiaal tot stand gebracht tussen de AFM-naald en de elektrode die reeds is aangebracht aan de onderkant van het substraat (in dit geval SrRuO_3). Vervolgens wordt de stroomsterkte gemeten terwijl het oppervlak in de contact modus wordt afgetast.

In hoofdstuk 4 bestuderen we als eersten de geleiding met behulp van C-AFM bij kamertemperatuur van zowel het 71° domeintype als het 109°

domeintype van onze BiFeO_3 films. De geleiding blijkt vergelijkbaar voor beide typen domeinwanden en een orde van grootte hoger dan die van de domeinen zelf, die bij kamertemperatuur elektrisch isolerend gedrag vertonen. Het geleidingsmechanisme is rectificierend, en heeft veel weg van diode gedrag. Dit is in overeenstemming met de bevindingen van andere auteurs. The stroomdichtheid door de domeinwanden kan bij kamertemperatuur oplopen tot wel $0.5\text{A}/\text{cm}^2$. Deze hoge stroomdichtheid is nog niet eerder vertoond in onderzoek aan andere vergelijkbare typen weerstandsgemoduleerd schakelgedrag.

In hoofdstuk 5 passeren alle mogelijke geleidingsmechanismes de revue om de temperatuurafhankelijke I-V curves die eerder in hoofdstuk 4 zijn besproken, te kunnen verklaren. Zowel het transportgedrag van domeinen als dat van domeinwanden wordt in beschouwing genomen. We komen tot de conclusie dat de transportmechanismen voor domeinen en domeinwanden van vergelijkbare aard zijn: Bij lage spanningen ($1\text{ V} < V < 2.8\text{ V}$), wordt de conductieband bezet door ladingsdragers die afkomstig zijn van defect toestanden. Deze defect toestanden zijn energetisch nabij de bodem van de conductieband gesitueerd. De stroom vertoont ruimtelading begrensd gedrag, dit is in overeenstemming met wat verwacht mag worden voor ferroelektrische materialen. Bij hoge spanningen ($3.2\text{ V} < V < 4.8\text{ V}$), domineert Schottky emissie het transportgedrag echter. De verschillende Schottky barrières ter hoogte van de AFM naald hebben verschillende geleidingsniveaus tot gevolg (binnen de domeinen en ter hoogte van de domeinwanden). We benoemen twee mogelijke verklaringen voor dit gedrag. De eerste mogelijkheid is dat dit wordt veroorzaakt door een opeenhoping van vacante zuurstof posities. De tweede mogelijkheid is dat geladen defecten bij de domeinwanden dit gedrag veroorzaken, wellicht gedreven door grote roosterspanningsgradienten. Geladen grensvlakdefecten genereren discontinue potentiaal stappen en veranderen de hoogte van de Schottky barrière. De stroomsterkte kan inderdaad worden aangepast door de zuurstofhoeveelheid in het monster gericht te varieren, wat onze eerdere aanname bevestigt. Bovendien is onderzocht hoe de stroom kan worden veranderd door een ander type AFM-naald te gebruiken (voorzien van steeds een ander elektrodemateriaal).

In hoofdstuk 6 behandelen we de invloed van ferroelektrische polarisatie op het geleidingsniveau (het zogenaamde ferroelektrische weerstandsgemoduleerd schakelen). Een enorme stroomtoename word waargenomen zodra de polarisatie in opwaartse richting wordt geschakeld, dit effect is

in overeenstemming met eerder vergelijkbaar onderzoek. Analooq aan de benadering die we in hoofdstuk 5 kozen, vinden we wederom een Schottky emissie mechanisme dat verantwoordelijk is voor de geleiding. Echter, zodra de polarisatie opwaarts wordt geschakeld, leidt dit tot een aanzienlijke verlaging van de Schottky barrière met een energie van maar liefst 1.7 eV. Door de transporteigenschappen van de opwaartse domeinen, neerwaartse domeinen en die van de domeinwanden onderling te vergelijken, zijn we in staat om afschermingsladingen te onderscheiden van polarisatie ladingen.

We concluderen dat specifiek ontworpen tweeling domein structuren in epitaxiaal aangebracht BiFeO_3 op SrTiO_3 altijd leiden tot specifieke domein wanden (71° en 109°). Beide domeintypen vertonen betere geleidingseigenschappen dan voorheen gerapporteerd in de literatuur. Aan de hand van de temperatuur afhankelijkheid van lokale IV karakteristieken hebben we de geleidingsmechanismen van zowel domeinen als domeinwanden in kaart gebracht, om vervolgens aan te tonen dat de hoogte van de Schottky barrière op het grensvlak tussen de electrode en de film de stroomsterkte bepaalt. We hebben bovendien het bewijs geleverd dat vacante zuurstof posities verantwoordelijk zijn voor een minder hoge barrière en een diensgevolge hogere geleiding ter hoogte van de domeinwanden. Met het oog op het belang van mogelijke toepassingen in geheugencellen hebben we tot slot het schakelgedrag van ferroelektrisch BiFeO_3 onder de loep genomen.

Acknowledgements

Prof. Beatriz Noheda and Prof. Thomas Palstra, I thank you for giving me the opportunity to be part of your group. Beatriz, it was a truly fabulous experience to work under your supervision while you gave me the freedom of a real researcher. Thank you for the trust. I so much enjoyed the hours that we spent together to understand the physics behind my experiments. Your intelligence always amazed me. Thank you for great inspiration. Special thanks to Lucas and Ian to share their mother's time with me, you patiently came along all the way with me step by step. Thank you for your great patience. Besides all these things, Beatriz, you build a good international perspective for my future by believing in me to give me the opportunity to present our works in more than 30 conferences during my PhD. I would never be able to thank you enough. Thom, first, I want to thank you for acting like a family member when there were some issues with Iranian student residence permits in Netherlands. You gave me and this issue great priorities, regardless of your very busy schedule. I will never forget that. On top of this, it was a luxury to have you in the group meetings. You always asked excellent and motivating questions. Also, many thanks go to Prof. Rob de Groot and Dr. Graeme Blake for their useful inputs during our weekly group meetings. Dr. Tamalika, I want to cordially appreciate all your useful inputs during my PhD. You are a great support. My very special thank goes to Prof. J. Scott who was always willing to help us for improving our manuscripts. I do appreciate that, Sir.

I am very grateful to my reading committee members: Prof, Guus Rijnders, Prof. Gustau Catalan, Prof. Hans Christen. Hans, I want to express special my gratitude to you. The presented thesis enormously improved by your brilliant inputs. You were the first one who wanted to read my dissertation. You were always amazingly kind to spend your break time at MRS, APS, WOE to discuss over my dissertation. You are one of the most important reasons that I am still in science. My very special

thanks go to Gustau, who accurately read my thesis and enlightened me with his smart comments. Moreover, for a person that loves to work on several projects at the same time, like me, having your brilliant ideas was just a miracle. It was/is a great honor to collaborate with you. I am greatly indebted to Alexie Gruverman who spent one week of his valuable time with us in our lab. You were the first one seeing my C-AFM images on domain walls when I was just starting, and I learned a lot from you. You were the one encouraging me to continue on that project, and now it is the main subject of my dissertation. Thank you!

I am greatly pleased to thank all my collaborators and colleagues to whom I have provided with various samples to broaden my horizon in science with several projects that are not included in this thesis: to Prof. Gustau Catalan and Dr. Neus Domingo at CIN2 (Barcelona) for our projects on oxide interfaces and magnetoresistance effect at domain walls, to Prof. Elisabeth Soergel in Bonn for the project on PFM quantitative measurements on BiFeO₃ samples with and without bottom electrode, to Prof. Sara Thompson at university of York for the IR spectroscopy measurements, to Prof. Theo Rasing and Dr. Diana Gheorghe in Radboud university for Second Harmonic Generation measurements, to Prof. Jan Aarts and Dr. Klara Uhlirova for the LEEM measurements, to Dr. Sriram Venkatesan and Alexander Müller from the Ludwig Maximilian University of Munich for TEM studies on both BiFeO₃ and TbMnO₃ samples, to Monika Iwanowska, Dr. Igor Stolitchnov and Prof. Nava Setter at the EPFL (Lausanne) for conduction studies at DWs in BiFeO₃ films on DyScO₃ substrate, to Prof. Dago.de. Leeuw at the Holst Center for their electronic measurements using PbTiO₃, to Dr. César Magen and Dr. Etienne Snoeck at the INA (Zaragoza) for the very impressive TEM studies on TbMnO₃ samples, to Fatwa Abdi and Prof. Bernard Dam in Delf university for measuring photocurrent and to Dr. Christianne Beekman and Prof. Hans Christen at Oak Ridge Nat. Lab. for investigation of conduction properties on morphotropic phase boundaries on BiFeO₃ thin films. I also benefited a lot from a couple of intense discussions with world experts at scientific meeting. Those with Jim Scott, R. Ramesh, Patrycja Paruch and Finlay Morrison have been important for this thesis.

I would like to thank the people I was working with: Jacob, I almost learned everything from you in the physics lab. You could appear in the lab within few minutes whenever I needed you regardless of the time and the day. Your help was not just limited to the lab, even outside the lab

you were a great friend. Speciale dank voor jou! Henk Bruinenberg, thank you very much for being always available for helping a just arrived non-experienced PhD student. Henk Bonder, I appreciate your unconditional support in the lab. Thank you Henriët for arranging all the paper works and being so helpful. Bernard, I would like to endlessly thank you for all the wire-bonding that you have done for me.

Anne, you are one of my best friends. How I can possibly thank you for all our great time together, your endless cares, your emotional and wise supports, and thanks a lot for being my paranymph. Johan, you have always been a great help. You always showed a lot of interest to our long scientific discussions. Also, thank you for accepting to be my pharanymph. Christophe, Ard and Gijsbert, when I came here you were in your last year with all the stress and huge amount of work involved. But, you always had time for me. Thanks for teaching me how to work in the SSME lab. Jos, thank you very much for spending time to program my measurements with Lab-view. Special thanks to my old roomie: Oleksiy and Jeroen and the new ones: Mai and Alex for bearing me. It was a great pleasure to work with all my colleagues from different cultures who make the lab environment nicer with their positive presence: Igor, Syarif, Shiva, Sylvia, Hilde, Kaliani, Laya, Aisha, Alim, Thomas, Arnoud, Anil, Guowei, Naureen, Gaurav, Sander and Saurabh.

Besides, all my colleagues, I sincerely like to express my appreciations to all my Persian friends. Life is much more beautiful and less worrisome with you guys here; Salomeh, Parisa, Mehdi, Mehrnoosh, Fariba, Sara, Amir Hossein, Sahar, Ismail, Ali, Qader, Morteza and Elham. I want also to thank Raziëh, Mehdi and Mahdi for helping me with my computer issues and for my cover design.

Fatemeh, my very first friend whom I titled as honey, though, it took me a while to realize that I really meant it when I said it to you. I simply love to listen to you, to your endless philosophical speech and theories. I love our traveling in a way I miss you whenever I travel alone. Our friendship does mean a lot to me my very special honey. Mehrsima, my sweetheart housemate; I am proud of being friend with you for almost 10 years. How happy I felt from the moment that you decided to come to Groningen and we decided to live together. Everything just happened that naturally and comfortably that it is still too unbelievable, and I am sure it is all because you are great. I will never forget our tea time which can take till morning.

Thank you Leila. You are more than a cousin to me. I think I inherit the studying enthusiasm from you. You were always so generous with me. Thank you my lovely Hamideh for being the best ever sister. You always charge me with your endless source of energy. I cannot live without your daily cares. I am very grateful to my lovely brother, Mohamad. How I can possibly make a decision without talking to you! You are my valuable source of wisdom and kindness. You are the best ever brother. As I can remember, you, guys, have always been so much supportive.

Mom, my education has always been your first priority, you are so serious about it and you sacrificed a lot from your own life for that. But at the same time, it is always fun with you. Dad, you are my priceless source of calmness, strength, trust and power. It is beyond words to thank you, my lovely parents.

*Saeedeh Farokhipoor
Groningen
05.March.2013*

